An investigation into the effect A and B-site doping of precious metal free perovskite oxides on the material structure and the electrocatalytic facilitation of the Oxygen Evolution Reaction (OER) as alkaline electrolyser anodes.

Steve Ward

This thesis is submitted for the degree of
Doctor of Philosophy

School of Engineering

Newcastle University

February 2022

Abstract

Climate change is arguably the single most important issue facing humanity in the modern day. Increasing global temperatures due to the greenhouse effect arising from carbon emissions are predicted to have devasting effects on oceanic seawater levels, disease, and agriculture if current levels of emission are not reduced. In 2020, fossil-fuels (coal, oil, and natural gas) were responsible for around 32 billion tonnes of CO_2 emission worldwide. Therefore, there is a strong push for scientists and engineers to develop sustainable energy alternatives to the current fossil-fuel based systems that are currently in place.

Although there are many fields of interest where sustainable energy processes would be highly initiative, one of the largest uses of fossil fuels is in the production of combustible fuels. It has long been known that hydrogen gas has the highest energy density of any fuel (120 MJ/kg) where the gasoline contains 44 MJ/kg, and when combusted produces water vapour instead of carbon dioxide. Currently, alongside the known dangerous of storing hydrogen gas, the main source of hydrogen currently used for fuels are carbon containing natural gasses such as methane, so this is not a long-term sustainable solution to reducing carbon emissions. However, processes such as electrolysis of water into oxygen and hydrogen gas provide carbon free fuels as well as a safer hydrogen storage method. Specifically, alkaline electrolysers (AE) offer a promise as a sustainable green energy producer due to higher durability, relatively inexpensive electrolytes and electrocatalysts, and lower dissolution of the anodic electrocatalyst into the electrolyte solution.

Alkaline electrolyser systems utilise alkaline electrolyte solutions to increase the facilitation of the oxygen evolution reaction (OER) at the anodic electrocatalyst. The oxygen evolution reaction is the limiting reaction in water splitting due to the sluggish kinetics of the 4-electron catalytic reaction, so increasing the facilitation of this reaction will in turn lead to an increase in the amount of hydrogen fuel generated at the cathode. The current state-of-the-art alkaline electrolyser systems use precious metal oxide catalysts such as IrO2 or PdO2 as anode materials. The selection of these catalysts is considered a limitation due to poor ionic conductivity and economically unfavourable materials used. This produces an opportunity into developing new alternative catalytic materials which have high performance and are economically and environmentally sustainable. This material development is the primary focus of the work contained in this thesis.

Precious metal free, transition metal-based perovskite oxides have been observed to have these desirable qualities when utilised as oxygen evolution reaction electrocatalysts. In this PhD project, various perovskite oxide material series with the formula $ABO_{3-\delta}$, with selected dopants A' and B' were synthesised through wet chemical methods, and the electrocatalytic performance was measured. In particular, the manipulation of the atomic structure of perovskite oxides through various cation doping to alter the levels of electrocatalytic facilitation of the oxygen evolution reaction were explored mainly to control the oxidation state of the transition metals occupying the B lattice site and the oxygen vacancy content (δ). This was then combined with investigations into altered grain morphologies through alternative material synthesis pathways to provide a thorough investigation into the level of electrocatalytic activity of the materials and further optimise from the atomic into grain-size level, with respect to the oxygen evolution reaction in alkaline media.

The initial investigation of the thesis is understanding the effects of increased addition of Sr^{2+} aliovalent dopant ions into the crystal lattice of $Pr_{1-x}Sr_xFeO_{3-\delta}$ (PSFO) perovskites *via* A-site substitution on the OER. The addition of the Sr^{2+} ions was found to drastically improve the OER catalytic activity of the material, as undoped $PrFeO_3$ catalyst was not electrocatalytically active up to 1.70 V_{RHE} in 0.1 M KOH electrolyte, whereas the x = 0.5 material measured a lower onset potential and the highest level of catalytic activity. This improvement in the electrocatalytic performance was associated with the increase in oxygen vacancies in the material due to the change imbalance of the Pr^{3+} and Sr^{2+} ions, which was shown through changed to the iron oxidation state. Building on these findings, Sr^{2+} was replaced with Ba^{2+} inducing an ordered double perovskite structure, and the stoichiometry of the B-site was altered to produce a series of $PrBaCo_{2(1-y)}Fe_{2y}O_6$ (PBCF) double perovskites. From the results of the double perovskite study, the ideal stoichiometric ratio of Co/Fe cations was determined to be y = 0.2. From this point a material using the combined findings was developed with the formula $Pr(BaSr)Co_{2(1-y)}Fe_{2y}O_6$ (PBSCF). This material had similar results to the strontium free double perovskite and was theorised to be limited due to poor phase purity, as phases such as Ruddlesden-Popper ($A_{n+1}B_nO_{3n+1}$), single perovskite (ABO_3), and spinel (AB_2O_4) were discovered alongside the primary double perovskite phase.

All materials in this study were comprehensively characterised through powder X-Ray diffraction (XRD) and refining the resulting powder diffraction patterns using Rietveld method to determine factors such as space group, lattice parameters, lattice volume, and bond lengths. The surface structure was investigated using X-Ray photoelectron spectroscopy (XPS), and the electrocatalytic activity was characterised through techniques such as cyclic voltammetry (CV), electrical impedance spectroscopy (EIS) and Tafel slope analysis.

Acknowledgements

TABLE OF CONTENTS

LIST OF FIGURES

List of Abbreviations

Abbreviation	Definition
3EC	3 Electrode Cell
CA	Citric Acid
CE	Counter Electrode
CV	Cyclic Voltammetry
EEC	Equivalent Electrical Circuit
EIS	Electrochemical Impedance Spectroscopy
HT	Hydrothermal
i	Current Density
OER	Oxygen Evolution Reaction
PBCF	PrBaCoFeO
PBSCF	PrBaSrCoFeO
PSFO	PrSrFeO
REF	Reference Electrode
RHE	Reversible Hydrogen Electrode
SEM	Scanning Electron Microscopy
SG	Sol-Gel
V	Volts
WE	Working Electrode
XPS	X-Ray Photoelectron Spectroscopy
XRD	X-Ray Diffraction

Chapter 1. Introduction

Ceramic mixed ion-electron conductors have received increasing levels of attention in the past few decades for their application in energy storage systems. Determining the most appropriate material to use in specific energy systems is a complex process, as factors such as electrocatalytic activity, electronic conductivity, longevity of materials, operating conditions, environmental and economical sustainability must be considered and analysed.

In this PhD project precious metal free perovskite oxide materials are developed for the electrocatalytic facilitation of the oxygen evolution reaction (OER) at the anode of electrolyser systems. Changes to the catalytic performance are investigated through altering the stoichiometry, atomic make up, and grain morphology of $Pr_{1-z}(Ba_{1-x}Sr_x)_zCo_{2(1-y)}Fe_{2y}O$ transition metal-based perovskite oxides. This chapter provides an overview of the motivation for the study of these materials by discussing the importance of various energy systems that these materials in which these materials are utilised.

1.1 The need for renewable energy

Global energy demand is gargantuan. In 2019 global energy requirement was around 173,340 TWh, and is expected to increase about 5% in the next year.[1] Developing infrastructure which provides low cost, environmentally sustainable energy to meet this demand is one of the greatest, if not the greatest, challenges faced by humanity to date. The increasing effects of climate change provide a serious threat to humanity in all fields of life from rising global temperatures and sea levels, increased risk of disease, and agricultural issues. It is clear that the effects of carbon emissions and the resulting greenhouse effect are felt by human everywhere. Fossil fuels such as coal, oil, and natural gas are not an appropriate fuel source for sustainable development as they are in finite amount and in 2020 were responsible for around 32 billion tonnes of CO_2 emissions worldwide.[2, 3] If fossil fuel systems such as oil, coal, and natural gas are used to satiate global energy demand, then atmospheric CO_2 is estimated to triple which would be environmentally and ecologically devastating.[4] Due to these harmful emissions arising from fossil fuel systems, this provides an opportunity for scientists and engineers to develop technologies to ultimately replace these systems with more environmentally sustainable fuel systems, and away from fossil fuel dependence.[5-9]

Determining the fuel source required to is the clear first step in reducing our dependency on fossil fuel systems, and hydrogen provides an ideal alternate. Despite being the most abundant element in the known universe, has one of the highest relative specific energy constants (120 MJ kg^{-1}) when compared to fuels such as liquefied natural gas (54.4 MJ kg^{-1}), propane (49.6 MJ kg^{-1}), automotive gasoline (46.4 MJ kg^{-1}), and ethanol (29.6 MJ kg^{-1}).[10] This provides a clear pathway that new technologies should ideally be based on hydrogen gas. However, this is not without challenges, as hydrogen gas is an extremely flammable gas, and the dangers of improper storage could be cataclysmic.

1.2 Water Splitting and the Oxygen Evolution Reaction (OER)

There are multiple avenues for producing hydrogen fuel. However, water is one of the most naturally abundant, hydrogen dense, relatively safe environmentally neutral resource on the planet. So, splitting water into hydrogen and oxygen is a logical step for new sustainable technologies. [11]

One of the benefits of water splitting is the production of high purity hydrogen fuel without any CO_2 emissions being generated during the reaction, which sets this technology apart from other hydrogen generation methods such as steam reforming of methane. Obviously, this is assuming that the energy required to drive the electrolyser reaction comes from a sustainable source rather than fossil fuels, but the hydrogen and oxygen generation reactions produce no CO_2. As mentioned above, hydrogen has a very high energy density so is ideal for the transport sector, as the hydrogen and oxygen can be recombined using fuel cells to produce energy which could power a vehicle whilst only producing water as a by-product. However, having access to a reliable source of pure hydrogen gas, stored safely as water, could be massively beneficial to industries outside of transport, as hydrogen is a feedstock to many different chemical processes such as the Haber-Bosch process. The Haber-Bosch process is a particularly good example of how moving towards CO_2 free hydrogen generation could greatly benefit the environment, as ammonia synthesised through the Haber-Bosch process is the most energy intensive commodity chemical in the world, and is responsible for around 1.4% of global carbon dioxide emissions due to the reliance on steam reforming.[12] Moving away from traditional hydrogen production

methods towards water splitting could drastically reduce carbon emissions, and this is why the work on developing these technologies is absolutely crucial.

Although water splitting consists of two half-reactions, the hydrogen evolution reaction (HER) and the oxygen evolution reaction (OER), the reaction is limited by the sluggish kinetics of the oxygen evolution reaction. Therefore, the key to effective and efficient water splitting relies on overcoming the limitations of the 4-electron oxygen evolution reaction. This fundamental concept of overcoming the limitations of OER is the basis for this research, as without a detailed understanding of the catalytic oxygen evolution process, a suitable long term catalyst material for electrochemical generation of hydrogen by water splitting will not be possible.

The key to combatting these kinetic limitations is through selection of electrocatalysts material, as factors that will enhance catalytic activity, such as morphology and atomic changes, can be built into the material. Designing these electrocatalyst materials is the focus upon which this thesis is based. Despite literature regarding the design and performance of oxygen evolution electrocatalyst materials seeing increased interest in the recent decades, the ideal catalyst material with regards to performance and sustainability is yet to be discovered.[13-15] The work in this thesis is therefore to aid in the understanding and knowledge of the scientific community in the study of electrocatalyst materials for the oxygen evolution reaction.

1.3 Solar Cells and Steam Methane Reforming

1.3.1 Solar Cells

When researchers think about water splitting, one of the immediate technologies that comes to mind is electrolysers powered by photovoltaics, or solar cells. Solar cells utilise energy from the sun to instigate the water splitting reaction, whereas technology such as alkaline electrolysers utilise electricity from a direct eternal source. Utilising the power of the sun has obvious advantages, as the sun is the most powerful energy generator in the Sol system. However, solar cells are plagued by inefficiencies relating to weather conditions. Although solar cells can generate power during cloudy and darker days, the efficiency suffers greatly. The performance of solar cells is also heavily influenced by the bandgap of the material utilised as a photovoltaic receptor, meaning that there is an intrinsic limitation of the efficiency of photovoltaic water splitting systems.[16] There is still a lot of ground to cover before large scale implementation of

photovoltaic water splitting systems, and time is a crucial factor in stopping the effects of climate change. For this reason, it is critical that other technologies are investigated alongside photovoltaic methods.

1.3.2 Steam Reforming and the Water-Gas Shift

As briefly mentioned during the Haber-Bosch process discussion, the main technology currently utilised to produce hydrogen is steam reforming of methane.[17, 18] Steam methane reforming (SMR), and specifically when performed in a water-gas shift reactor is a process in which natural gas is heated alongside steam to produce hydrogen and carbon monoxide (equation 1).

$$CH_4 + H_2O \rightarrow CO + 3H_2 \tag{1}$$

The carbon monoxide produced can be further reacted by the water-gas shift reaction (equation 2).

$$CO + H_2O \rightarrow CO_2 + H_2 \tag{2}$$

The overall process is endothermic, and so is performed at high temperatures (over 1000 K) and high pressures (around 15-20 bar) to increase the rate in which product is produced.[19] Which is also assisted by the fact that both reaction 1 and reaction 2 can occur concurrently in the same reaction vessel, which considerably reduces design costs.

As is the case for the oxygen and hydrogen evolution reactions, steam methane reforming is facilitated through a catalytic process. In original publications regarding these reactions in the early 20th century, the catalyst employed was finely divided cobalt or nickel.[20] However, much like other important catalytic reactions, developing an ideal catalyst is a still ongoing long term challenge.[21] The current most employed catalyst for industrial steam reforming is nickel on alumina (Ni/Al_2O_3) due to the affordability and performance.[22, 23] However, these catalysts are limited by severe coking and sintering of nickel atoms due to high temperature conditions, which renders active catalyst sites inactive and causes instrumental down time.[24] This has led to research into more stable, coke resistant catalyst such as those containing noble metals (Ru, Rh, and Pt).[25-27] However, despite promising performance these materials are exceptionally

expensive due to their low abundance, which severely limits the scale up potential of instruments utilising these catalysts.

The steam methane reforming process is obviously highly desirable, as for every mole of methane gas used, 4 moles of hydrogen gas are produced, which is the highest return of any hydrogen producing technology.[28] However, the production of poisonous carbon monoxide and environmentally detrimental carbon dioxide is not ideal. This combined with the reliance on natural gas sources for methane means and high-cost precious metal catalysts that this process cannot remain as the industry leader in option for hydrogen gas production.

1.4 Electrolysers

As mentioned in the solar cell discussion, electrolysers utilise external electrical energy to drive the catalytic degradation of water into oxygen and hydrogen, and most of the research into the electrocatalytic materials in electrolyser systems is focussed on overcoming the sluggish oxygen evolution reaction (OER). There are different types of electrolyser systems which will be discussed in further detail during the literature review chapter of this thesis. However, there are some key differences between the two main electrolyser system candidates, proton exchange membrane (PEM) electrolysers, and alkaline electrolysers (AE).

1.4.1 Proton Exchange Membrane vs Alkaline Electrolysers

Both electrolyser systems utilise the same basic concept of using electrical energy to drive the catalytic splitting of water. The primary difference between the two systems is the electrolyte. PEM electrolysers employ a static solid polymer electrolyte, whereas alkaline electrolysers employ dynamic KOH/NaOH liquid solution. Although both systems utilise half-cell reactions to generate hydrogen and oxygen at the cathode and anode respectively, the half-cell equations are different.

Proton exchange membrane electrolyser:

$$Cathode\text{: } 2H^+ + 2e^- \rightarrow H_2 \tag{3}$$

$$Anode\text{: } H_2O \rightarrow \frac{1}{2}O_2 + 2H^+ + 2e^- \tag{4}$$

Alkaline electrolyser:

$$Cathode: 2H_2O + 2e^- \rightarrow H_2 + 2OH^- \tag{5}$$

$$Anode: 2OH^- \rightarrow \frac{1}{2}O_2 + 2H^+ + 2e^- \tag{6}$$
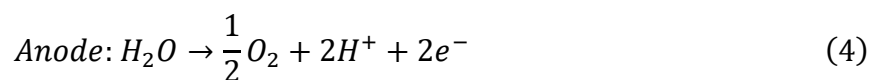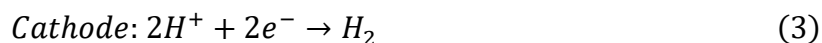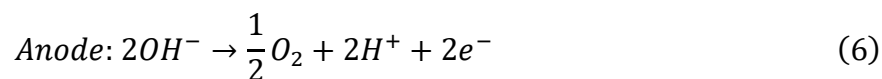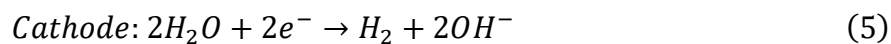
PEM electrolysers have a lower operational temperature than alkaline electrolysers, which allows for a larger operational power window, which is certainly more attractive to industrial systems. However, long term degradation of PEM electrolysers membranes remains a concern which is not shared by alkaline electrolysers due to the simpler set up. [29, 30] These factors considered alongside considerably higher material costs of PEM make alkaline electrolysers somewhat more of an attractive industrial option than when first proposed.

From this brief overview, it seems that the challenges faced by alkaline electrolyser systems are more practical than PEM electrolysers, as if a catalyst material can be designed which provides strong performance at lower operational temperatures (ideally at ambient temperature and pressure), is sustainable and durable, then these AE issues would be solved. It is for this reason that designing an anodic electrocatalyst for alkaline electrolysis is selected as the area of research for this PhD thesis.

1.5 Aims and Objectives

1. Develop a precious metal free oxygen evolution reaction electrocatalyst for alkaline electrolyser anodes, utilising abundant, low-cost metals such as iron

2. Improve the facilitation of the oxygen evolution reaction through material design, investigating the hypothesis that electrocatalytic facilitation can be improved by altering the elemental composition and stoichiometry of materials, whilst maintaining a high phase purity of material in a perovskite oxide configuration.

3. Investigate the effect of different particle morphologies, attained via different synthetic routes, on the catalytic performance and phase purity.

1.6 Chapter Breakdown

This thesis is comprised of 8 main chapters. These chapters contain an introduction to the project, a detailed overview of the literature surrounding the project, an overview of the

methodologies used, a discussion of the results obtained throughout the project, and a comprehensive list of references. A more detailed breakdown of the chapters is as follows:

1. Chapter one contains the introduction to the project. This chapter explains the driving force behind the project, as well as the aims and hypotheses that the project hopes to fulfil.

2. Chapter two contains a detailed literature review for the project. This literature review covers the wide range of electrolyser systems that are available, the multitude of catalyst materials that can be utilised, and the theory behind the oxygen evolution reaction (OER) which is the key reaction that this project aims to solve.

3. Chapter three covers the various analytical and synthetic techniques that were utilised during the project, including the theory behind the operational and data analysis techniques.

4. Chapter four is the first of the results chapters. In this chapter the effect Sr^{2+} doping concentration of $Pr_{1-x}Sr_xFeO_{3-\delta}$ perovskite oxides has on the electrocatalytic facilitation of the OER in alkaline environments. The conclusion of this chapter is that a 50 wt% doping provided the highest level of catalytic activity. This was hypothesised to be caused by the increase in oxygen vacancy (δ) concentration due to the charge imbalance induced by substituting Pr^{3+} with Sr^{2+} cations.

5. Chapter five expands on the ABO_3 nature of chapter four by investigating the performance of varying B site stoichiometries in $AA'B_{2(1-y)}B'_{2y}O_{5+\delta}$ double perovskite oxides. This chapter follows the hypothesis that the filling of the e_g antibonding orbital is directly related to the activity of the OER catalyst. This is achieved by synthesising a catalyst material series with a variety of non-stoichiometric B site ions. Building on from the results of chapter 4, cobalt was introduced into the B site to alter the e_g filling, and barium ions were included in order to obtain the desired double perovskite structure. The double perovskite oxide is also of interest due to the increase electronic conduction, which is highly

advantageous in electrolyser anode materials. The highest performing stoichiometry catalyst was $PrBaCo_{1.6}Fe_{0.4}O_5$ (y = 0.2), which is in line with what has been observed in the literature covering similar materials.

6. Chapter six combines elements from chapters four and five to attempt to develop a catalyst which utilises the benefits of increased oxygen vacancy concentration as displayed in chapter four, and the altered e_g orbital filling of the nonstoichiometric materials discussed in chapter five. This entails the synthesis of $Pr(Ba_{0.5}Sr_{0.5})Co_{2(1-y)}Fe_{2y}O_{5-\delta}$.

7. Chapter seven takes the benefits of the manipulation of the atomic structure and combines this with altering the grain morphology. This was achieved through altering the synthesis route for three perovskite oxides with varied compositions, and the highest performing catalyst material was compared with the results from the previous sol-gel materials of the same stoichiometry. This chapter utilised extensive use of the hydrothermal method which produces easily tuneable and interesting particle morphologies, at the expense of phase purity and production scale up.

8. Chapter eight contains the references for the project.

Chapter 2. Literature Review

In this chapter, a brief overview of the materials which have been used as oxygen evolution electrocatalysts is discussed, and the ABO/AA'BB'O perovskite materials are introduced as the primary focus of this thesis.

The theory of the catalysis of oxygen evolution on an alkaline electrolyser anode surface is briefly discussed in the previous chapter. However, as mentioned, developing a suitable anode is highly dependent on the materials used to facilitate the oxygen evolution reaction (OER). In this section historical catalysts, as well as the theory behind modern-day electrolyser anode materials and the various material classes that have been utilised as OER catalysts is discussed. The various synthesis techniques to synthesised perovskite oxides is also touched upon.

The OER in alkaline media is described in equation 2 in chapter 1.2.4, but for ease of reading it is provided as reference below.

$$4OH^- \rightarrow O_2 + 2H_2O + 4e^-$$
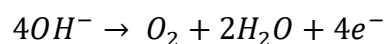
2.1 Precious Metal Oxides

Historically the precious metals Ru and Ir and their corresponding metal oxides have been tested as electrolyser anodes in alkaline electrolyser systems. These anode materials provide some of the most outstanding performance with regards to current response, with reports suggesting that an overpotential of around 470 mV is required to achieve a current response of 10 mA cm^{-2} in 0.1 M KOH electrolyte.[31-35] However, due to the low abundance and high cost of noble metals, these materials are not suitable for long term implementation as electrolyser anode catalysts.[36, 37] For this reason a high performance, economically and environmentally viable material solution is required for large scale implementation of this green energy technology.

2.2 Oxygen Evolution Catalysis and Transition Metal Perovskite Oxides

2.2.1 Activity Descriptors for Oxygen Evolution Reaction in Perovskite Oxides

As previously discussed, a great amount of time and resources have been dedicated to understanding the interaction mechanisms between the oxygen evolution reaction and corresponding catalysts, developing appropriate and dependable activity descriptor of alkaline OER, and ultimately developing a high-performance catalyst.[38] The slow nature of the 4-electron oxidation process per mole of oxygen at the catalyst surface in alkaline electrolyte has been

suggested by Rossmeisl *et al.* to be directly related to the binding strength of oxygen intermediates with the transition metal catalyst surface. More specifically, catalysts that form strong bonds with oxygen are limited by HOO-M formation, whereas catalysts which form weak bonds with oxygen are limited the O-M formation, where M indicates an active catalyst surface site.[39] However, based on a culmination of systematic research into OER activity descriptors, alongside molecular orbital principles, it is reasoned that the occupancy of the e_g antibonding orbital acts as a dependable material descriptor for perovskite oxides.[40] The Shao-Horn group demonstrated this using molecular orbital principles to show a volcano relationship between the e_g orbital filling and the oxygen evolution activity, and found that the ideal e_g electron filling to be approximately 1.2, as shown in Figure 1.[41]
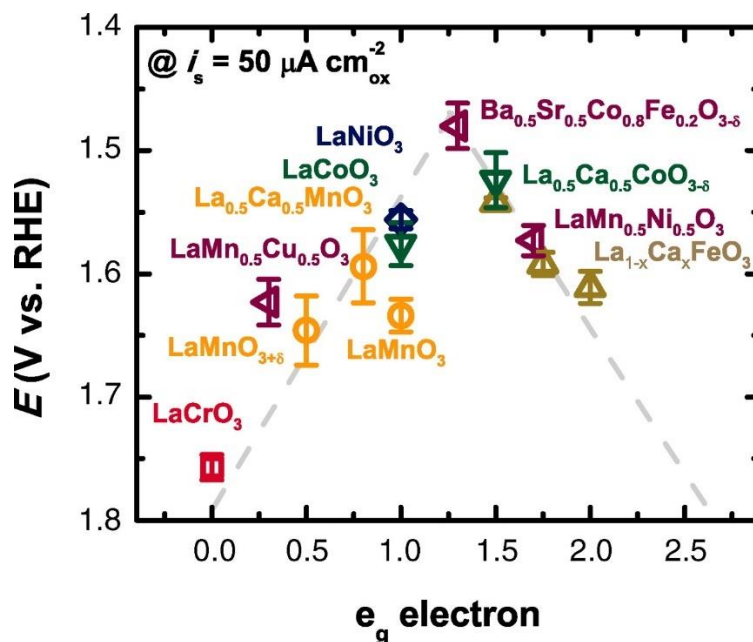
Figure 1 – Relationship between e_g antibonding orbital filling and oxygen evolution activity, showing an ideal filling of approximately 1.2 electrons as shown by the Shao-Horn group.[41]

The activity descriptor of specifically the e_g antibonding orbital is an important distinction from previously proposed electron based activity descriptors such as Bockris and Otagawa (1984), who determined the OER activity descriptor to be based on the filling of the bulk *d* orbital (both the π-bonding t_{2g} and the σ-bonding e_g orbitals).[42] The activity descriptor proposed by Shao-Horn is a logical expansion of that of Bockris and Otagawa, as the antibonding e_g orbital has a more significant overlap with the *2p* orbital of the incoming oxygen species which promotes electron transfer between the catalyst surface and the adsorbed oxygen intermediates.[41] However, due to

the complex nature of the 4-electron catalytic oxygen evolution reaction it is highly unlikely that a single activity descriptor will be suitable for all classes of materials. Shao-Horn accounts for this in separate study, in which the relationship between the OER catalytic activity and stability is described by an activity descriptor of the positioning of the oxygen band centre relative to the Fermi level of the surface of catalyst material atoms.[43] The Fermi level (E_f) of a solid state material such as a perovskite oxide catalyst is generally defined as the amount of thermodynamic work required at 0 K to add one electron to a solid state body, irrespective of the work required to remove any electron from the body first. Or in more practical terms, it is the highest molecular orbital level in which an electron could occupy at 0 K. Clearly, from this definition the Fermi level is temperature dependent which can complicate conceptualising an activity descriptor based around it, although electrolyser systems are temperature limited in their operation, so activity descriptors based the Fermi level are still a valid theory to follow. Specifically, the activity descriptor described by the Shao-Horn group as the relationship between the distance the oxygen p-band centre and the Fermi level, with the highest activity being when the band centre and the Fermi level were close.[43] However, this activity descriptor is limited by being most appropriate at pH 7. Electrolysis of water is considerably more challenging in neutral pH electrolyte media, as the reaction was hampered by B-site ion leaching when O p-band was a far distance from the Fermi level, and A-site leaching and enhanced metamictisation of the catalyst surface when the O p-band was close to the Fermi level. However, as this activity descriptor was also present to some degree at pH levels of 13, it is still appropriate to apply this theory to materials where the e_g orbital filling is difficult to determine, such as in double perovskite oxide structures.[43]

2.2.2 Single Perovskite Oxides (ABO$_3$)

The general formula for simple perovskite oxides is ABO_3, where A-sites are occupied by rare or alkaline earth metal cations, B-sites are occupied by transition metal cations, and the O site is occupied with oxygen anions. The structure of the single perovskite oxide can be visualised as a B-site transition metal ion surrounded by an octahedra of oxygen anions, housed in a cubic arrangement of A-site ions. A visualisation of an ABO_3 single perovskite oxide is displayed in Figure 2.
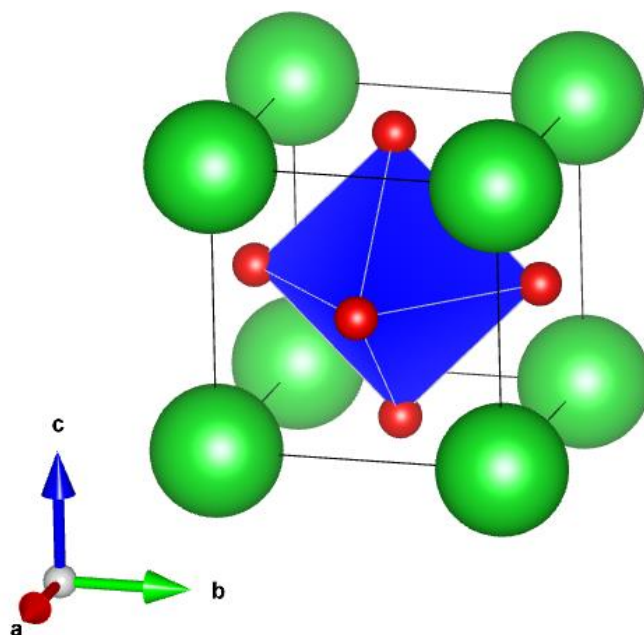
Figure 2 – Simulation of a single unit cell of cubic ABO$_3$ single perovskite oxide. Green spheres represent A-site rare/alkaline earth metal cations, blue represents B-site transition metal ion in octahedral configuration with red oxygen anions. Black lines are for visualisation of unit cell and are purely used as a visual aid.

However, although a simple stoichiometric ABO$_3$ perovskite oxide such as that shown in Figure 2 are relatively simple to synthesise and can be synthesised from a plethora of various atoms, the stoichiometric nature of the pristine perovskites does not lend itself to high performance OER electrocatalysts.

High surface area, doped perovskites with the formula $A_{1-x}A'_xBO_{3-\delta}$ (A = rare earth metal, A' = alkali earth metal, and B = transition metal) have been well researched as potential effective electrocatalysts for the oxygen evolution reaction (OER) at electrolyser anodes. This is due to their relatively low cost (Table 1), high mixed ion electron conductivity, flexibility in physical-chemical and catalytic properties[41], range of synthesis options.[44-52] As discussed, first row transition metal based perovskites have been demonstrated to have high activity for facilitating the oxygen evolution reaction due to the fulfilment of an activity design principle of a near unit occupancy of the d shell σ* antibonding orbital of the B site ion, and overlap with the 2p π bonding orbital of the oxygen species.[41, 53] This has led to the development of perovskite oxides such as La$_x$(Ba$_{0.5}$Sr$_{0.5}$)$_{1-x}$Co$_{0.8}$Fe$_{0.2}$O$_{3-\delta}$ (BSCF)[54-56], LaNiO$_{3-\delta}$ [57-59], and LaFeO$_{3-\delta}$[60] for use as oxygen electrodes.

Table 1 – Average price of common perovskite oxides used in OER electrocatalysts (Source: Sigma Aldrich)

Element	Average price of oxide (>99% purity) (g^{-1})
Precious Metals	
Iridium (Ir)	£155.00
Ruthenium (Ru)	£53.10
Transition Metals	
Cobalt (Co)	£29.60
Iron (Fe)	£5.02
Manganese (Mn)	£0.38
Nickel (Ni)	£4.12
Alkali Earth Metals	
Barium (Ba)	£5.65
Strontium (Sr)	£4.84
Rare Earth Metals	
Lanthanum (La)	£2.26
Praseodymium (Pr)	£17.60

Historically lanthanum has been the A site metal cation of choice for perovskite oxide oxygen electrocatalysts. However, more recently studies have been done by changing the A site cation to another lanthanide metal cation, especially the 'elemental neighbour' of lanthanum, praseodymium. Studies have shown that for oxygen electrocatalyst materials, praseodymium based materials have a considerably higher ionic conductivity than lanthanum based materials, with some studies showing this improvement to be an order of magnitude higher than lanthanum counterparts.[61]

The innate ability of perovskite oxides in facilitating the electrochemical catalysis of the OER can be improved upon further through relatively minor changes to the material. The substitution of metal cations into the perovskite oxide lattice can drastically improve the material's ability to facilitate electrochemical reactions. The exact science behind how tuning the crystal structure of a perovskite to orchestrate higher catalytic activity is often looked over in literature. However, a full understanding of how tuning simple perovskite oxides is critical in the design of more complex catalytic systems and could hold the key to unlocking feasible noble metal free OER catalysts. One such structural tuning is the introduction of oxygen vacancies within the lattice, thought to increase the OER catalytic activity.[62-69] The fundamental science behind this

effect has been investigated in this thesis by substituting Pr^{3+} cations with Sr^{2+} in $PrFeO_{3-\delta}$ perovskite oxides, giving $Pr_{-1x}Sr_xFeO_{3-\delta}$ (x = 0, 0.1, 0.2, 0.3, 0.4, and 0.5), which is discussed at length in chapter 4. The substitution of a trivalent ion for a divalent ion induces a charge imbalance within the material. This induces the formation of an oxygen anion vacancy (denoted by an increased value of δ), which the presence of which is thought to increase the availability of the transition metal catalyst sites to the triple phase boundary, thus increasing the rate of the OER.[70, 71] The mechanism of formation of this vacancy (V) is denoted in Kröger-Vink notation in equation 7, where the trivalent rare earth praseodymium ion (RE^{3+}), is substituted with the divalent alkaline earth strontium ion (AE^{2+}).
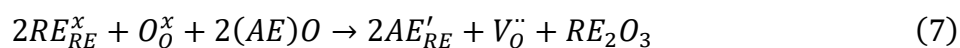
$$2RE_{RE}^x + O_O^x + 2(AE)O \rightarrow 2AE_{RE}' + V_O^{\cdot\cdot} + RE_2O_3 \qquad (7)$$

Where x, ' and • represents neutral, single negative and single positive charge, respectively. This increase in oxygen vacancy concentration is also an increase in the number of electron holes in the crystal lattice. This means the intrinsic semiconductor samples are *p* type semiconductors. Aside from the increase of available catalyst sites created by the holes/vacancies, the increased concentration of electron holes will also increase the electrical conductivity due to an expanded valence band, shortening the distance between the valence band and the fermi level, as discussed in chapter 2.2.1.

2.2.3 Double Perovskite Oxides (AA'BB'O$_6$)

As discussed in the above section $ABO_{3-\delta}$ (A = rare/alkaline earth, and B = 3d transition metal) perovskite oxides are a well-studied class of materials with promise to be substitute catalysts for alkaline OER as they utilize relatively low cost and high abundance materials, and the tuneable catalytic activity through structural manipulation. Similarly, double perovskite oxides with the structure $AA'BB'O_{6-\delta}$ are an attractive class of materials for alkaline water electrolysis anodes. Double perovskites are similar in structure to $ABO_{3-\delta}$ perovskites in that they are both made up of 12 coordinated A site and 6 coordinated B site (when δ = 0) cations. However, in double perovskite oxides the unit cell is doubled along a certain crystallographic axis which has ordered alternating cations. A depiction of a unit cell of a double perovskite with the formula $AA'B_2O_{6-\delta}$ configured in a tetragonal space group with doubling along the *c* crystallographic axis can be found in Figure 3. Double perovskite oxides have shown to have advantageous properties

for electrocatalysis of the OER such as easier diffusivity of oxygen ions, faster surface oxygen exchange, and increased electrical conductivity compared to their $ABO_{3-\delta}$ counterparts.[72]
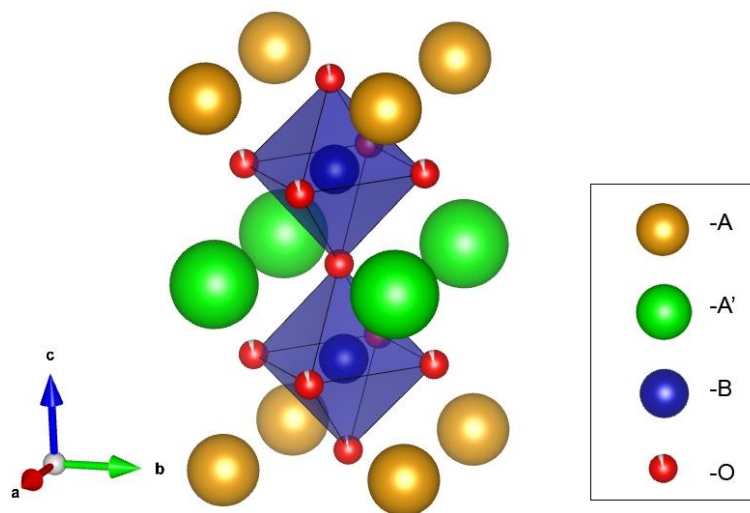
Figure 3 – Unit Cell of an $AA'B_2O_{6-\delta}$ Double Perovskite in Tetragonal Configuration with doubling along the c crystallographic lattice.

Barium is a commonly used alkali earth metal in double perovskites due to its large ionic radius, abundance, and relatively low cost (Table 1). However, it is also of note that the electrocatalytic performance enhancement by tuning the level of transition metal B-site doping, due to the fulfilment of an activity descriptor as outlined by Shao-Horn's group[41], must be taken into account in order to obtain the best performance from the material. Shao-Horn's study found a volcano relationship between the e_g orbital filling of the *B* site transition metal and the performance of the OER. As previously discussed, the filling of the e_g antibonding states of surface transition metal catalysts, rather than the overall number of 3d electrons (with both e_g and t_{2g} electrons) as proposed by Bockris and Otagawa[42], is a more appropriate activity descriptor for the OER. This is due to the σ bonding e_g electron has a much stronger overlap with the oxygen species than the π bonding t_{2g} electron. This stronger overlap leads to a more direct electron transfer between the catalyst surface and the oxygen intermediates. The ideal cobalt to iron doping ratio was determined by the synthesis of a $PrBaCo_{2-y}Fe_yO_{6-\delta}$ (PBCF) double perovskite series.

2.3 Electrolyser Systems

Water is one of the most naturally abundant, hydrogen dense, relatively safe environmentally neutral resource on the planet. The use of electrolyser/fuel cell set ups using

15

water as an energy storage vector has sparked interest in the research community is recent years.[11] One of the biggest challenges faced with development of these systems is the kinetic limitations faced in electrolyser systems, where water is electrochemically separated into hydrogen and oxygen gas. There are many types of electrolyser system setups that can be used to facilitate the water splitting reaction, some of which are discussed below.

2.3.1 Polymer Electrolyte Membrane (PEM) Electrolysers

Polymer electrolyte membrane, or PEM, electrolysers were developed in the 1960s by W.T. Grubb and General Electric. The fundamental concept behind the PEM electrolyser was the use of a solid polymer electrolyte rather than more traditional liquid electrolytes.[73] The use of a solid electrolyte allows for a reduction is gas crossover, keeps the system compressed under high pressure operations, and facilitates the transport of protons through the membrane towards to cathode.[74] During operation of a PEM electrolyser cell, liquid water is fed to the anode where it is oxidised to oxygen gas and protons. The oxygen gas is collected, and the protons diffuse through the solid polymer electrolyte towards to cathode where they are reduced into hydrogen gas. A diagram showing the fundamental reactions and components of a PEM electrolyser by Conte *et al.*, is shown in Figure 4.[75]

PEM - Electrolysis
20°C – 100°C

$$H_2O \rightarrow 2H^+ + \tfrac{1}{2}O_2 + 2e^- \qquad \text{Anode}$$
$$2H^+ + 2e^- \rightarrow H_2 \qquad \text{Cathode}$$

$$H_2O \rightarrow H_2 + \tfrac{1}{2}O_2 \qquad \text{Total reaction}$$
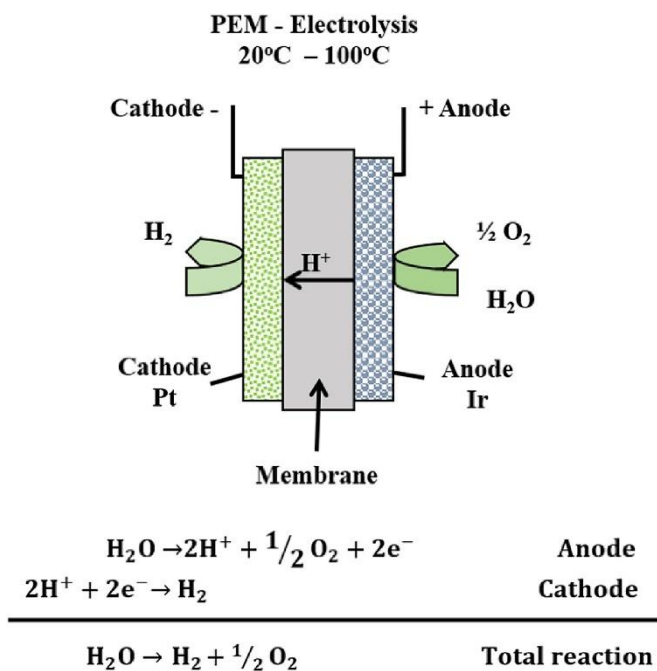
Figure 4 – Diagram showing the components and reaction of a PEM Electrolyser.[75]

PEM electrolysers generally operate with high current densities, and a major factor in this is the opportunity to reduce the thickness of the polymer electrode which leads to a reduction in the ohmic losses and increase in proton conductivity, as well as reduced device and operation costs.[76]

Polymer electrolyte membrane electrolysers are a promising method of hydrogen generation, but they are not without drawbacks. The primary issue of PEM electrolysers is also their greatest strength, being the use of the solid polymer electrode. Although thinning the polymer can lead to high performance with respects to current density, this can also cause structural issues as the electrode is weakened. If the electrode dries out during operation, then the conductivity of the material will sharply reduce which will considerably reduce the efficiency of the instrument. However, this is not the main cause of concern as if the electrode is too dry (or to be too thin) then it is highly likely that a crack will occur due to the high-pressure operating conditions. Any cracking in the electrode runs the risk of short-circuiting the device, meaning it would have to be shut down and the (expensive) electrolyte must be replaced, which at industrial scale could prove economically disastrous.[77]

2.3.2 Solid Oxide Electrolyser Cells (SOEC)

Solid oxide electrolyser cells (SOEC) can be thought of as the reverse operation of the more widely known solid oxide fuel cell (SOFC). Whereas an SOFC system converts chemical energy (for example hydrogen) to electrical energy with high efficiency, an SOEC system converts electrical energy to chemical energy.[78] Just like their fuel cell counterparts, SOEC operate at high temperature. This allows for systems where SOFC/SOEC coupling, which gives a high space efficiency as it allows the production of electrical energy straight from the chemical source.

In a solid oxide electrolyser cell, steam is fed through a solid porous cathode as a voltage is applied, which reduces the steam into hydrogen gas and oxygen ions at the cathode-electrolyte interface. The hydrogen gas diffuses back through the porous cathode to be collected at the surface. The oxygen ions then diffuse through the solid electrolyte towards the anode where they are oxidised into oxygen gas, which diffuses through the porous anode to be collected at the surface. A diagram showing the fundamental reactions and components by Ni *et al.,* is shown in Figure 5.[79]
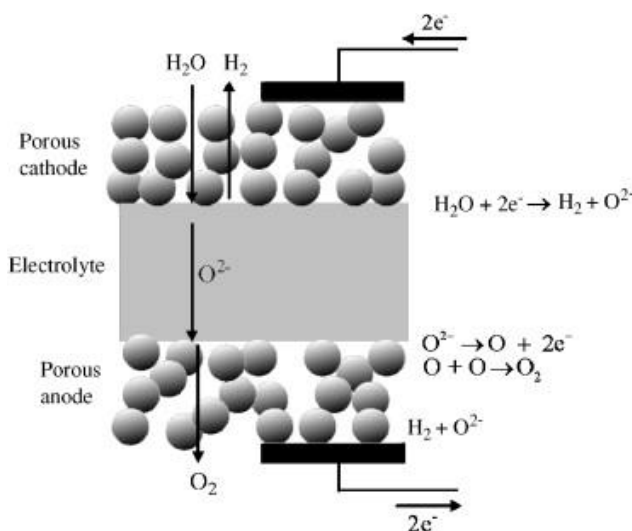
Figure 5 – Diagram showing the components and reactions of a solid oxide electrolyser cell.[79]

As the electrolysis of water is an endothermic process, solid oxide electrolysers must operate at a high temperature to be efficient producers of hydrogen/oxygen gas. This leads to high thermal demand for SOEC operation which can incur massive operational costs, although in combination with the thermal energy produced from SOFC there is the opportunity to recycle the heat back to the electrolyser which can reduce this operational cost.

As well as the operational costs associated with high temperature operation of electrolyser systems, there are other disadvantages that are associated with this. For example, the use of a high temperature environment means that certain material specifications need to be considered which may not be as critical in another electrolyser system, such as ensuring the thermal expansion parameter of the anode, cathode, and electrolyte are all within a similar range to avoid mechanical stress and breakages in the system. The materials used for the electrodes and electrolytes must be chemically inert from one another as the high temperature environment may cause electrode-electrolyte reactions which can significantly dampen the performance of the SOEC.[80]

Overall, SOEC/SOFC systems provide an interesting route for clean energy production but are limited by high temperature environments causing long start up times, electrode-electrolyte reactions, and mechanical stress. This leads to issues with the scale up of these systems in the future, and geographical limitations due to temperature considerations.

2.3.3 Alkaline Electrolysers (AE)

Alkaline electrolyser systems are one of the more mature electrolysis systems, but recently have been revisited as potential water splitting systems. The fundamental principle of alkaline electrolysis is, on the surface, simpler than PEM or SOEC electrolyser systems. As the name suggests, alkaline electrolysers consist of an anode and a cathode submerged in an alkaline electrolyte solution. Generally a solution of potassium hydroxide (KOH) or sodium hydroxide (NaOH) in water is used as it is economically viable due to abundance, avoids dissolution of the catalyst (as has been seen in acidic media), and has a high ionic conductivity.[81] As a side note, it is noted that there are there are safety concerns working with corrosive electrolytes, but with proper risk management and enforcement the risk should be mitigated. During operation, the electrolyte solution is fed into the vessel and a potential is applied which causes water to be broken down into hydrogen gas and hydroxide ions ($OH^-_{(aq)}$). The hydroxide ions then flow through the electrolyte towards the anode, where they are catalytically converted into oxygen gas.[82] An overview of the components of an alkaline electrolyser is shown in Figure 6 by Bodner *et al.*[83]
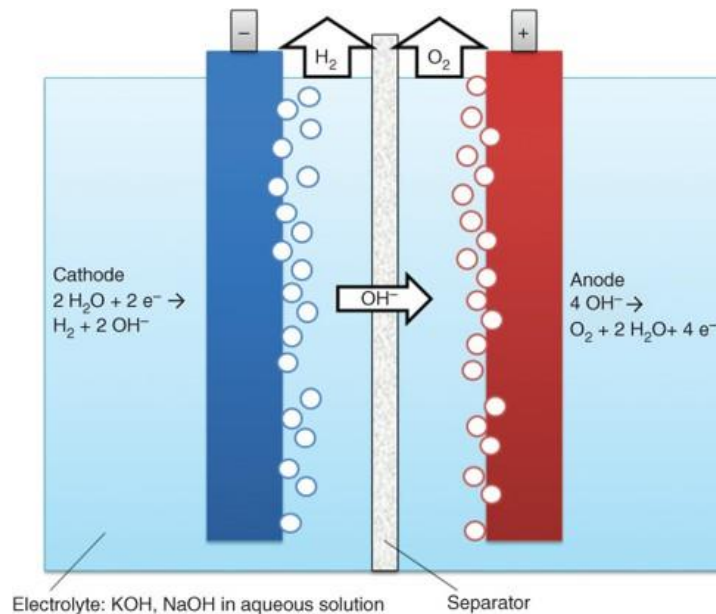
Figure 6 – Diagram showing the components and reactions of an alkaline electrolyser.[83]

The initial difference observed when comparing Alkaline Electrolyser (AE) cells with the two other methods mentioned in this thesis, the Solid Oxide Electrolyser Cell (SOEC) and the

Polymer Exchange Membrane (PEM) cell, is that AE cells consist of a relatively simple set up. This is an attractive characteristic for industries looking at long term scale up as the fewer parts required, the less variables there are to consider during operational planning.

The advantage of AE cells compared with SOEC configurations is the safety and economic gains from operating at a considerably lower temperature with AE cells. However, the distinctions between AE and PEM cells are not as apparent. For instance, PEM cells are generally operated at lower temperatures (50 – 80 °C) than AE cells (80 – 90 °C), albeit at a higher working pressure (≤ 5 MPa and ≤ 3.2 MPa for PEM and AE cells respectively). The main advantage that AE cells have over PEM cells are a considerably longer operation life (10 years in comparison to 3-4 years for PEM cells), and a lower manufacturing cost.[84] This is not insignificant as for long-term scale up processes, capital investment into infrastructure will be of utmost concern to governments and companies looking to implement this technology.

The low operational and manufacturing cost, combined with safety aspects from low temperature operation make alkaline electrolyser cells a highly attractive technology for renewable hydrogen generation from water, and is a clear reasoning behind their current use as electrolysis industry standard. [85]

However, alkaline electrolyser systems are still plagued with the issue that is present in all electrolysis systems, that being that the materials used for the anode and cathode are still reliant on high cost, low ionic conductivity, low abundance precious metal catalysts. In order to increase the viability of electrolyser systems as fossil fuel replacements, new high-performance materials catalysts with high ionic conductivity, low cost, and high abundance need to be developed as alternatives. Due to the nature of the hydrogen and oxygen evolution reactions, the largest advances in the overall electrolyser performance can be made at the anode, where the oxygen evolution reaction occurs.

2.3.4 The Oxygen Evolution Reaction (OER)

As previously mentioned, the oxygen evolution reaction at the anode of electrolyser systems provides the greatest opportunity for improving the performance of the entire electrolyser system. The primary reason behind this is that the oxygen evolution reaction is hindered by slow kinetics of the 4-electron catalytic reaction. Some efficiencies have been

reportedly as low as 53%.[33, 86-88] Due to this, electrolysers often run at potentials of around 1.80-2.00 V, which is considerably higher than the 1.23 V theoretical minimum for water splitting.[89]

As shown in the schematic diagrams of the alkaline electrolyser above (Figure 6), the overall reaction for the electrochemical splitting of water to produce 1 mole of oxygen gas is shown in equation 8.

$$2H_2O \rightarrow 2H_2 + O_2 \tag{8}$$

However, the half-cell equations of reaction 8 in alkaline media provide a description of the electrocatalytic redox reactions that occur at the electrodes of the alkaline electrolysis cell, where the overall anodic oxygen evolution reaction (OER) is described by equation 9.[90]

$$4OH^- \rightarrow O_2 + 2H_2O + 4e^- \tag{9}$$

However, in order to design a catalyst material for the electrocatalytic facilitation of the oxygen evolution reaction in alkaline media (equation 2), a more in depth understanding of the reaction pathway must be investigated. The widely accepted reaction pathway at the catalytic surface for alkaline OER is shown in equations 10-13, where M denotes the catalyst surface.[91]

$$M + OH^- \rightarrow MOH + e^- \tag{10}$$

$$MOH + OH^- \rightarrow MO + H_2O + e^- \tag{11}$$

$$MO + 2OH^- \rightarrow MOO^- + H_2O + e^- \tag{12}$$

$$MOO^- \rightarrow M + O_2 + e^- \tag{13}$$
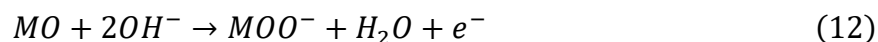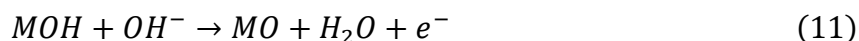
Each stage of the oxygen evolution reaction pathway (equations 10-13) has their own independent activation energies and stabilities, and therefore can all act as a rate determining step to the overall reaction. However, the properties of these catalytic surface reactions are dependent on the reaction conditions and the material used as an electrocatalyst.[92, 93] Calculating which reaction is the rate limiting reaction is a considerably challenging task which requires the use of computational quantum mechanical methods such as density functional theory calculations. Whilst the results reported in this PhD project are based upon complex, peer-reviewed calculations, it is useful to have a basic understanding of the challenges faced by computational scientists.

A conventional method of predicting minimum overpotentials for the reactions is based around the Gibbs free reaction energy. The difference in the chemisorption energy of 2 sequential steps is equivalent to the change in the Gibbs free energy (ΔG) of the 2 reactions at a specific energy. Assuming that the overall change in Gibbs free energy is exergonic, where ΔG is negative, the minimum electrode overpotential can be predicted.[94] However, the limitations of this conventional method is that it can be oversimplistic as it utilises Gibbs free energies at 0 overpotential (η), which is obviously not the case during the real life conditions of the OER in an alkaline electrolyser, so it can be prone to error.[95] Although this is far beyond the scope of this PhD project, it is useful in showing the challenges behind the design of OER electrocatalyst materials.

This activity descriptor is also dependent on the class and atomic make-up of the material used as an electrocatalyst, which is part of the reason that the activity descriptors based on the catalytic pathway are often combined with the interaction between specific material classes such as transition metal perovskite oxides and an oxidised species..

Chapter 3. Experimental and Characterisation Techniques

There are many techniques that can be utilised in the synthesis and characterisation of perovskite oxide materials. These techniques can tell us about the crystal structure of the material, including phase quantification, crystal structure, surface morphology, oxygen concentration, electrocatalytic ability, and surface electronic structure and density to name a few. The techniques used for analysing OER performance of perovskite oxides can be classified as either structural or electrochemical analysis.

Structural analysis is the primary focus of this work as this offers and understanding of the mechanisms behind any change in the electrocatalyical activity or the material. Non-destructive structural techniques utilised in this work are powder X-ray Diffraction (XRD) and X-ray Photoelectron Spectroscopy (XPS) for investigating the structure and composition of the material, and destructive wet chemistry techniques such as Iodometric Titration

The structural characterisation techniques are limited to *ex situ* situations, where the analysis conditions are not necessarily the same as conditions required for operation of a full electrolyser system. This method of analysis brings with it an assumption that the material properties stay consistent between testing and operating conditions. However, this can lead to experimental errors and inaccuracies in the data. In an ideal situation, characterisation testing should be utilised using the exact conditions used during the operation of the system, or *in operando*. As this is not practical for many operations, where possible materials are analysed *in situ*. This is where the conditions are made as close to operational conditions as possible.

Electrochemical characterisation involves *in situ* techniques that are used to determine the electrocatalytic behaviour of the catalyst material. These primarily consist of Electrochemical Impedance Spectroscopy (EIS) to measure the material's electrical impedance, Cyclic Voltammetry (CV) to observe the level of electrochemical reaction occurring over a range of voltages as well as information regarding rate limiting reactions, and Chronoamperometry (Chrono) where the catalyst stability at a specific potential is measured over time.

This chapter details the instruments and techniques used in the investigation of perovskite oxide oxygen evolution catalysts, including the synthesis of samples and the subsequent analysis. The wet chemical methods used for the synthesis of bulk perovskite oxides are outlined first. This

is followed by two sections outlining the *ex-situ* X-ray techniques and the techniques used to analyse the data. The final section details the *in situ* electrochemical techniques used to observe the electrocatalytic behaviour of the catalyst materials.

3.1 Synthesis Techniques

The synthetic pathway and conditions used during the production of the catalyst will play a large role in material factors such as phase purity, grain size, surface area, and particle morphology, as well as production factors such as synthesis cost, complexity, and saleability. Determining an ideal synthesis route is a case of weighing up the positives and limitations of the method to produce a high-performance material with large scale-up potential.

The most primitive synthesis of transition metal perovskite oxides is through solid state sintering. The basic premise of this synthetic route consists of milling stoichiometric amounts of metal oxides or carbonates together and then calcinating the mixture at high temperatures. The resulting chemical reaction is based around the diffusion of ions, which is heavily limited by slow kinetics. The initial kinetics of the solid-state synthesis are relatively quick as the initial point of contact between the mixtures is high. However, the diffusion of ions after the initial contact is an extremely kinetically limited process, and so high calcination temperatures are required. Due to the intrinsic nature of the solid-state synthesis, the level of mixing and the particle size of the reactants are the main material factors in determining the properties of the final material. Despite the solid-state reaction synthesis of perovskite oxides being one of the simplest and inexpensive methods of catalyst production, the synthetic method is plagued by poor reproducibility, massive variety in particle size, and poor phase purity which is especially present in complexes with multiple atomic compositions (i.e., $A_{1-x-y}A'_xA''_yB_{1-z-a}B'_zB''_aO_3$ type complexes).[96] These catalytic limitations at the most fundamental level require wet chemical-based solutions to produce replicable, inexpensive, high performance electrocatalysts for oxygen evolution anodes.

3.1.1 Sol-gel Synthesis

Sol-gel synthesis is a wet chemistry technique widely utilised in materials chemistry for synthesising nano materials, especially oxides which makes it an ideal production route for perovskite oxide oxygen evolution electrocatalysts. The procedure involves the transformation of the solution of dissolved metal ions into a gel network containing both solid and liquid phases

(hence the term sol-gel). The dissolved metal ions are mixed with a chelating agent such as an alcohol, which forms a colloid through condensation and hydrolysis reactions. Depending on the materials used, the colloid can range in size from a polymer network of interconnected chains, down to single colloidal pockets distributed in the solvent.[97]

General sol-gel processes as described above are ideal for binary oxides such as SiO_2 and MnO_2 as homogenisation of the colloidal particles does not pose an issue as due to the fewer components present. For ternary oxides such as ABO_3 perovskite oxides, the homogeneity of the particles is significantly more important, as a non-homogenous distribution of ions in the sol-gel may lead to phase discrepancies in the final product. To combat potential phase purity issues, the sol-gel process must be modified to factor in steric immobilisation of the ions. Steric immobilisation is an effective way of avoiding the formation of multiple binary oxides which involved imprisoning the metal ions in a large chelate complex to form a large polymer network. The chelating agent used in the synthesis method to create the perovskite oxides was citric acid, as it is much larger than other commonly used chelating agents like alcohols, which sterically entangles the aqueous cations to create a gel. This term is often coined the Pechini process.[98, 99]

Once the gel has been formed in both standard sol-gel and Pechini synthesis, the solvent is removed through gradual heating. Once most of the solvent has evaporated, the resulting gel is combusted at around 300 °C to remove any organic compounds from the material. The material is then transferred into a muffle furnace and undergoes sintering, the temperature of which is dependent on the desired product. The sol-gel materials investigated in this thesis was sintered at 800 °C for 6 hours with a heating rate of 2 °C min^{-1} for single perovskite oxides, and 1100 °C for 12 hours with a heating rate of 5 °C min^{-1} for double perovskite oxides.

Sol-gel synthesis of ceramic materials, in particular transition metal-based perovskite oxides is the preferred synthesis method over solid state synthesis for many reasons. However, there are two distinct advantages of the procedure when compared to solid state synthesis. The first is that this synthesis route allows the use of much lower sintering temperatures, as solid state synthesis is mass transfer limited at the intersection of the grains of the reactant materials, whereas this is not the case in a sol-gel environment as the ions are held in a combustible polymer matrix.[100]Secondly, the sol-gel synthesis route allows relatively simple production of ternary and quaternary metal oxides, as the precursor gel stage allows for the system to remain amorphous

until the material begins to nucleate. This is important as early nucleation and growth of intermediate phases may lead to irregular particle sizes and the formation of significant levels of impurity phases, thus giving a higher degree of control over the properties of the final material product.[101]

3.1.2 Hydrothermal Synthesis

A lesser utilised synthesis technique for metal oxide materials is hydrothermal synthesis. This is similar to the sol-gel method, but instead of simply combusting the gel before sintering the solution is heated in a sealed autoclave before being sintered. The use of an autoclave can drastically reduce the temperature required, as during the heating process the internal solution is put under increased pressure. This internal pressure allows for interesting a novel grain morphology which researchers have used to produce cubed, yolk-shell, and porous hollow sphere structured materials among others.[46, 52, 102]

Although the specifics of the hydrothermal synthesis of the perovskite oxide will be discussed within the relevant chapter, the overall procedure is very similar to that of the sol-gel process. Metal cations are spread homogenously throughout an aqueous body and in the presence of chemicals which aid the reaction. In the case of the pure sol-gel route, polydentate ligands such as citric acid are utilised due to the large steric nature ligand, but in the case of hydrothermal methods a mineraliser is utilised instead. The purpose of a mineraliser in this case is to provide a nucleation point for dissolved metal ions to crystallise from, essentially acting as a catalyst in the crystal growth. In this thesis, KOH was used as a mineraliser, although different mineralisers will lead to different particle size and morphology.

The synthesis technique utilised in the hydrothermal synthesis of perovskite oxides involved the dissolution of metal cation in water with an excess of KOH. This solution was allowed to stir, was transferred to a autoclave, and place in an oven at 180 °C for 24 hours. The resulting slurry was then washed with deionised water to remove any KOH, and the resulting material was sintered in a muffle furnace for 2 hours at 800 °C in order to increase phase purity.

3.2 Powder X-Ray Diffraction – X-Ray Generation and Sample Optics

3.2.1 Introduction

Powder X-Ray diffraction is utilised heavily in the investigation of crystalline solids as a structural characterisation determination technique. The basic principle of powder X-ray diffraction, often shortened to simply XRD, is that high energy X-Rays of a specific wavelength are generated and then diffracted by a crystalline material onto a detector. From this, a powder diffraction pattern is gathered, and this powder diffraction pattern can be analysed through procedures such as Rietveld refinement to extract information about various crystalline properties, such as grain size, crystal volume, atomic positions, lattice parameters and space group. X-ray diffraction is crucial to the research displayed in this thesis, as it is used as proof of various material hypotheses. As such an in-depth discussion on the various aspects of X-ray diffraction and crystallography in general are provided below.

3.2.2 Generation of X-rays

The X-rays used in XRD are generated within an X-ray tube by first generating electrons by heating a tungsten filament and accelerating these electrons at high velocity towards an anode material. Different anode materials are used to generate different wavelengths of X-ray. As the anode material used to generate the X-rays has to be metallic and have a relatively high melting point, the materials selection is limited. The wavelengths of X-rays generated generally ranges from 0.5 to 2.5 Å. The most common anode material used as an X-ray source is copper, so this section will discuss XRD instrumentation which has a Cu anode source. As electrons from the filament bombard the Cu anode, X-rays are produced via 2 simultaneous processes. In one process, X-rays are produced due to the electron being slowed and reflected by the Cu atomic nucleus in a process known as inelastic scattering. The slowing of the electron produces radiation known as bremsstrahlung (or braking radiation). The other process is more integral to XRD analysis, as this produces high-energy characteristic X-rays. As electrons from the filament collide with the Cu atoms in the anode, an electron from a base shell is ejected. This causes a cascade of electrons from the higher energy levels to fill the energy gap left behind, and in doing so energy is released in the form of a photon. This photon has a specific energy which is related to the distance between the quantised energy levels in the anode atoms, and will therefore be different

with different material anodes, which makes it possible to change the energy of the X-rays by changing the anode material.

Both of these processes can be observed in an X-ray spectrum of copper with the smooth lower intensity line arising from bremsstrahlung rays, and the sharp, higher intensity peaks can be attributed to the characteristic X-rays of Cu (Figure 7).
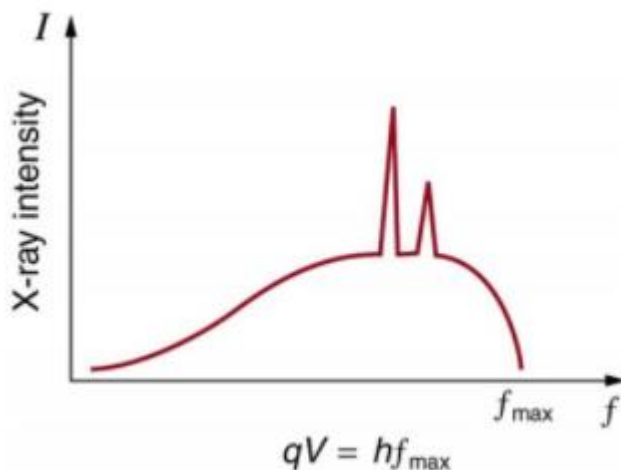
Figure 7 – X-ray spectrum showing bremsstrahlung and characteristic X-rays.

As discussed, as electrons collide with Cu atoms some energy is transferred. This energy excites one or more electrons temporarily into a higher energy sub shell. As the electron(s) fall back to fill the hole a photon of a certain energy is released. The energy of this photon is dependent on the energy gap between shell, which is unique per element, and which shell to shell transition the electron undergoes. The highest energy photons are emitted when a K 1s (n = 1) electron is excited into a L 2p (n = 2) or M 3p (n = 3) orbital and then returns. When a 2p to 1s transition occurs, the resulting radiation is known as Kα radiation. However, due to spin coupling in the 2p orbital there are two very similar energy photons that are released which are designated as $K\alpha_1$ and $K\alpha_2$. Similarly, a 3p to 1s electron transition results in the release of higher energy Kβ radiation. Figure 8 shows some of the allowed transitions between orbitals and the resulting radiation.
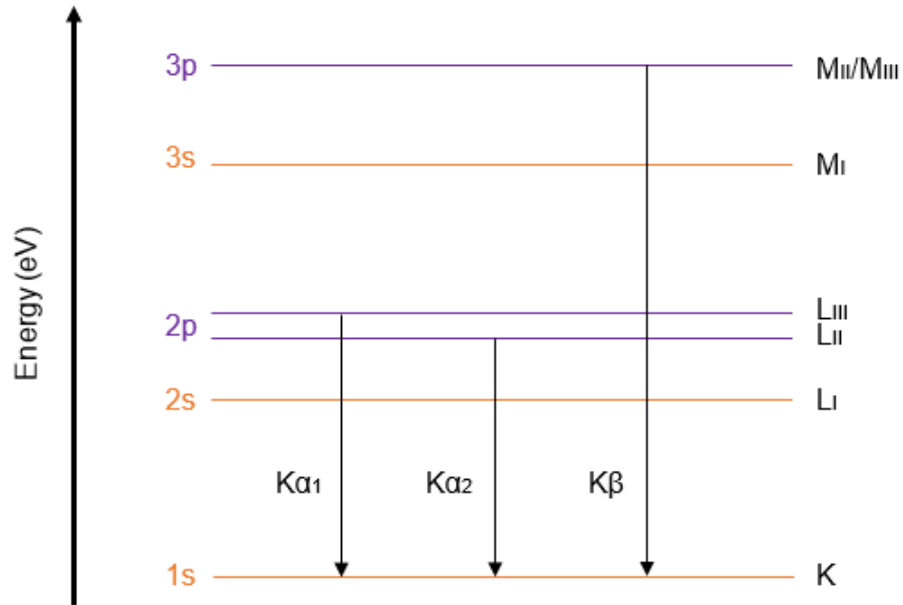
Figure 8 – Displaying some of the allowed electron transitions which results in X-rays with different wavelengths labelled as Kα and Kβ radiation.

As previously discussed, the wavelength of the electromagnetic photons released as a consequence of these electron transitions is characteristic to the energy gap between the orbitals in the atom from which they originated. The wavelengths of the electromagnetic radiation generated from a copper anode material are λ = 1.54056 Å ($K\alpha_1$), λ = 1.54439 Å ($K\alpha_2$), and λ = 1.39442 Å ($K\beta$). The peaks associated with $K\alpha_1$, $K\alpha_2$, and $K\beta$ can be seen in Figure 9.
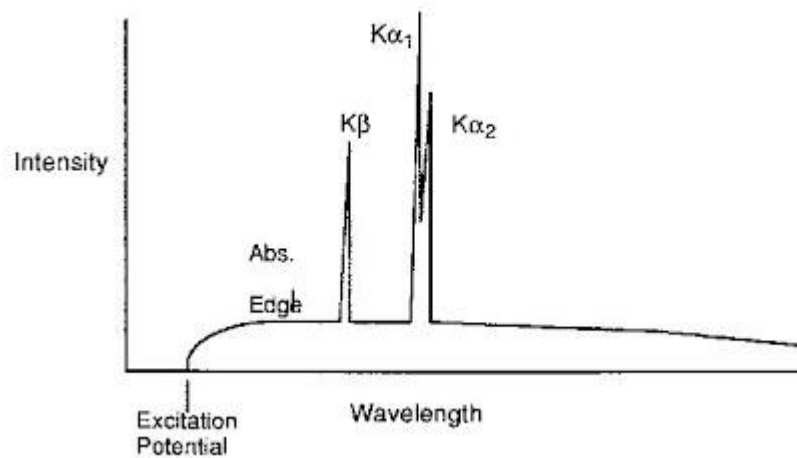
Figure 9 – Plot displaying different Bragg peaks of the same reflection and their relative intensities caused by different X-ray energies.

The positioning and relative intensity of the $K\alpha_1$ and $K\alpha_2$ peaks are integral to ensure that the instrument is operating correctly, as these peaks have fundamental characteristics. In a typical XRD pattern, the $K\alpha_1$ peak occurs at a lower scattering angle than the $K\alpha_2$ peak. This is due to Bragg's law (equation 1), which shows that the wavelength is proportional to the scattering angle. This shows that the higher wavelength $K\alpha_2$ peaks occur at a wider diffraction angle than the shorter wavelength $K\alpha_1$ peak.

$$n\lambda = 2d_{hkl} \sin \theta \tag{1}$$

Where n is a positive integer denoting the reflection order (non-integer values of n would lead to destructive scattering which would not lead to a Bragg peak), λ is the wavelength of the incident X-ray, d_{hkl} is the interplanar lattice spacing between Miller planes, hkl are the Miller indices, and θ is the diffraction angle with respect to the scattering planes. The ratio between the relative intensity of the $K\alpha_1$: $K\alpha_2$ should always be 2:1 due to spin orbital splitting of core levels.[103] Core levels are generally designated 3 numbers, denoted as n l and m_s where n is the principal quantum number, l is the angular momentum (or azimuthal) quantum number, and m_s is the total angular momentum number which is calculated by:

$$m_s = l + s \tag{2}$$

Where s is the spin angular momentum number and has a value of ± ½. This spin orbit splitting is the mechanism behind the difference in the core shell energy level differences in Figure 8. For all orbital levels except from the s orbitals (as l = 0) give rise to 2 degenerate orbital states with different energies in a process known as spin orbit splitting.[103] The 2 energy states that arise from this splitting are degenerate due to the 2 different total angular momentum numbers (m_s). As state in equation 2 if the value for the angular momentum quantum number is equal to 1, as is the case in a p orbital, then m_s will give rise to 2 sub-orbitals, a lower energy ½ orbital and a higher energy $\frac{3}{2}$ orbital. As 6 electrons are required to fill the p orbital, 4 electrons occupy the $\frac{3}{2}$ orbital, and the remaining 2 electrons will inhabit the $\frac{1}{2}$ orbital. As $K\alpha_1$ radiation comes from an electron transition from the $\frac{3}{2}$ orbital, and $K\alpha_2$ arises from a transition from the $\frac{1}{2}$ orbital, there will be 4 electrons contributing to $K\alpha_1$ radiation compared to 2 for $K\alpha_2$ which gives rise to the 2:1 ratio between the relative intensities of $K\alpha_1$: $K\alpha_2$.

3.2.3 Optics and Sample Diffraction

As shown in the previous section, after the X-rays are generated, the incident beamline passes through a series of primary optics, irradiates the sample (held in a goniometer), then passes through a set of secondary optics before hitting the detector. Each of these optics plays a significant role in the data that is gathered, so optimum optics are imperative for high quality data collection. The primary optics consist of the incident X-ray beam passing through soller slits, beam mask, followed by divergence and anti-scatter slits. The primary optics are responsible for altering the incident beam in such a way that it is more useful for diffraction experiments, for example to increase the resolution of the final diffraction pattern.

Soller slits are designed in such a way that only X-ray waves that are parallel to one another can pass through. This is achieved through multiple repeat parallel blades made from a material that does not fluoresce in the region of interest, and absorbs the X-ray radiation that collides with it, thus limiting the non-parallel waves. One of the main benefits provided by soller slits is a reduction of the axial divergence. Whilst there are optics to control the divergence of the incident beam in the diffraction plane, the incident beam can also diverge perpendicular along the goniometer which gives rise to axial divergence. As mentioned, soller slits control the width of the beam. Because of this the soller slits are used to reduce the axial divergence. One of the ways axial divergence is manifested in the diffraction pattern is by peak asymmetry on the lower 2θ side of the peak, allowing for higher resolution diffraction data. The equation for calculating the displacement the axial divergence has on the peak position is shown in equation 3. However, the consequence of utilising soller slits is a reduction in the peak intensity as the soller slits do block some of the desired radiation from passing through. To get well defined peaks there is sometimes another soller slit placed on the secondary optics, although this is rare as often the reduction in peak intensity is not worth the increase in peak resolution.

$$\Delta 2\theta = \frac{Q_1 \cot(2\theta)\, h^2}{6R^2} \tag{3}$$

Where Q_1 is a complex function of q, h is the width of the irradiated surface (same as beam height) and R is the radius of the goniometer.

The shape of the parallel incident X-ray beam is then altered through beam masks and anti-scatter slits. Different sizes of beam mask and slits are used to optimise how much of the

sample is irradiated by the incident beam. The beam mask is used to adjust the width of the irradiated area, and the divergence and anti-scatter slits are used to adjust the length of the irradiated area. An ideal incident beam will irradiate the maximum possible area of the sample. However, the area should not be so large that the beam irradiates the sample holder. If this happens it is called beam spill and can cause non-sample specific peaks to appear in the diffraction pattern.

Powder XRD is used in order to determine the structure of a crystal. A crystal can be defined as a material with atoms or ions arranged in a three-dimensional highly ordered structure, forming a crystal lattice. The smallest repeating unit of this crystal lattice which encompasses all the structural characteristics repeated by indefinite repetitions is called the unit cell. Powder XRD utilises the fundamental process of elastic scattering of monochromatic X-ray radiation caused by interactions with the electrons of the atoms or ions in a crystal lattice. As the interatomic distances in the crystal lattice and the wavelength of the X-ray radiation are on the same order of magnitude, when the X-rays interact with the electrons in the crystal and the waves are scattered constructively, a diffraction pattern can be recorded. The pattern gained from XRD analysis of a crystal can show the characteristics of said crystal, as the pattern will be determined by the orientation of the crystal structures, the atomic make-up of the structures, and the interplanar distance between crystal layers. The lattice spacing can be determined by Bragg's law[104], which is shown in equation 4.

$$n\lambda = 2d_{hkl}\sin\theta \tag{4}$$

Where n is a positive integer showing the order of reflection, λ is the wavelength of the incident X-ray radiation, d_{hkl} is the interplanar lattice spacing between Miller planes. hkl is defined by the Miller indices, and θ is the incidence angle of the incoming X-ray radiation.
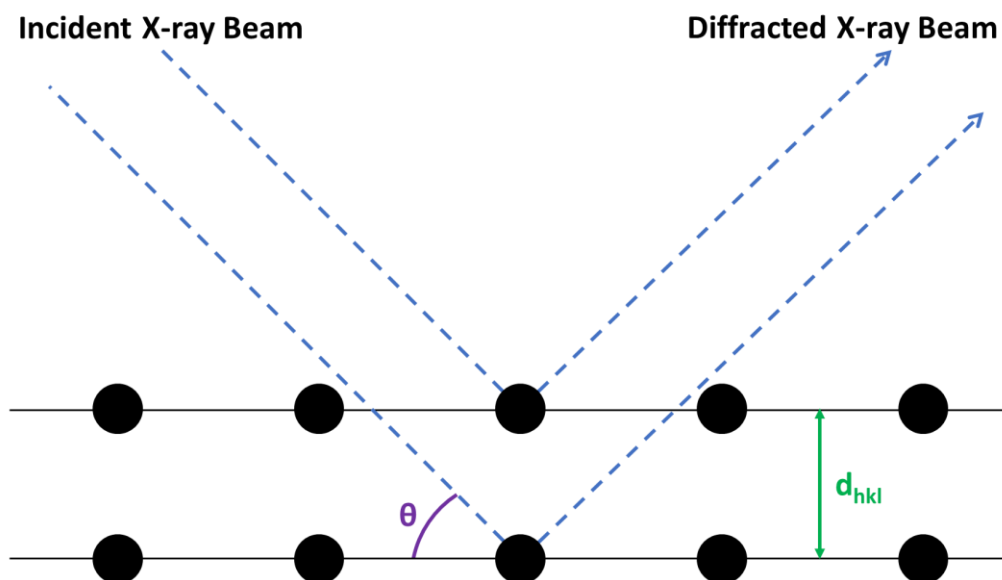
Figure 10 – Visual representation of Bragg's Law, which describes the interaction between X-rays and atoms in a crystal during X-ray Diffraction. Large black circles represent atoms, blue dashed lines indicate incident and diffracted X-ray beams. The interplanar spacing is denoted as d_{hkl}, and the diffraction angle is denoted as θ measured in degrees (°).

A visual representation of Bragg's law in action is illustrated in Figure 10. This illustration shows that there are a limited number of directions where X-rays will have constructive interference which satisfies Bragg's law (when the diffraction order (n) is an integer), whereas most of the scattering will cause destructive interference and therefore will not show as a reflection peak in the powder diffraction pattern. This limitation explains why for a certain crystalline material, the diffraction pattern will be characteristic. During the XRD analysis, the diffraction is measured across a range of incidence angles in order to produce a pattern with peaks with varying intensity as a function of θ. As the diffraction order (n) is always an integer, λ is the wavelength of the X-ray radiation, and the scan is obtained over known values of θ, the interplanar spacing (d_{hkl}) can be determined from the position of the reflection peaks.

3.3 Powder X-Ray Diffraction – Crystal Systems and Bravais Lattice

3.3.1 Introduction

As discussed in the introduction to this section, powder X-ray diffraction is essential for determining specific structural properties of the crystalline solids which are central to this research work. Analysing the information gathered from an XRD powder diffraction pattern (discussed later on in this chapter) requires use of certain techniques and terminology from the field of crystallography. The field of crystallography, in particular the full attribution of how space

and lattice groups are determined, is too large of a field to cover entirely in detail within this thesis. However, an understanding of the 14 Bravais lattices is arguably the most important crystallographic concept used in the characterisation of solid crystalline electrocatalyst materials, and so a discussion of this is provided below.

3.3.2 Bravais Lattices

There are a total of 14 Bravais lattices in three-dimensional space, which are separated into 7 different lattice groups, or primitive lattices; triclinic, monoclinic, orthorhombic, tetragonal, rhombohedral (also referred to as trigonal), hexagonal and cubic. These lattice groups described the three-dimensional shape of the unit cell of the lattice. The unit cell is the space that, when translated through a subset of vectors as described by equation 5, will fill lattice space without any overlap with other atoms, or leave any previously filled space empty.[105]

$$\boldsymbol{R} = n_1 a_1 + n_2 a_2 + n_3 a_3 \qquad (5)$$

Where a_1, a_2, and a_3 are translation vectors, and n_1, n_2, and n_3 are a set of arbitrary integers (which include zero and negative numbers), and **R** is the set of all possible lattice points. In simpler terms, the unit cell is the smallest set of repeating points in a crystal which can be used to build the entire crystal when stacked in any three-dimensional way. As the crystal can be represented by stitching together of unit cells, it is therefore logical to say that any crystalline material will have a unit cell, and as the primitive lattice is the smallest possible group, the unit cell will always be in some configuration of the 7 primitive lattices listed above. However, in some cases it may be possible to assign multiple different primitive lattice shapes to a crystal (as shown in two-dimensions in Figure 11.
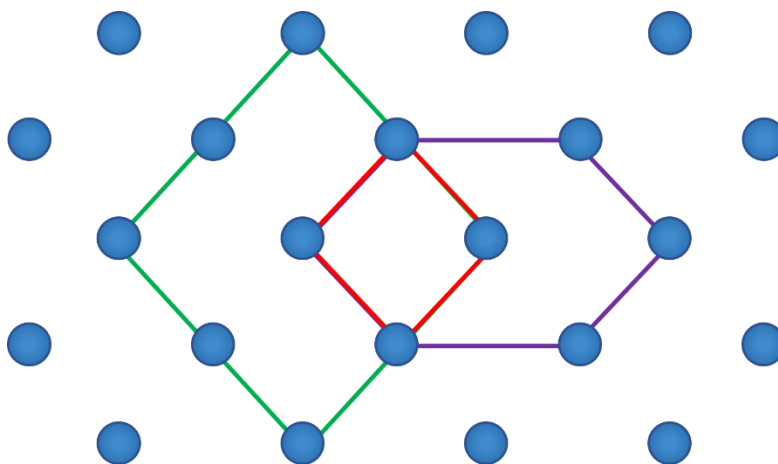
Figure 11 – Two-dimensional example showing how it may be possible to assign multiple primitive lattice shapes to the same crystal configuration.

All 3 shown unit cells (shown in red, green, and purple) are equivalent and appropriate unit cells, as they fulfil the condition that by pure translation operations, the whole lattice point pattern can be generated. However, there are some general rules of thumb to consider when assigning a unit cell (both in 2 and 3 dimensions). These are:

- The unit cell should be the smallest appropriate shape, in that it has short lattice vectors. For example, the red unit cell is half the size of the green unit cell.

- The unit cell should represent the symmetry of the crystal. For example, the red unit cell as the lattice vectors are perpendicular to mirror planes of the lattice.

- Where possible, the unit cell should be orthogonal (which is indicative of high symmetry). For example, this is the case for the red and green unit cells, but not for the purple.

Using these rules, the red unit cell in Figure 11 is the most appropriate starting point for the unit cell of that crystal. Sometimes it is not possible to find a primitive unit cell which satisfies the rules listed above, so it is sometimes necessary to choose a centred unit cell, where there are atoms included in the unit cell that are not only at the corners. The addition of further lattice points into the unit cell gives rise to 7 more lattice systems, giving the combined 14 Bravais lattices.

3.3.3 Crystal System

As discussed, many different material characteristics can be defined from the diffraction pattern, and/or the resulting Rietveld analysis. Common reported characteristics include lattice

parameters, crystal volume, and fitting statistics. The lattice parameters can be calculated using the d spacing gathered from Bragg's law (equation 1), and the Miller indices (hkl) of the Bragg reflection. During this work, the 3 classes of lattice structure were cubic (a=b=c), tetragonal (a=b≠c), and orthorhombic (a≠b≠c), of which the equations used in calculating the lattice parameters of these crystal systems are shown in Table 2. The crystal volume is the product of the lattice parameters multiplied by one another.

Table 2 – Lattice parameter calculations for cubic, tetragonal, and orthorhombic lattice structures

Crystal System	Lattice Parameter
Cubic	$$\frac{1}{d_{hkl}^2} = \frac{h^2 + k^2 + l^2}{a^2}$$
Tetragonal	$$\frac{1}{d_{hkl}^2} = \frac{h^2 + k^2}{a^2} + \frac{l^2}{c^2}$$
Hexagonal	$$\frac{1}{d_{hkl}^2} = \frac{4}{3}\left(\frac{h^2 + hk + k^2}{a^2}\right) + \frac{l^2}{c^2}$$
Rhombohedral	$$\frac{1}{d_{hkl}^2} = \frac{(h^2 + k^2 + l^2)sin^2\alpha + 2(hk + kl + hl)(cos^2\alpha - cos\alpha)}{a^2(1 - 3cos^2\alpha + 2cos^3\alpha)}$$
Orthorhombic	$$\frac{1}{d_{hkl}^2} = \frac{h^2}{a^2} + \frac{k^2}{b^2} + \frac{l^2}{c^2}$$
Monoclinic	$$\frac{1}{d_{hkl}^2} = \frac{1}{sin^2\beta}\left(\frac{h^2}{a^2} + \frac{k^2 sin^2\beta}{b^2} + \frac{l^2}{c^2} - \frac{2hlcos\beta}{ac}\right)$$
Triclinic	$$\frac{1}{d_{hkl}^2} = \frac{1}{V^2}(S_{11}h^2 + S_{22}k^2 + S_{33}l^2 + 2S_{12}hk + 2S_{23}kl + 2S_{31}hl)$$ Where $$S_{11} = b^2c^2sin^2\alpha$$ $$S_{22} = a^2c^2sin^2\beta$$ $$S_{33} = a^2b^2sin^2\gamma$$ $$S_{12} = abc^2(cos\alpha.cos\beta - cos\gamma)$$ $$S_{23} = a^2bc(cos\beta.cos\gamma - cos\alpha)$$ $$S_{31} = ab^2c(cos\gamma.cos\alpha - cos\beta)$$ $$V^2 = a^2b^2c^2(1 - cos^2\alpha - cos^2\beta - cos^2\gamma + 2cos\alpha.cos\beta.cos\gamma)$$

3.4 Powder X-Ray Diffraction – Rietveld Refinement

3.4.1 The Powder Diffraction Pattern

Data gathered from powder X-Ray Diffraction is displayed in a powder diffraction pattern, generally as a plot of Bragg angle (2θ°) against intensity. This powder diffraction pattern can be thought of as a set of discrete diffraction peaks, plotted alongside a continuous background. The background measurement is normally factored out of calculations, and the analysis is focussed on the diffraction peaks in the powder diffraction pattern. There are 3 main parameters that can be used to describe the diffraction peaks, these are peak position, peak shape, and peak intensity. These parameters hold information about the crystal structure of the material, the properties of the sample, and the effects from instrumental parameters. The relationship between these parameters and crystal structures is show in Table 3.[106] It should be noted that there may be other parameters that affect the position, shape and intensities of the Bragg peaks.

*Table 3 – Properties of powder diffraction patterns and the relation to crystal structure, sample parameters, and instrumental parameters. Parameters in **bold** are key parameters, italicised parameters may have a significant influence.*

Pattern Feature	Crystal Structure	Sample Properties	Instrumental Parameter
Peak position	**Unit cell parameters:** (a, b, c, α, β, γ)	*Absorption* Porosity	**Radiation (wavelength)** *Alignment* Axial divergence of beam
Peak shape	*Crystallinity* Disorder Defects	*Grain size* *Strain* *Stress*	**Radiation (spectral purity)** **Geometry** **Beam conditioning**
Peak intensity	**Atomic parameters** (x, y, z, B etc)	*Preferred orientation* Absorption *Porosity*	Geometry and configuration **Radiation (Lorentz, polarisation)**

Aside from the parameters listed in Table 3, the powder diffraction pattern will be strongly affected by structural parameters, especially the unit cell parameters, and the atomic make-up of the lattice (both the type of atoms and the positions of the atoms). These are the main components which make up a powder diffraction pattern. As the position of the Bragg reflections

has been discussed through Bragg's law earlier in this chapter, the following is a discussion of the peak intensity and peak shape parameters as listed in Table 3, as described by Pecharsky and Zavalij (2008).[106]

3.4.2 Peak Shape in Powder Diffraction

In order to obtain information about the crystal structure of the material from the powder diffraction pattern, an appropriate function is applied specifically for the peak shape. This function relies on the fact that the majority of Bragg peaks in a powder diffraction pattern are normally overlaps of multiple Bragg peaks. This is due to many different factors, including intrinsic parameters of the incident X-ray, for example, peak contributions from $K\alpha_1$ and $K\alpha_2$ radiation, and multiple reflections from equivalent planes such as (100), (010), and (001). The function that is used in order to extract information from these various Bragg reflections is know as the peak-shape function (PSF), which is a convolution of 3 separate functions. These are the instrumental broadening Ω, wavelength dispersion Λ, and specimen function ψ. The PSF is represented in equation 5, where b is the background function.

$$PSF(\theta) = \Omega(\theta) \otimes \Lambda(\theta) \otimes \psi(\theta) + b(\theta) \tag{5}$$

Where $\otimes$ denotes a convolution of 2 functions.

The instrumental broadening

(Ω) is, as the name suggests, related to the various features of a powder X-Ray Diffraction instruments such as: the optics and monochromator type used (discussed above), the position and geometry of the sample, and the type of material that is being analysed. The wavelength dispersion (Λ) accounts for variance in the wavelengths of the x-rays which can occur due to the material type and purity of the source anode, as well as the type of monochromator used. The final line shape function is the specimen (ψ) is arguably the most complex, due to contributions arising from multiple effects. The initial effect is those arising from dynamic scattering due to the existence of a finite width of the Bragg peaks. However, the majority of the effects for the specimen function arise from the make-up and physical properties of the material itself, which include properties such as grain size and strain which are well known to affect the width of the Bragg peaks, also known as broadening effects. These broadening effects are heavily correlated with the physical make-up of the material, and so the observed broadening of the Bragg peaks is often of interest to materials scientists. Specifically,

the effects that average grain size (τ) and microstrain (ε) have on peak broadening (β, measured in radians) is approximated through equations 6 and 7.

$$\beta = \frac{\lambda}{\tau \cdot \cos\theta} \tag{6}$$

$$\beta = k \cdot \varepsilon \cdot \tan\theta \tag{7}$$

Where k is a constant that is dependent on the definition of microstrain used, and β is the excess width arising from broadening, meaning the total peak width arises from the sum of the effects of the instrumental parameters and peak broadening (from material parameters). This relationship between peak broadening and material properties is important during the refinement of X-ray powder diffraction data, as will be discussed after establishing how the shape of the Bragg peaks are convoluted (or fit) during Rietveld refinement.

Utilising this knowledge of the various parameters that effect the peak shape in powder diffraction patterns, a function can be designed to be used in a model which will fit the peak shape of the powder diffraction pattern. There are a few different methods of developing this function, depending on what information is of interest and available. All powder X-Ray diffraction scans and their subsequent refinements used in this research what is known as the fundamental parameters approach, in which all aspects of the peak-shape function (equation 5) are modelled using reasonable physical quantities, which are often brought about from a reference material, but this will be discussed later in the text.

3.4.3 Peak-Shape Functions

As described in section 3.4.2 above, the majority of powder diffraction patterns consist of overlapping Bragg reflections. This is manifested in the shape of an individual Bragg reflection peak (denoted as the kth peak), which is analysed using the peak-shape function (equation 5). Considering equation 5, it can be realistically stated that the total intensity (Y_i) at point i in the diffraction pattern is the sum of the contributions arising from m number of overlapped peaks and the background (b_i), where i is a single measured point in the specific Bragg peak k. This can be represented by equation 8.

$$Y_i = b_i + \sum_{k=1}^{m} I_k \left[y_k(x_k) + 0.5 y_k(x_k + \Delta x_k) \right] \tag{8}$$

Where I_k is the intensity of Bragg peak k, $x_k = 2\theta_i - 2\theta_k$, and Δx_k is the difference between the Bragg angles of the Kα$_1$ and Kα$_2$ peaks. As the intensity of the Bragg peak (I_k) functions as a multiplier in equation 8, the shape of the peak can be analysed independently of the intensity by fitting various peak-shape functions to the data.

There are many different practical functions (y) that can be used to fit the peak shape, the most common and simplest of which are the Gaussian function and the Lorentzian function. These are described in equations 9 and 10 respectively.

Gaussian:

$$y(x) = G(x) = \frac{C_G^{1/2}}{\sqrt{\pi H}} \exp(-C_G x^2) \tag{9}$$

Lorentzian:

$$y(x) = L(x) = \frac{C_L^{1/2}}{\pi H'} (1 + C_L x^2)^{-1} \tag{10}$$

Where:

- $H = (U \tan^2\theta + V \tan\theta + W)^{1/2}$. This is the full width at half maximum as a function of Bragg angle (θ) for Gaussian functions, known as the Caglioti formula, and U, V and W are the Caglioti parameters which are instrumental parameters.[107]
- $H' = X/\cos\theta + Y \tan\theta$. This is the full width at half maximum as a function of Bragg angle (θ) for the Lorentz function, where X and Y are free variables.
- x is the Bragg angle at point i in peak k, divided by the FWHM of the peak. Can be shown as: $x = (2\theta_i - 2\theta_k)/H_k$.
- θ_i = Bragg angle at point i.
- θ_k = Calculated Bragg angle of Bragg peak k.
- $\frac{C_G^{1/2}}{\sqrt{\pi H}}$ = Gaussian function normalisation factor such that $\int_{-\infty}^{\infty} G(x)dx = 1$.

- $C_G = 4\ln(2)$.

- $\frac{C_L^{1/2}}{\pi H'}$ = Lorentzian function normalisation such that $\int_{-\infty}^{\infty} L(x)dx = 1$.

- $C_L = 4$.
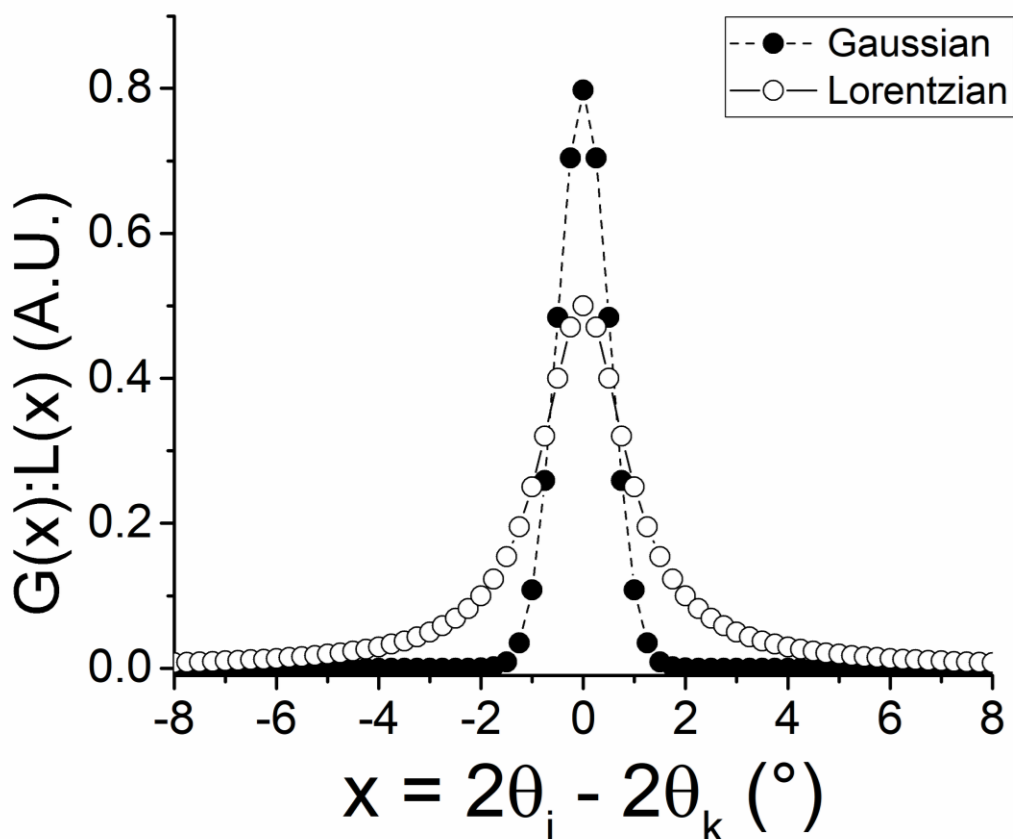
Figure 12 – Plots of both the Gaussian and Lorentzian peak-shape functions highlighting the difference in the distributions

The distributions of both Gaussian and Lorentzian peak-shape functions are shown in Figure 12 where it is clear to see how the two functions differ from one another. For example, the Lorentzian function has a lower maximum intensity but has tails spreading towards the base, but the Gaussian function is almost the opposite, with no tails at the base of the peak but a noticeably higher maximum peak intensity. However, it is unlikely that the diffraction peaks in an X-ray diffraction powder diffraction pattern will be described well by pure Gaussian or Lorentzian distributions, and in reality, most peaks are somewhere in between. This could cause an issue as structural information may be lost or incorrect if the peak-shape function cannot accurately describe the distribution of the peak. The solution to this problem would be to convolute both Lorentzian and Gaussian peak-shape functions to determine their respective contributions to the

shape of the Bragg peak. It is for this reason that many powder X-ray diffraction patterns utilise a peak-shape function that is a linear combination of Gaussian and Lorentzian functions known as the pseudo-Voigt peak-shape function.

The pseudo-Voigt peak-shape function can be described as a linear combination of the Gaussian and Lorentzian functions shown in equations 9 and 10 respectively. The combination of these two functions is shown in equation 11.

$$y(x) = PV(x) = \eta \frac{C_G^{\frac{1}{2}}}{\sqrt{\pi H}} \exp(-C_G x^2) + (1 - \eta) \frac{C_L^{\frac{1}{2}}}{\pi H'} (1 + C_L x^2)^{-1} \qquad (11)$$

It can be seen in equation 11 that the pseudo-Voigt function is a combination of Gaussian and Lorentzian functions with an additional parameter denoted as η. This η parameter is the pseudo-Voigt mixing parameter and can be defined in equation 12:

$$\eta = \eta_0 + \eta_1 2\theta + \eta_2 2\theta^2 \qquad (12)$$

The pseudo-Voigt mixing parameter (η) is a value between 0 and 1, where 0 is pure Lorentzian and 1 is pure Gaussian in nature. This allows for appropriate fitting of most Bragg peaks found in powder X-ray diffraction when compared to pure Gaussian or Lorentzian.

As discussed earlier in this chapter, the relationship between the FWHM and peak broadening with material characteristics such as grain size (equation 6) and microstrain (equation 7) is an important one to consider when attempting to extract structural information from X-ray powder diffraction patterns. With the knowledge of the pseudo-Voigt distribution function as discussed above, an equation to be used during peak shape refinement to attempt to quantify the grain size and microstrain of the crystalline sample can be determined. In order to understand the FWHM of the Bragg peaks, the Bragg angle at which the peak maximum lie should be determined. This is taken into consideration in the Gaussian, Lorentzian, and pseudo-Voigt peak-shape functions (equations 9, 10, and 11 respectively) by the x parameter. As x is the Bragg angle of data point i in peak k divided by the FWHM (H), the Bragg angle of the maximum peak intensity is the point in which $x = 0$ and $2\theta_i = 2\theta_k$, which means that the FWHM (H) parameter will determine the value of x. The FWHM (H) varies with different peaks depending on the Bragg angle (θ), this dependence is represented by the peak-broadening function shown in equation 13.

$$H = \sqrt{U \tan^2\theta + V \tan\theta + W} \qquad (13)$$

Where U, V, and W are peak broadening parameters that are refined during the Rietveld process, which allows determination of the grain size and the microstrain.

3.4.4 Peak Intensity in Powder Diffraction Patterns

The final feature which holds important structural information in the powder diffraction is the intensity of the Bragg peak. As seen in Table 3, there are 3 classes of features that can affect the intensity of the powder diffraction peak. These are grouped as crystal structure factors, which are as follows:

- Crystal structure parameters. These arise from the crystal structure of the material (atomic coordinates, thermal parameters etc).

- Sample parameters. These are effects from the sample being measured (grain size, microstructure, sample size etc). These contributions have some overlap with the peak shape, as the peak-shape distribution function will effect the peak intensity (Figure 12).

- Instrumental parameters. These are related to the different possible instrumental set-up (Optics and monochromator settings, radiation properties such as anode material and instrumental power etc).

However, the parameters listed above do not have an equal effect on the determination of the Bragg peak intensity. By far the crystal structure is considerably more crucial in determining in peak intensity is the Bragg peak, and the instrumental and sample parameters can be considered as having auxiliary effects. As shown in Table 3, the crystal structure factors are related to the atomic structure of the crystal unit cell such as the atomic type, position, thermal motion, and lattice site occupancy. Ensuring that the peak intensity, as well as the peak shape, is defined correctly is critical in order to extract accurate structural information from the powder diffraction pattern in Rietveld refinement procedures.

The peak intensity is often referred in the literature as the peak intensity (Y_{max}). The peak intensity can be a useful metric for specific applications, the most well utilised of these is in comparing the measured diffraction pattern to a database in order to provide an estimate of the material parameters such a space group and crystal system using programmes such as GSAS or X'Pert Highscore.[108, 109] However, due to the multiple factors that can affect the peak intensity,

the Y_{max} alone is not an appropriate parameter for extraction of structural information from the powder diffraction pattern. A more appropriate description of the peak intensity is the area under the Bragg peak, as even with changes from the peak broadening etc, the area under the peak will stay relatively unchanged. Logically this indicates that the peak intensity function can be applied as a multiplying function to the peak-shape function, meaning that the area under the peak is the true value of peak intensity, rather than the simplified version of using the peak intensity at maximum (Y_{max}). The intensity measured from the area under the Bragg peak is sometimes referred to as the integrated intensity, however for the rest of this thesis the integrated intensity will be referred to as simply the intensity and is denoted as I_{hkl}.

During the Rietveld refinement process the intensity of a Bragg peak is measured by a sum of profile intensity, minus the effects from the background. The profile intensity (Y_i) is the measured intensity at point i, which is generally given a value based on where the point is in the pattern ($i = 1$ is the first measured data point in the pattern and so on). Therefore, the calculation used to quantify the intensity of a Bragg peak is shown in equation 14:

$$I_{hkl} = \sum_{i=1}^{j} (Y_i - b_i) \tag{14}$$

Where j is the total number of measured data points, and b_i is the contribution from the background.

However, whilst the above discussion highlights how the intensity of the Bragg peaks is measured, it is important to understand the factors that contribute to the intensity. The intensity (I_{hkl}) is a function of many different parameters, from the atomic structure of the sample to various instrumental parameters, a comprehensive function for showing the various contributing factors to the intensity is shown in equation 15, and a brief overview of the various parameters will be provided.

$$I_{hkl} = K \times m_{hkl} \times L_\theta \times P_\theta \times A_\theta \times T_{hkl} \times E_{hkl} \times |F_{hkl}|^2 \tag{15}$$

Where:

- K is the scale factor. This is essential in Rietveld refinement as this parameter is used to normalise the experimentally measured intensities with absolute calculated intensity. The absolute calculated intensity is the total intensity which

is scattered by one unit cell. This means that the scale factor is constant for a specific crystal phase, and has contributions from the number, spacing, and state of the atoms in the unit cell.

- m_{hkl} is the multiplicity factor, which accounts for the presence of symmetrically equivalent reflections.
- L_{θ} is the Lorentz multiplier which accounts for the diffraction geometry.
- P_{θ} is the polarisation factor, which accounts for the partial polarisation of the X-ray wave by the sample.
- A_{θ} accounts for any absorption of the incident and diffracted beams.
- T_{hkl} accounts for deviations in the total randomness of the grain orientations, known as preferred orientation.
- E_{hkl} is the extinction factor, which is so small in powder diffraction that it can essentially be ignored.
- $\mathbf{F}_{hkl}$ is the structure factor. This accounts for the type of atoms and their coordinates, as well as lattice site occupancy and thermal parameters.

The hkl subscript indicates the parameter is a function of the relevant reciprocal lattice vector, and the θ subscript indicates the parameter is a function of the Bragg angle.

3.5 Refinement – Least Square Fitting (LSF)

As discussed, material characteristics can be obtained through computational fitting of a model to observed powder diffraction data. In this study the refinement method used is Rietveld method, which is a least square fitting method (LSF). In order to understand the methodology of Rietveld refinement, it is first useful to examine LSF in general, as well as what makes a 'good' fitting.

Quantifying how good of a fit the model data is to the observed data in LSF refinements is still a topic of debate amongst crystallographers and materials scientists. There is no one parameter that can accurately describe and compare every possible variation of LSF fitting. However, there are a variety of accepted fitting statistics that can give a good insight to the refinement, although they can vary slightly from field to field. Nevertheless, these fitting statistics

(or R-factors) provide an insight into if the model is appropriate for the observed data, and how well the model can determine crystal parameters of a material.

Diffraction data is fundamentally a plot of intensity values measured at a specific set of scattering vectors, given as °2θ. Intensity factors can be denoted as $y_{o,i}$ where o, i indicates the observed intensity value (o) taken at point 2θ$_i$ (i). A LSF refinement will estimate the standard uncertainty of $y_{o,i}$, which can be denoted as $\sigma[y_{o,i}]$. As discussed, LSF refinement method fits a model to observed data. This means that there will be two separate standard uncertainties to take into consideration in the fitting statistics, the computed values (denoted by a subscript c), and the observed values (denoted by a subscript o). The fitting algorithm used in LSF refinements attempts to optimise the model function to minimise the weighted sum of square differences between the observed and computed values (equations 16 and 17).

$$\sum_i w_i (y_{c,i} - y_{o,i})^2 \tag{16}$$

Where w_i is the weighting. Due to the statistical nature of the data fitting, the smallest uncertainties are given when the weighting is equal to the reciprocal of the square of the standard uncertainty (equation 6).[110, 111]

$$w_i = \frac{1}{\sigma[y_{o,i}]^2} \tag{17}$$

One of the simpler, but still incredibly useful fitting statistics is the weighted profile R-factor, commonly denoted as R_{wp}, which builds on the concepts used by the fitting algorithm (equations 16 and 17) by scaling these values by the weighted intensities (equation 18).[112]

$$R_{wp}^2 = \frac{\sum_i w_i (y_{c,i} - y_{o,i})^2}{\sum_i w_i (y_{o,i})^2} \tag{18}$$

In an ideal scenario in which the model perfectly predicts the true observed intensity values ($y_{o,i}$), then the following would be true:

$$(y_{c,i} - y_{o,i})^2 = \sigma[y_{o,i}]^2$$

And

$$w_i (y_{c,i} - y_{o,i})^2 = 1$$

Assuming the values for $\sigma[y_{o,i}]$ are correct, then the resulting R_{wp} would be the best possible value obtainable from that data. The value resulting from this scenario is in fact another

fitting statistic known as the expected R-factor (R_{exp}). If the number of measured datapoints in a diffraction pattern is denoted as N, then R_{exp} can be calculated through equation 20.[112]

$$R^2_{exp} = \frac{N}{\sum_i w_i (y_{o,i})^2} \qquad (20)$$

In terms of pure statistics, then N should technically be the number of measured points minus the number of refined parameters. However, as the number of measured datapoints is orders of magnitude higher than the relatively small number of refined parameters, it will not have a significant impact on the value of R^2_{exp} and so can essentially be ignored.

A relatively common function found in statistics is chi-squared, which is often denoted as χ^2, which is a good measure of if there is a statistical difference between observed and expected values. Clearly this is a useful statistical measure during a refinement process. The chi-squared value is highly correlated to the goodness of fit (G) as G can be calculated from χ^2 = G^2.[113] Chi-squared is a function of 2 already defined parameters, as shown in equation 21.

$$\chi^2 = \left(\frac{R_{wp}}{R_{exp}}\right)^2 \qquad (21)$$

These fitting statistics give a good measure of the fitting of the model data to the observed diffraction data and allow a running observation as various parameters are refined. As a general rule of thumb, the values for statistics such as χ^2 should reduce during the refinement otherwise there may be external errors in the data and the data collection should be repeated.[113]

3.5.1 Rietveld Refinement Method

The refinement procedure proposed by Hugo Rietveld takes the principles of least square fitting and applies them to powder X-Ray Diffraction patterns. This provides the obvious advantage from generic least squares fitting of being able to determine specific material characteristics of crystalline materials. Like LSF, the basis of the Rietveld method is to refine a theoretical powder diffraction pattern until it matches observed data gathered from powder X-Ray diffraction. A condition of this refinement method is that some material parameters require reasonable approximations of the initial value. These parameters include properties such as space group, lattice parameters, crystal volume, and atomic coordinates and type. Fortunately for the modern-day crystallographer, mass databases such as the Inorganic Crystal Structure database (ICSD), Crystallography Open Database (COD), and the International Centre for Diffraction Data

(ICDD) exist, holding a plethora of peer reviewed crystal data for different materials. Using these data files as a starting approximation of the material parameters allows the refinement of structural parameters from powder diffraction data. The following is a discussion of the various considerations and operations that are involved in the Rietveld refinement of a powder diffraction pattern.

3.5.2 X-ray Diffraction Procedure

Diffraction patterns were acquired using a PANalytical X'Pert Pro MPD which was fitted with an X'Celerator detector. As discussed in Chapter 3.2.2 – Generation of X-rays, diffraction patterns were acquired by irradiating powder samples with Cu Kα X-ray radiation ($\lambda_{Average}$ = 1.5418 Å). The samples were scanned over a range of 5-120° in 2θ with a step size of 0.0334° and a nominal time-per-step of roughly 6 seconds. Fixed divergence and anti-scatter slits of 1/2 ° and 1° respectively were used with a 20 mm beam mask.

The powdered samples were first ground using a pestle and mortar so that the particle size was consistent. The powder was then loaded into either a backloaded sample holder, or onto a silicon wafer (depending on the amount of sample), which was made level with the top of the sample holder. The resulting diffraction patterns were then refined using Rietveld method of least squares[114] using TOPAS-Academic V6.[115, 116] This method is used to model the crystalline properties of the material by forming a theoretical structure and the resulting diffraction plot using a model, and then comparing this to the measured diffraction data.

Starting models using the appropriate space group were gathered from the Inorganic Crystal Structure Database (ICSD), the specific models used will be referred to during the discussion of results. Where appropriate, fundamental peak shape profiles[117] and X-ray form factors of Pr^{3+}, Sr^{2+}, Ba^{2+}, Fe^{3+}, Co^{3+} and O^{2-} were used. For each diffraction pattern, the Chebyshev polynomial and $\frac{1}{x}$ background, a zero error. Scale factors, and crystal size/strain were refined sequentially. The sum of occupancies of the A and B sites were constrained to unity. Isotropic temperature displacement factors for all atoms were refined independently. The cation positions were refined, followed by the oxygen positions.

3.6 Electrochemistry

Electrochemistry, at the most fundamental level, is studying the relationship between electrical potential and a chemical reaction. In comparison to traditional chemical reactions, during electrochemical reactions the electrons and ions are not exchanged directly between molecules, rather they are transferred through conducting circuits.

Electrochemical characterisation of oxygen evolution electrocatalysts are commonly performed in a 3-electrode cell. The catalyst material is drop cast onto the surface of a working electrode, then this, a counter electrode (Pt mesh), and a reference electrode (material depends on electrolyte conditions) are submerged into a liquid electrolyte solution. The electrodes are connected to a potentiostat which provides a set potential or current to the system and measures the resulting current or potential. A supply of potential whilst measuring current generated is known as operating in potentiostatic mode, whilst the reverse is known as galvanostatic mode. The current is generally measured as current density, and the potential is converted against the reversible hydrogen electrode (RHE) using the Nernst equation, which is discussed later in this chapter.

The oxygen evolution reaction (OER) is performed under electrolytic conditions, in that an external source of energy is used to drive the chemical reaction, which is the opposite of galvanic conditions in which chemical reactions provide sources of energy such as in oxygen reduction reaction (ORR) of fuel cells. This means that the basic principle of the electrochemical characterisation of the oxygen evolution reaction will involve providing an electrical potential to the system and measuring the levels of the resulting chemical reaction.

The endergonic nature of the water splitting reaction will have a minimum input energy required before the reaction will begin. This is known as the thermodynamic limitation of the water splitting reaction, and can be calculated using the standard reduction potentials (E^O) of the half-cell equations (equations 22 and 23) which are readily available in the literature.[118] It should be noted that these values are for water splitting are often reported in acidic conditions ([H⁺ = 1M]) however, the thermodynamic limitation is the same in alkaline conditions due to the Nernst equation which will be discussed further below.

$$Anode\ (ox): \quad 2H_2O \rightarrow O_{2\,(g)} + 4H^+_{(aq)} + 4e^- \quad\quad E^O_{Anode} = +1.23\,V \quad\quad (22)$$

$$Cathode\ (red): \qquad 2H^+_{(aq)} + 2e^- \rightarrow H_{2\ (g)} \qquad E^O_{Cathode} = 0.00\ V \qquad (23)$$
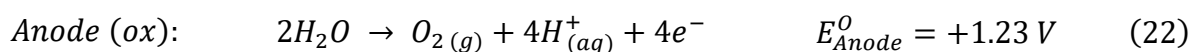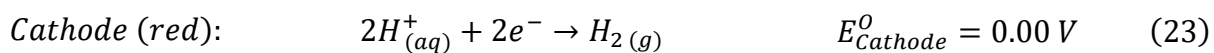
$$E^o_{Cell} = E^o_{Cathode} - E^o_{Anode} = -1.23\ V \qquad (24)$$

The overall thermodynamic limit for the water splitting reaction can simply be calculated by finding the net change as per equation 24, which gives the limiting potential for the water splitting reaction as -1.23 V. This means that at a minimum, 1.23 V of electrical potential must be provided to the electrolyser cell before the water splitting reaction can begin to proceed. However, due to other factors such as bubble formation, electrolyte impurities and resistance, material capacitance and so on, it is practically impossible for an electrolyser system to operate at the thermodynamic minimum. Therefore, the concept of overpotential (η) is often used when discussing electrochemical reactions and processes, as this is the amount of potential required for a specific occurrence minus the thermodynamic limit. For example, if a specific reaction occurs at an overpotential of η = 100 mV in an electrolyser system, the 'real' potential required is 1.33 V. The electrochemical performance of the oxygen evolution catalysts is tested using potentiostatic techniques, where a potential is applied to the system and the current response is recorded.

3.7 Electrochemical Impedance Spectroscopy (EIS)

Electrochemical Impedance Spectroscopy (EIS) is the measure of the impedance of a circuit created by an electrochemical cell. Impedance is analogous with resistance in direct current (DC) systems, but in alternating current (AC) systems. The primary difference between DC and AC systems is the direction of the current. In DC systems, the current flows in a single direction throughout the circuit, whereas in AC systems the current will periodically change direction. Direct current provides a much more consistent voltage delivery over short distances, which is ideal for applications such as batteries, fuel cells, and solar cells. Whereas, alternating current systems is the 'standard' power found from power stations and from sockets in the home. Alternating current is generated in power stations by spinning a metal coil in a magnetic field. The current will change direction as the coil passes from one magnetic pole to the other, and this defines the properties of the current generated. Assuming the rotation of the coil is a consistent

speed, the current produced by an AC system can be described by a sinusoidal wave. This is the fundamental distinction between DC and AC currents.

As the electrochemical nature of the oxygen evolution reaction electrocatalyst materials is being tested a in potentiostatic environment, the system can be thought of as a black box with a sinusoidal wave of potential entering the system, and a sinusoidal current wave with the same angular frequency, but different amplitude and phase is produced. The analysis of the variation between the two amplitudes and phases is the basis of EIS. A difference in the amplitude of two sine waves is simply the ratio of the heights of the input and output peaks and is often referred to as the magnitude of the impedance (Z_o). The difference in the phase of the waves is a shift of one peak along the x axis with respect to the other wave. This is called the phase shift, or phase angle, and is represented by the Greek letter phi (ϕ). A figure showing two waves with different phase angles is shown in Figure 13.
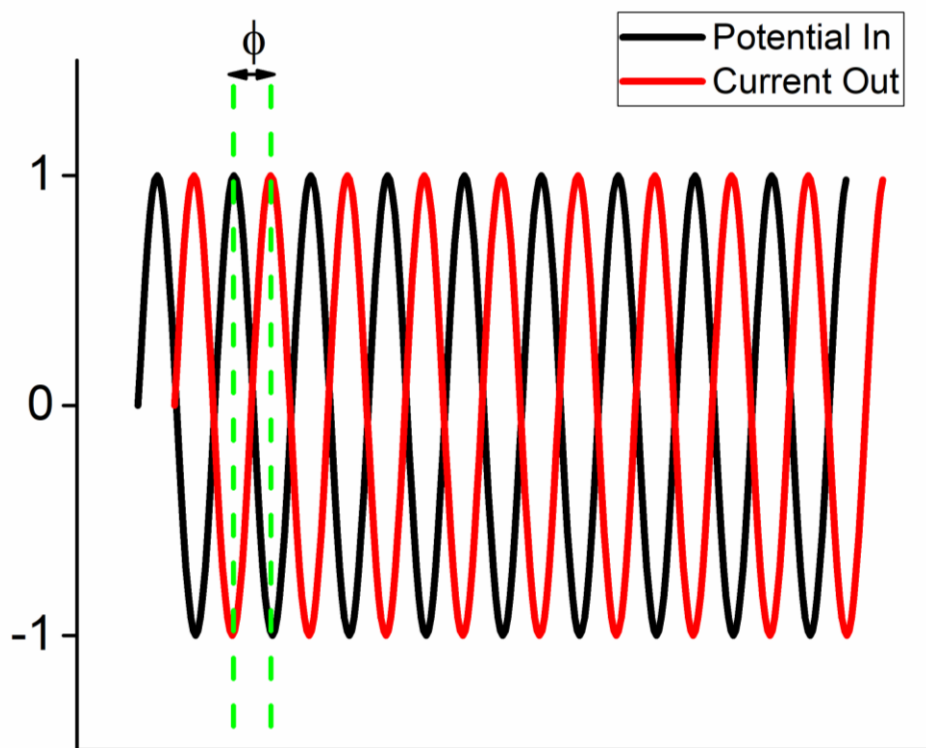
Figure 13 – Phase angle(ϕ) between two sinusoidal waves. Black represents incoming potential to system and red represents resulting current output from the system. Green dashed lines are for visualisation purposes.

However, there is a lot of information stored in the waves of the input and output and plotting the data in an accessible way requires some data processing.

3.7.1 Nyquist Plots

As mentioned, plotting the data gathered from electrochemical impedance spectroscopy (EIS) can be quite challenging due to the amount of data contained in the results, but for the EIS analysis of oxygen evolution electrocatalysts, the Nyquist plot is arguably the most useful representation of the data. In order to plot a Nyquist plot, the input and output sinusoidal wave data must be processed.

The incident potential sinusoidal wave can be expressed as a function of time, shown in equation 25.

$$E_t = E_o \sin(\omega t) \tag{25}$$

Where E_t is the potential at time t, E_o is the amplitude of the signal, and ω is the angular frequency. This is similar to the output current sinusoidal wave (equation 26).

$$I_t = I_o \sin(\omega t + \Phi) \tag{26}$$

Where I_t is the current at time t, I_o is the amplitude of the signal, ω is the angular frequency, and ϕ is the phase shift. The impedance of the circuit (Z) as a function of time t is calculated by the ratio of potential to current at time t, using the same principles as found in Ohm's law for calculating resistance (equation 27).

$$Z = \frac{E_t}{I_t} = \frac{E_o \sin(\omega t)}{I_o \sin(\omega t + \Phi)} = Z_o = \frac{\sin(\omega t)}{\sin(\omega t + \Phi)} \tag{27}$$

It can be seen from equation 27 that the impedance is a function of magnitude (the ratio between the amplitude of the two waves, stylised as Z_o) and the phase shift (ϕ). This information can be represented in a Nyquist plot using Euler's formula (equation 28), which when applied using the phase angle (ϕ), gives the general formula:

$$e^{j\Phi} = \cos(\Phi) + j sin(\Phi) \tag{28}$$

Where ϕ is the phase angle and j is the imaginary component.

By utilising Euler's formula, the impedance of the system can be expressed by a real and complex number, which can be plotted against each other. This plot is known as a Nyquist plot

and is a good way of representing all the data gained from EIS on one axis. Taking into consideration equation 28, the potential can be described by equation 29.

$$E_t = E_o exp^{(j\omega t)} \tag{29}$$

Whilst the current response is expressed in equation 30.

$$I_t = I_o exp^{(j\omega t - \Phi)} \tag{30}$$

Combining equations 29 and 30 allows the impedance (Z) as a function of angular frequency (ω) to be expressed as a complex function, and as previously mentioned, the real (Z') and the imaginary (-Z'') part of equation 31 can be plotted against each other to give a Nyquist plot, an example of which is shown in Figure 14.

$$Z(\omega) = \frac{E}{I} = Z_o = exp^{(j\Phi)} = Z_o(cos\Phi + jsin\Phi) \tag{31}$$
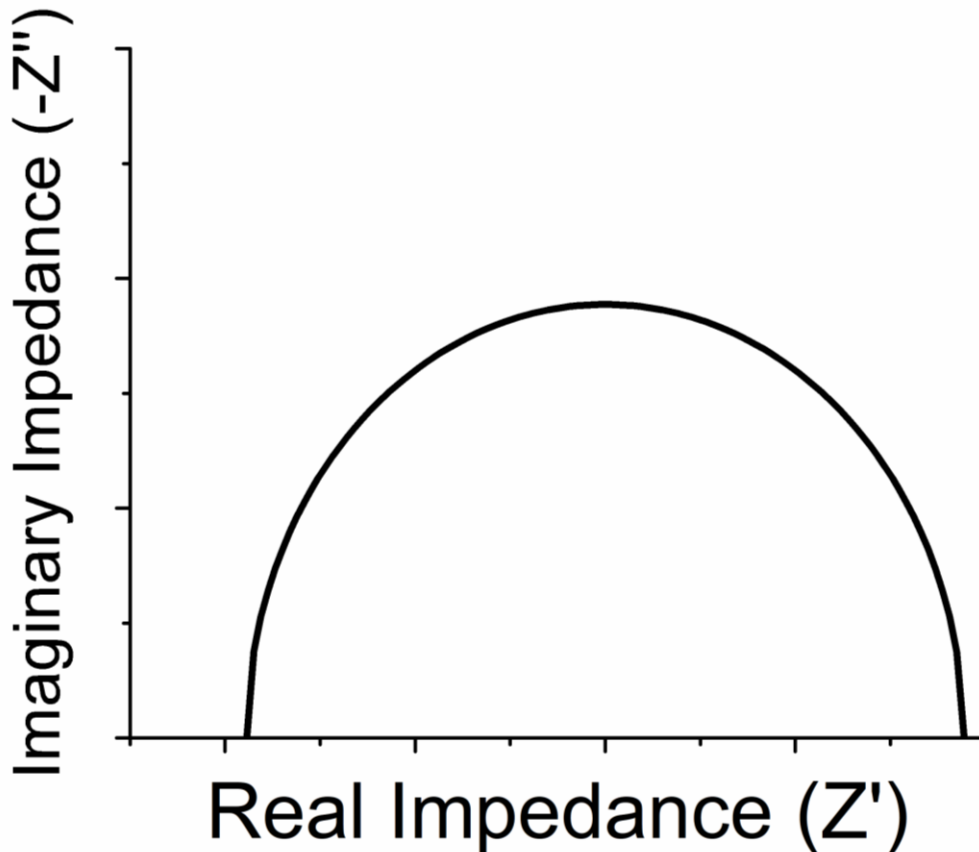
Figure 14 – Example of a Nyquist plot showing perfect semi-circle

3.7.2 Data Fitting

As previously discussed, EIS plots such as the Nyquist plot contain a large amount of information about the impedance of the catalytic material. The most common method for extracting system information from these plots is to fit the data to an equivalent electrical circuit (EEC) model. The equivalent electrical circuit must be based on known electrochemical elements as the system, for instance including a resistor component to account for the solution resistance of the electrolyte. The data model utilised in the fitting of the EIS data for perovskite oxides is a series of three elements, a resistor element to account for solution resistance, and two constant phase element (CPE) which are in parallel to two resistor elements accounting for the high and low frequency regions respectively. A model outlining the electrical equivalent circuit is shown in Figure 15.
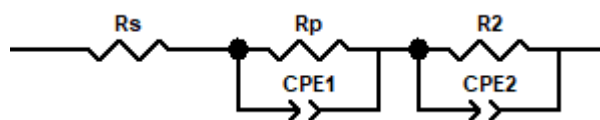
Figure 15 – Equivalent electrical circuit model used for modelling Nyquist plots of alkaline oxygen evolution electrocatalysis facilitated by perovskite oxide catalysts.

To understand the choice of equivalent electrical circuit used for the analysis of EIS data gathered in this thesis, it is important to explain the purpose of using three components in the EEC. This initially appears counter intuitive as there only appears to be one semi-circle present in the Nyquist plots for the OER, which would indicate that a two component EEC would be sufficient (the Rs for solution resistance, and one Resistor/CPE component representing the interaction between the species and the catalyst). However, during electrochemical impedance spectroscopy (EIS) points are taken at a range of frequencies going from high to low with respect to the real (Z') impendence (Figure 14). This varied frequency range translates to different electrocatalytic reactions and environments best demonstrated by the change in relaxation time, which is the time taken for an equilibrium to reach a new equilibrium which is brought about from external perturbations, often denoted as τ. Frequency and τ are inversely proportional, so high frequency environments have low relaxation time and vice-versa. This application of pure electrophysics has been studied with respects to oxygen electrocatalytic reactions to better understand the kinetics

of the reaction, and this high and low frequency environment is the reasoning behind the three individual components in the equivalent electrical circuit model shown in Figure 15.

As discussed, the first component (Rs) is related to the resistance arising from the electrolyte solution. The next combination of Rp and CPE1 models the high frequency (low τ) domain, which has been attributed to the interaction between the oxygen species and the pores/grain boundary of the catalyst, as well as any active dielectric effects present at the specific voltage. The final component consists of R2 and CPE2 which accounts for the low frequency (high τ) domain, which relate to Faradaic processes which are generally interfacial charge transfer reactions, which consist of the electron transfer between differing energy levels at both material-material and material-electrolyte interfaces.[119-121]

This is obviously a somewhat simplified view of these electrochemical phenomena, but this model is fit for the purpose of comparing the results of a material series and gathering an estimate of the electrical behaviour of catalytic materials. The next section will discuss what is meant by a capacitor and show how electrochemical parameters such as capacitance are calculated.

Transition metal-based perovskite oxides will act as a capacitor during the oxygen evolution reaction, due to the formation of what is known as double layer capacitance. The double layer capacitance forms at the surface of the electrocatalyst as ions from the electrolyte solution adsorb onto the material surface. This, in turn, causes the charged electrode to be separated from the charged ions by a very small (order of Angstroms) insulating layer known as the dielectric. The capacitance can be estimated through equation 32.

$$C = \frac{\varepsilon_o \varepsilon_r A}{d} \tag{32}$$

Where C is the capacitance, ε_o is the electric constant, ε_r is the dielectric constant, A is the surface of the electrode, and d is the space between the electrode and the ions. However, capacitor materials often do not act like a 'true' capacitor during EIS, and they are often defined by the constant phase element (CPE). The impedance of a constant phase element (Z_{CPE}) is calculated through equation 33.

$$Z_{CPE} = \frac{1}{(j\omega)^\alpha Y_o} \tag{33}$$

Where ω is the angular frequency in radians per second, Y_o is the material capacitance in Farads, and α is an exponent between 0 and 1 where 1 is a true capacitor and 0 is a resistor. The exponent function can be visualised in the Nyquist plot by how perfect the semi-circle is, with 1 being a perfect semi-circle.[122]

3.8 Cyclic Voltammetry (CV)

Cyclic voltammetry is a powerful technique for electrochemical characterisation of electron transfer initiated catalytic reactions. The core concept in cyclic voltammetry of oxygen evolution electrocatalysts is applying a known potential at a defined scan rate and measuring the current output of the system. The cyclic aspect of the name refers to the idea that multiple scans can be performed, cycling between set potentials, and measuring current output over time.

As the oxygen evolution reaction (OER) is an oxidation reaction, the performance of the catalyst is tested in potentiostatic mode, scanning from low to high positive potential values. As previously discussed, the thermodynamic minimum for the water splitting reaction to begin is 1.23 V and any potential above this value is coined as the overpotential (η). This is an important consideration, as the potential where the reaction begins to be facilitated is measured (normally defined by the potential needed to produce a small amount of current) and termed as the onset potential. The other parameters of note when analysing a cyclic voltammogram is the height of the peak (indicating maximum catalytic activity), and the gradient of the increasing in current over a set current rage (normally one order of magnitude) known as the Tafel slope. However, this potential is a function of the reference electrode used, and as measured is only comparable to systems utilising the exact same environments. Obviously, this produces a problem when attempting to compare catalyst performance across various systems. This requires the need for the potential to be normalised to a universal scale known as the reversible hydrogen electrode, and this normalisation is performed using the Nernst equation.

3.8.1 The Nernst Equation

The Nernst equation is the determination of the reduction potential of a reaction using chemical and thermodynamic properties such as temperature, the number of electrons exchanged, the activities of the reacting species, and the standard electrode potential.[123] The

reason that the reversible hydrogen electrode is used is because it allows comparison to systems where no salt bridge in present, such as is the case during the OER characterisation.

The reaction quotient (Q_r) is the ratio of the activity of the oxidised and reduced species. For any dissolved chemical species, the activity ($a_{Species}$) is essentially the concentration of the species in the dissolution media, provided the concentration or the activity coefficients of the species are not too high. At chemical equilibrium, the reaction quotient is equal to the equilibrium constant (K) for the half cell reaction, as shown in equation 34.

$$Q_r = \frac{a_{Red}}{a_{Ox}} = \frac{[Red]}{[Ox]} = K \tag{34}$$

Where square brackets indicate the concentration of the species.

The reaction quotient (Q_r) is also related to the change in the Gibb's free energy (ΔG) through equation 35, and the cell potential (E), defined as the decrease in Gibb's free energy per coulomb of charge transfer is related to the Gibb's free energy through equation 36.

$$\Delta G = \Delta G^{\ominus} + RT \ln Q_r \tag{35}$$

$$\Delta G = -zFE \tag{36}$$

Where $\Delta G^{\ominus}$ is the change in free energy under standard conditions, R is the ideal gas constant (8.314 J mol^{-1} K^{-1}), T is the temperature in kelvin, z is the number of electrons transferred in the half-cell reaction, and F is the Faraday constant (96485.332 C mol^{-1}). The combination of these elements with the standard half-cell reduction potential ($E_{Red}^{\ominus}$ gathered from data tables) gives the Nernst equation for calculating half-cell reaction potential (E_{Red}) (equation 37).

$$E_{Red} = E_{Red}^{\ominus} - \frac{RT}{zF} \ln Q_r = E_{Red}^{\ominus} - \frac{RT}{zF} \ln \frac{[Red]}{[Ox]} \tag{37}$$

As a lot of the elements utilised in the Nernst equation are known values, the Nernst equation for certain electrochemical reactions can be simplified. The properties of the concentrations of reactant and oxidant species can also be represented as a function of system's pH, which is particularly useful as this value is easily calculated from the electrolyte solution. For

a half-cell reduction reaction with the form of equation 38 and factoring in the known values of the constants, the Nernst equation with respect to pH can be written as equation 39 and 40.

$$aA + bB + ze^- \rightleftharpoons cC + dD \tag{38}$$

$$E_{Red} = E_{Red}^{\ominus} - \frac{0.05916}{z} \log\left(\frac{[C]^c [D]^d}{[A]^a [B]^b}\right) \tag{39}$$

$$E_{Red} = E_{Red}^{\ominus} - 0.05916\, pH \tag{40}$$

3.8.2 Ink preparation

Electrochemical data for all perovskite oxide series investigated in this thesis were measured using a potentiostat attached to a three-electrode cell. In order to transfer the perovskite material onto the gold working electrode, the material was first dispersed in an ink before drop-casting directly onto the electrode and allowed to dry. The ink preparation involved mixing together 2 mg of perovskite catalyst, 0.4 ml deionised H_2O, 0.1 ml propan-2-ol, and 60 µl of Nafion 117 binding solution (5% w/v). Homogenous mixing was assured by ultrasonicating the ink for at least 20 minutes. 3 µl of the ink was then drop cast onto a 3 mm diameter gold electrode (99.95% purity, Alvatek), which acted as the working electrode. This ensured that ~10.7 µg of catalyst was loaded onto the electrode which has an area of 0.07 cm^2, giving a catalyst material coverage of approximately 153 µg/cm^{-2}. Cyclic voltammetry (CV) and electrochemical impedance spectroscopy (EIS) were carried out in a glass cell, using the catalyst coated gold electrode as a working electrode, alongside a Ag/AgCl leakless electrode and platinum mesh as reference and counter electrodes, respectively. A solution of nitrogen saturated 0.1 M KOH (Alfa Aesar, 99.98%) in deionised water was used as the electrolyte.[124-126] The Ag/AgCl reference electrode was calibrated against the reversible hydrogen electrode (RHE) in the same electrolyte solution, giving a conversion values of $E_{RHE} = E_{Ag/AgCl} + 0.98$ V. Potential and currents were applied and measured respectively using a Gamry Interface 5000E potentiostat. Cyclic voltammetry experiments were carried out in a range of 1.30 – 1.80 V_{RHE}, using a scan rate of 5 mV s^{-1}. 3 cycles were measured after activating the material by running chronoamperometry at 1.70 V_{RHE} for 30 minutes. To account for resistances arising from the electrolyte solution, and internal connections, ohmic

drop (*iR*) compensation was applied to the electrochemical data post testing using resistance data gathered from EIS measurements. All current densities were normalised through the area of the electrode. EIS scans were recorded from 10^5 to 10^{-1} Hz at 1.70 V_{RHE}.

Chapter 4. Oxygen evolution reaction facilitated by Sr dopant in $Pr_{1-x}Sr_xFeO_{3-\delta}$ Perovskite Oxides

4.1 Introduction

This chapter focuses on the aliovalent substitution of Pr^{3+} ion for Sr^{2+} ions in the single perovskite oxide lattice $Pr_{1-x}Sr_xFeO_{3-\delta}$. It is hypothesised that increased strontium content in the perovskite lattice will lead to the formation of oxygen vacancies, which will in turn increase the activity of the oxygen evolution reaction due to increased exposure of the B-site catalyst surface, and a change in the oxidation state of the B-site iron centre promoting faster electron transfer between the catalyst surface and the adsorbed oxygen species.

The information in this chapter has been published in the Royal Society of Chemistry journal Sustainable Energy & Fuels, adding to the proof of novelty of the work carried out during this PhD.[127]

As discussed in the broad introduction to this thesis, water is a highly lucrative green energy source due to the relative abundance and green properties. Specifically, the use of alkaline electrolyser systems to liberate both hydrogen at the cathode (HER) and oxygen at the anode (OER) using water-based solutions as a fuel source is the overriding driving factor for carrying out the work displayed in this research. As mentioned in chapter 2,

the splitting reaction is rate limited by the kinetically sluggish nature of the oxygen evolution reaction (OER).[41, 128, 129] This sluggishness has led to electrolyser energy efficiency rates of as low as 53%.[33, 86-88] Hence, one of the keys to practical hydrogen production lies in overcoming the sluggishness of the OER.

Current state-of-the-art catalysts employed in the electrochemical splitting of water are the noble metal oxides IrO_2 and RuO_2 for the anodic half-cell reaction (equation 1), for the OER in alkaline solutions.[33, 41] These materials are some of the highest performing anodes, requiring overpotentials of around 470 mV to achieve a current density of 10 mA cm^{-2} in 0.1 M KOH electrolyte.[33-35] These materials however, are in low abundance, demonstrate poor ionic conductivity of oxygen species leading to high internal resistance manifesting as a limitation to the reaction rate, and utilise high cost materials. It is for this reason that there is a drive to replace these materials with high performing and more economically sustainably materials.

Although perovskite oxides were discussed in-depth in the previous chapter, it is useful to have a quick overview of the materials and their OER catalytic properties before discussing the specifics of the $Pr_{1-x}Sr_xFeO_3$ (PSFO) perovskite oxide material series. Perovskite oxides with the formula $ABO_{3-\delta}$ (A = rare earth metal and B = transition metal), synthesised using various routes,[130-134] have been well researched as potential catalysts for the oxygen evolution reaction (equation 1, below) due to their relatively low cost, high mixed ion-electron conductivity and high surface oxygen exchange coefficient.[135, 136] The effectiveness of perovskite oxides has been discussed in literature to be due to the binding strength of the oxygen intermediate species and the transition metal catalyst surface.[39, 41, 137, 138] As discussed in chapter 2, this binding strength of the various 4 electron oxidation process per mole of oxygen at the catalyst surface can be represented as a volcano type relationship between oxygen-bonding strength and catalytic activity.[39] Suntivich *et al.* expanded on this theory, discovering an activity descriptor for catalytic activity relating to the filling of the transition metal higher energy d shell e_g σ* antibonding orbital, with and e_g filling of single unit occupancy giving the highest oxygen species to transition metal catalyst interaction in octahedral complexes.[41, 53]

$$4OH^- \rightarrow O_2 + 2H_2O + 4e^- \tag{1}$$

This understanding of the relationship between d shell e_g σ* antibonding orbital filling altering the interactions with 2p π bonding orbital has led to developments of first row transition metal based perovskite oxide catalysts. Previously given examples of these are materials such as $Ba_{0.5}Sr_{0.5}Co_{0.8}Fe_{0.2}O_{3-\delta}$,[54-56] $LaNiO_{3-\delta}$,[57-59] and $LaFeO_{3-\delta}$[60] have successfully been demonstrated to be capable electrolyser anodes. Perovskite oxide materials have even been shown to have a comparable OER performance with IrO_2 catalysts.[139-141]

As discussed earlier in the thesis, perovskite oxides offer considerable control over their crystal structure with relatively small changes to the synthesis process. Specifically, the induction of a charge imbalance throughout the material through A site substitution is an important wet chemical technique in order to introduce oxygen vacancies into the crystal lattice, whilst still retaining the lattice configuration. This chapter shows the effectiveness of this technique viastrontium doped praseodymium ferrites (PSFO, $Pr_{1-x}Sr_xFeO_{3-\delta}$, x = 0, 0.1, 0.2, 0.3, 0.4, and 0.5). The increased concentration of divalent strontium (x) leads to increased oxygen vacancy

concentration (δ).[69] The proposed mechanism for oxygen vacancy (V) manufacture arising from substituting RE^{3+} with AE^{2+} denoted by Kröger-Vink notation is shown in equation 2.
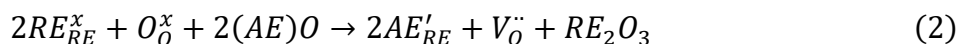
$$2RE_{RE}^{x} + O_{O}^{x} + 2(AE)O \rightarrow 2AE_{RE}' + V_{O}^{\cdot\cdot} + RE_2O_3 \tag{2}$$

Where x, ' and • represents neutral, single negative and single positive charge respectively. The presence of a vacancy in the perovskite lattice is thought to increase the availability of the transition metal catalytic sites at the triple phase boundary, leading to increased OER performance. [70, 71]

Electrolyte selection is important in electrolyser systems, especially when those systems are scaled up from 3-electrode cell testing into a full cell operation. In order to lessen high overpotentials due to the electrolyte, the water splitting reaction is best carried out under strongly acidic or alkaline conditions due to the lower solution resistance provided via the higher availability of ions contained in these solutions.[142] In order to avoid pH gradients from forming due to the high pH, the electrodes are separated by an ion conducting membrane in electrolyser setups.[143] In acidic media, transition metal oxides are associated with energy loss due to corrosion and high overpotentials at the anode.[39, 92, 144-146] Therefore, in order to extend the lifetime of the catalyst and to reduce overpotentials, alkaline environments are preferential when utilising transition metal based catalysts, which will allow for a replacement of noble metal based systems, increasing economic and environmental viability.

In this chapter the effects of different doping levels of strontium into praseodymium ferrite oxide perovskite structures is investigated with respect to the crystal structure, surface electronic states and the electrochemical performance, specifically of the oxygen evolution reaction.

4.2 Characterisation Methods

4.2.1 Iodometric Titration

The oxygen content of the perovskite oxides was calculated from the oxidation state of iron, which was determined by iodometric titration. ~20 mg of perovskite powder was dissolved in 20 ml of hydrochloric acid (12 M) by continuous stirring in a nitrogen gas flushed flask. An excess of 0.1 M KI was added once the powder had fully dissolved. 0.005 M Na$_2$S$_2$O$_3$ solution was

used to titrate against the iodine generated. A 1% starch solution, as an indicator, was added near the end of titration. The oxygen content of the perovskite oxides was calculated from the oxidation state of iron, which was determined by iodometric titration. ~20 mg of perovskite powder was dissolved in 20 ml of hydrochloric acid (12 M) by continuous stirring in a nitrogen gas flushed flask. An excess of 0.1 M KI was added once the powder had fully dissolved. 0.005 M $Na_2S_2O_3$ solution was used to titrate against the iodine generated. A 1% starch solution, as an indicator, was added near the end of titration.

Although iodometric titration involves the titration of I_3^- against $S_2O_3^{2-}$, in order to allow the B site transition metal to be reduced it must be in aqueous solution. To achieve this, perovskite powder is first dissolved in concentrated hydrochloric acid (HCl ~37 wt%). In a material containing only iron cations as the B site transition metal, no issue is caused by this as the reaction between iron (III) ions and chloride ions is thermodynamically unfavourable (equations 3 – 6), so the titration reaction can occur in solution.

$Overall$: $\quad\quad\quad\quad\quad\quad\quad\quad 2Fe^{3+} + 2Cl^- \leftrightarrow 2Fe^{2+} + Cl_2 \quad\quad\quad\quad\quad\quad\quad\quad\quad$ (3)

$Oxidation$: $\quad\quad\quad\quad\quad\quad\quad 2Cl^- \rightarrow Cl_2 + 2e^- \quad\quad\quad\quad E^{\circ}_{Ox} = -1.36\ V \quad$ (4)

$Reduction$: $\quad\quad\quad\quad\quad 2Fe^{3+} + 2e^- \rightarrow 2Fe^{2+} \quad\quad\quad\quad E^{\circ}_{Red} = +0.77\ V \quad$ (5)

$Total$: $\quad\quad\quad\quad\quad\quad\quad E^{\circ}_{Total} = E^{\circ}_{Ox} + E^{\circ}_{Red} \quad\quad\quad\quad E^{\circ}_{Total} = -0.59\ V \quad$ (6)
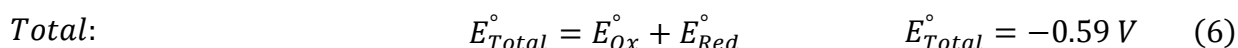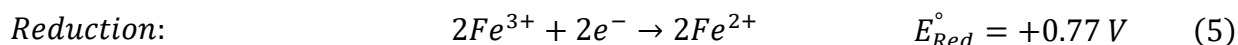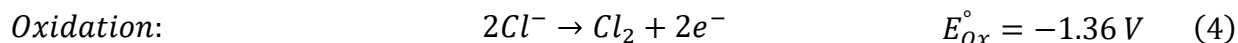
However, when a material which includes cobalt (III) ions is dissolved in concentrated hydrochloric acid, such as those discussed in the later chapters of this thesis, a stoichiometric amount of chlorine gas (Cl_2) is formed. For every 1 mole of Co^{3+} present, ½ moles of Cl_2 is produced (equations 7 – 10). As this gas is produced in a molar ratio to the metal ions, it must be accounted for in the titration, but using a simple gas flow into a bubble trap will remove this gas from the reaction vessel, providing inaccurate results.

$$Overall: \quad 2Co^{3+} + 2Cl^- \leftrightarrow 2Co^{2+} + Cl_2 \tag{7}$$

$$Oxidation: \quad 2Cl^- \rightarrow Cl_2 + 2e^- \qquad E^\circ_{Ox} = -1.36\,V \tag{8}$$

$$Reduction: \quad 2Co^{3+} + 2e^- \rightarrow 2Co^{2+} \qquad E^\circ_{Red} = +1.82\,V \tag{9}$$

$$Total: \quad E^\circ_{Total} = E^\circ_{Ox} + E^\circ_{Red} \qquad E^\circ_{Total} = +0.46\,V \tag{10}$$
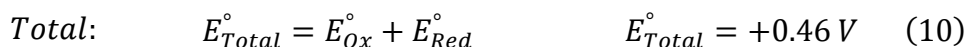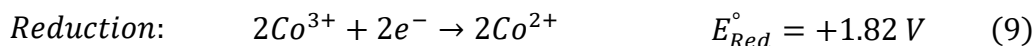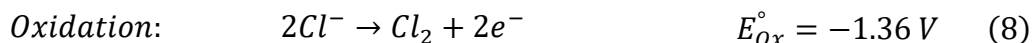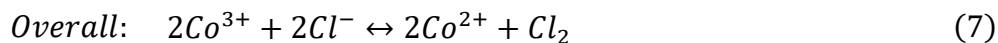
4.2.2 Full Cell Electrolyser Testing

The performance of the material as a catalyst at electrolyser anodes was tested using a 300 μm thick titanium fibre felt gas diffusion layer (GDL, Bekaert S.A. Fibre Technologies) with a 78% porosity using 20 μm thick titanium fibres used as a support for the PSFO material. The mesh was cut into an area of 2 cm². The anode was prepared by spraying the catalyst material directly onto the titanium mesh. The spray consisted of 10 wt.% polystyrene-b-poly (ethylene/butylene)-b-polystyrene base ionomer, made with polymer synthesis as outlined by Gupta et al.,[147] with 2 mg cm^{-2} loading of the PSFO perovskite samples, with a small amount of 5 wt.% polytetrafluoroethylene (PTFE) binder.

The cathode for the hydrogen evolution reaction (HER) was constructed using a non-wet proofed carbon GDL with microporous layer (MPL, Freudenberg), cut into a 13 mm diameter circle. For the HER catalyst, 0.4 mg cm^{-2} 20 wt.% Pt on carbon was used. The catalyst ink contained 20 wt.% Pt on carbon, 28 wt.% ionomer, a small amount of 5 wt.% PTFE binder, and propan-2-ol. This was sprayed directly onto the carbon GDL/MPL paper.

The radiation grafted anion exchange membrane (AEM) was synthesised also according to Gupta et al.,[147] using a low-density polyethene (LDPE) with vinylbenzyl chloride (VBC) as the graft monomer. 0.1 M NaOH was used as the electrolyte. EIS and CV scans were measured at 20 °C, 40 °C, 60 °C, and 80 °C.

X-ray photoelectron spectroscopy (XPS) Analysis was performed using a Kratos Axis SUPRA XPS fitted with a monochromated Al Kα X-ray source (1486.7 eV), a spherical sector analyser and 3 multichannel resistive plate, 128 channel delay line detectors. Ultraviolet photoelectron spectroscopy (UPS) measurements were performed using a He(I) lamp (21.22 eV) and an emission current of 25 mA. All spectra were recorded at 150 W and a spot size of 700 μm x 300 μm. Survey scans were recorded at a pass energy of 160 eV, and high-resolution scans recorded at a pass

energy of 20 eV. UPS scans were recorded with a pass energy of 5 eV. Electronic charge neutralization was achieved using an electron flood gun. The parameters used for the filament current, charge balance, and filament bias were 0.27 A, 3.3 V, and 3.8 V respectively. All sample data were recorded at a pressure below 10^{-9} Torr and a room temperature of 294 K. Data was analysed using CasaXPS v2.3.19PR1.0. Peaks were fit with a Shirley background prior to component analysis. Lineshapes of LA(1.53,243) were used to fit components. Charge calibration was achieved using adventitious carbon at 284.8 eV.

4.3 3. Results and Discussion

4.3.1 3.1. Crystal Structure
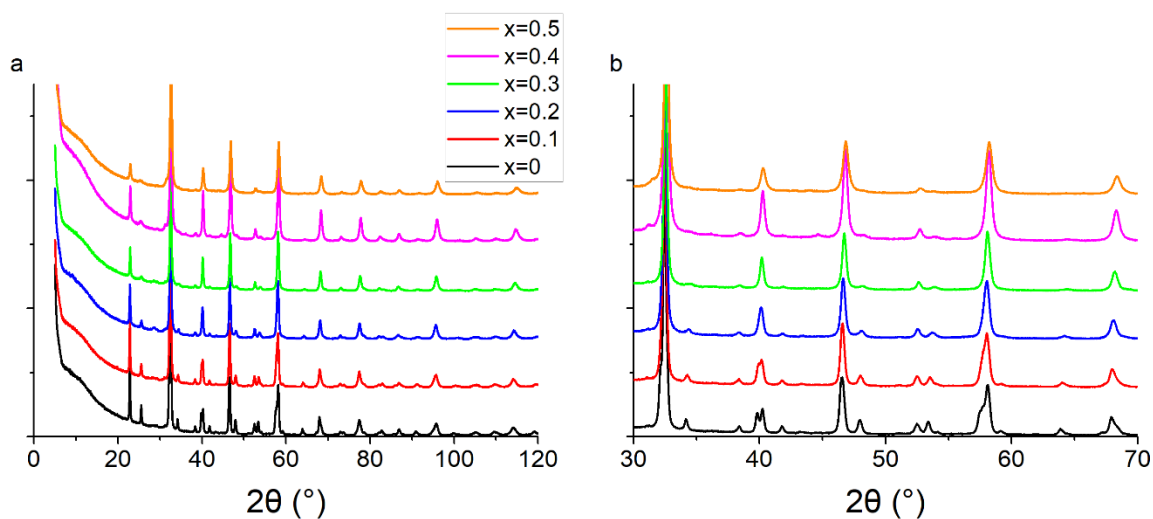
Figure 16 - a) Powder XRD Patterns for the as-synthesised $Pr_{1-x}Sr_xFeO_{3-\delta}$ perovskite oxides. b) As the concentration of strontium (x) increases, there is a phase transformation towards a high symmetry pseudo-cubic structure, as seen by the reduction in the number of visible Bragg reflections around for example $2\theta = 40.2, 47.9$ and 53.4 °.

Powder X-Ray diffraction patterns for all PSFO samples indicate pure perovskite phase with minimal secondary impurity phases within the detection limit of the XRD instrument (Figure 16). The x = 0.4 and x = 0.5 material have a small amount (< 3 wt.%) of $Pr_2FeO_{4+\delta}$ Ruddlesden-Popper phase present. The Rietveld fits of the XRD patterns are collated in Figures 25 – 30. As the concentration of the divalent strontium species (Sr^{2+}) increases, the peaks shift towards a higher 2θ value which results in the contraction of the perovskite lattice parameters (Figures 17a and b) but the overall crystal structure retains the orthorhombic *Pbnm* space group, as is consistent with literature studies of similar materials.[148] As highlighted in Figure 16b, the number of Bragg reflections decreases as x increases. It is clearly observed at $2\theta = 40.2, 47.9$ and 53.4 ° where the

peak splits are less apparent. This indicates the reduction of the orthorhombic distortion, leading to a higher degree of crystal symmetry indicated by the ratio of b/a lattice parameters approaching unity with increased Sr^{2+} (Figure 17c).[69, 149, 150] This reduction of orthorhombic distortion leading closer to an ideal cubic perovskite increases the electrical conductivity of the material.[151] This is explained by a wider charge carrier bandwidth and overlap between the Fe 3d and O 2p orbitals, which is due to the changes in buckling angle of the Fe-O-Fe bonds, and the bond lengths of the Fe-O environment.[152, 153]
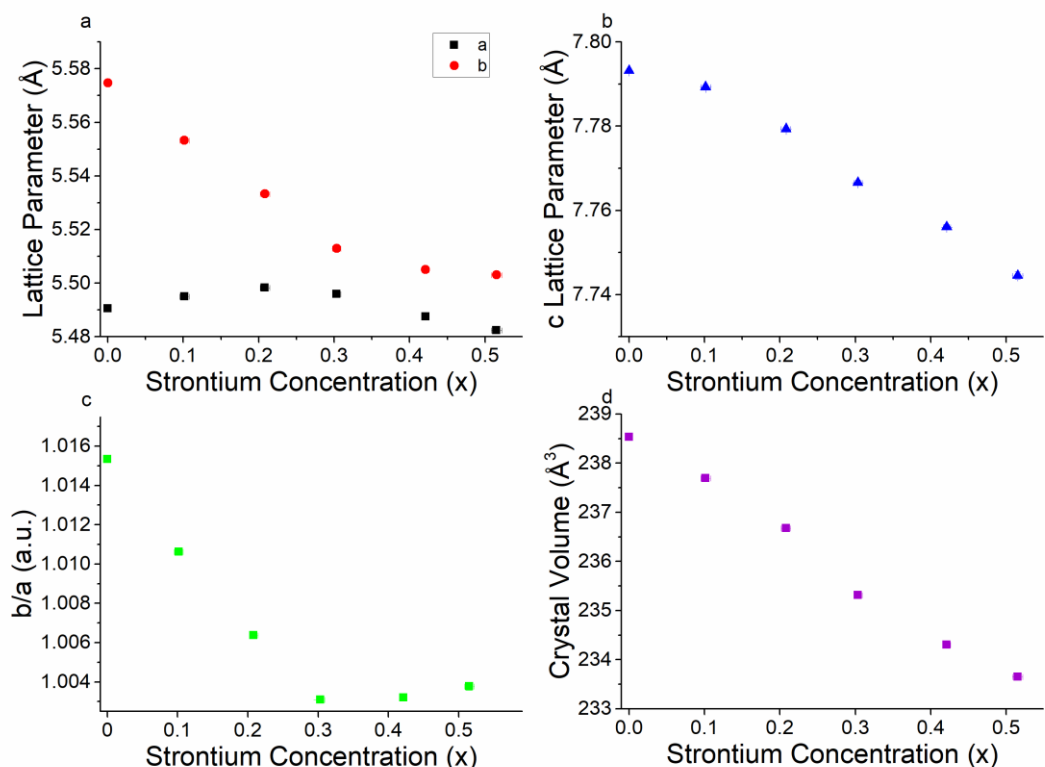
Figure 17 - a) Plots showing the variation of a and b lattice parameters. b) c lattice parameter. c) b/a trend indicating a shift towards a pseudo cubic structure, close to that of an ideal perovskite, as x increases. d) The near linear decreasing relationship of the unit cell volume with increased Sr^{2+} concentration.

The contraction of lattice parameters and crystal volume as strontium doping increases is shown in Figure 17. Overall, the *a* lattice parameter stayed at 5.48 to 5.49 Å, whereas the *b* and *c* lattice parameter decreased in line with increasing Sr^{2+} content. The overall crystal volume of the perovskite decreased with increased addition of Sr^{2+}. Despite the larger ionic size of Sr^{2+} (1.31 Å, in 9-coordination)[154] occupying the Pr^{3+} site (1.179 Å), the decreasing trend of the unit cell volume can be explained by an increasing average oxidation state of Fe, obtained from the iodometric

titration, and as a result, a decrease in the coordination number of Fe-O, from 6 to 5, due to a higher oxygen vacancy content. This is consistent with a slight shift of X-ray photoelectron spectrum towards a lower binding energy of Fe 2p as x increases, which will be explained in the next section. Lattice parameters and crystal volume are shown in Table 4. The reduction of the crystal lattice volume as Sr^{2+} doping concentration increases is consistent with what has been observed in similar perovskite oxide materials.[155, 156]

Table 4 – Lattice parameters and crystal volume for different Sr^{2+} concentration in $Pr_{1-x}Sr_xFeO_{3-δ}$ perovskite oxides. All data acquired through Rietveld refinement method of powder XRD diffraction patterns.

Sr^{2+} Concentration (x)	a lattice parameter (Å)	b lattice parameter (Å)	c lattice parameter (Å)	Crystal Volume (Å³)
0	5.4905 (2)	5.5748 (2)	7.7932 (2)	238.54 (1)
0.101 (6)	5.4950 (2)	5.5533 (2)	7.7893 (3)	237.69 (2)
0.208 (6)	5.4983 (3)	5.5333 (3)	7.7793 (4)	236.68 (2)
0.303 (6)	5.4959 (4)	5.5130 (5)	7.7666 (6)	235.32 (3)
0.421 (5)	5.4875 (5)	5.5051 (3)	7.7561 (6)	234.30 (3)
0.515 (7)	5.4824 (6)	5.5031 (9)	7.7445 (9)	233.65 (5)

Bond valence sum (BVS) analysis[157] which gives an estimation of the bond strength in ionic compounds, was calculated taking into consideration the oxygen vacancy concentration determined by iodometric titration using equation 4.

$$s_i = \sum exp^{\frac{(R_0 - R)}{B}} \tag{4}$$

Where s_i is the bond valence sum, R_0 and B are previously determined parameters,[157] and R is the bond length.[158] For determining the BVS of the Fe cation, 1.76 Å and 0.35 were used for Ro and B respectively. The oxygen vacancy weighted bond valence sum of Fe cation, and Fe-O bond lengths for each material are listed in Table 5.

Table 5 – Bond lengths and Bond Valence Sum of Fe for different Sr^{2+} concentration in $Pr_{1-x}Sr_xFeO_{3-\delta}$ perovskite oxides.

Sr^{2+} Concentration (x)	Average Total Bond Length (Å)	Average Axial Bond Length (Å)	Average Equatorial Bond Length (Å)	Bond Valence Sum of Fe
0	2.010 (2)	2.012 (2)	2.009 (4)	2.99 (2)
0.101 (6)	2.002 (3)	1.996 (2)	2.005 (5)	2.99 (3)
0.208 (6)	1.989 (4)	1.972 (3)	1.999 (6)	3.11 (4)
0.303 (6)	1.977 (5)	1.971 (4)	1.979 (8)	3.15 (5)
0.421 (5)	1.966 (7)	1.958 (4)	1.970 (10)	3.19 (7)
0.515 (7)	1.962 (7)	1.976 (4)	1.955 (10)	3.19 (7)

Interestingly, Figures 18a and b indicate that for lower Sr^{2+} concentration (x = 0 – 0.2) it is the axial Fe-O bonds that appear to have a higher contribution to the reduction in the average overall bond length, whereas for Sr^{2+} concentrations of 0.3 – 0.5 the equatorial bond lengths have a greater contribution. This observation is worthy of note, but the reasoning behind this change is beyond the scope of this investigation. In line with what is hypothesised in equation 2, Figure 18d shows that as Sr^{2+} concentration increases, so too does the concentration of oxygen vacancies. The reduction of the oxygen stoichiometry (3-δ) whilst retaining the *Pbnm* space group was thought to lead to a higher active sites of the B site Fe catalyst surface throughout the crystal lattice to the oxygen species to be oxidised, leading to an increase in OER catalytic activity.
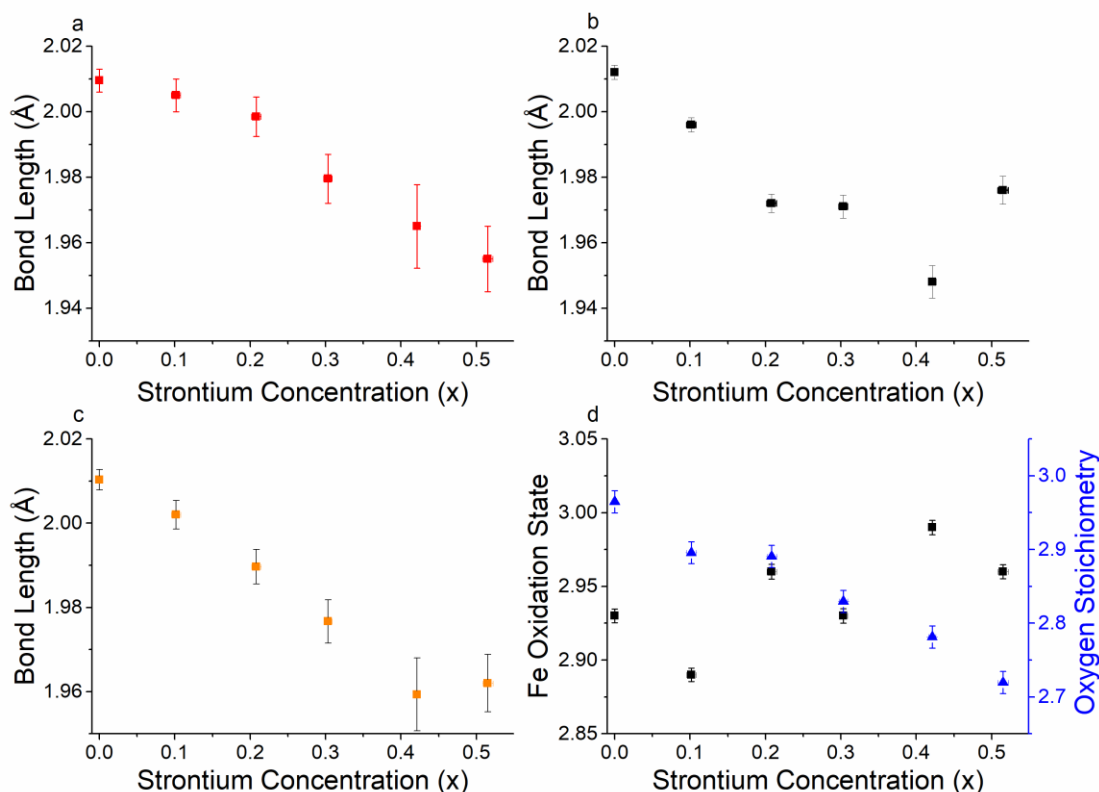
Figure 18 – a) Average Fe-O equatorial bond lengths. b) Average Fe-O axial bond lengths. c) Total average bond lengths of the Fe-O octahedra. d) Fe oxidation state and oxygen stoichiometry (3-δ) calculated from iodometric titration. All values are plotted as a function of Sr^{2+} concentration. Errors calculated by propagating estimated standard deviation (ESD) of each step, culminating in the error bars shown above.

The presence of Fe^{4+} was ruled out in this system as this was not observed in either the iodometric titration or the XPS measurements. The higher overall oxidation state will lead to a d shell degenerate e_g orbital filling closer to unity, which as previously discussed[41, 53] will lead to higher OER catalyst activity. This combined with the increased availability of the transition metal species through vacancies in the oxygen site were hypothesised to be the reason behind the increase in the OER electrocatalytic performance of the higher Sr^{2+} doped PSFO material. This increase in the oxidation state is in good agreement with recent literature regarding studies of the perovskite oxide $La_{1-x}Sr_xFeO_{3-\delta}$ for OER catalysis, where Fe oxidation states as high as 4+ have been observed in high Sr^{2+} doping concentrations through X-ray absorption spectroscopy of Fe $L_{2,3}$ edge.[159, 160] This increase of overall oxidation state will induce changes in the electronic properties of the material, with increasing oxidation state affecting the density of states (DOS) near the Fermi level, thus altering the binding strength between the Fe 3d and oxygen species 2p

orbitals which as previously discussed is in line with the activity descriptor set out by Suntivich *et al.*[124, 161]

4.3.2 3.2. Surface Electronic Structure and Chemistry
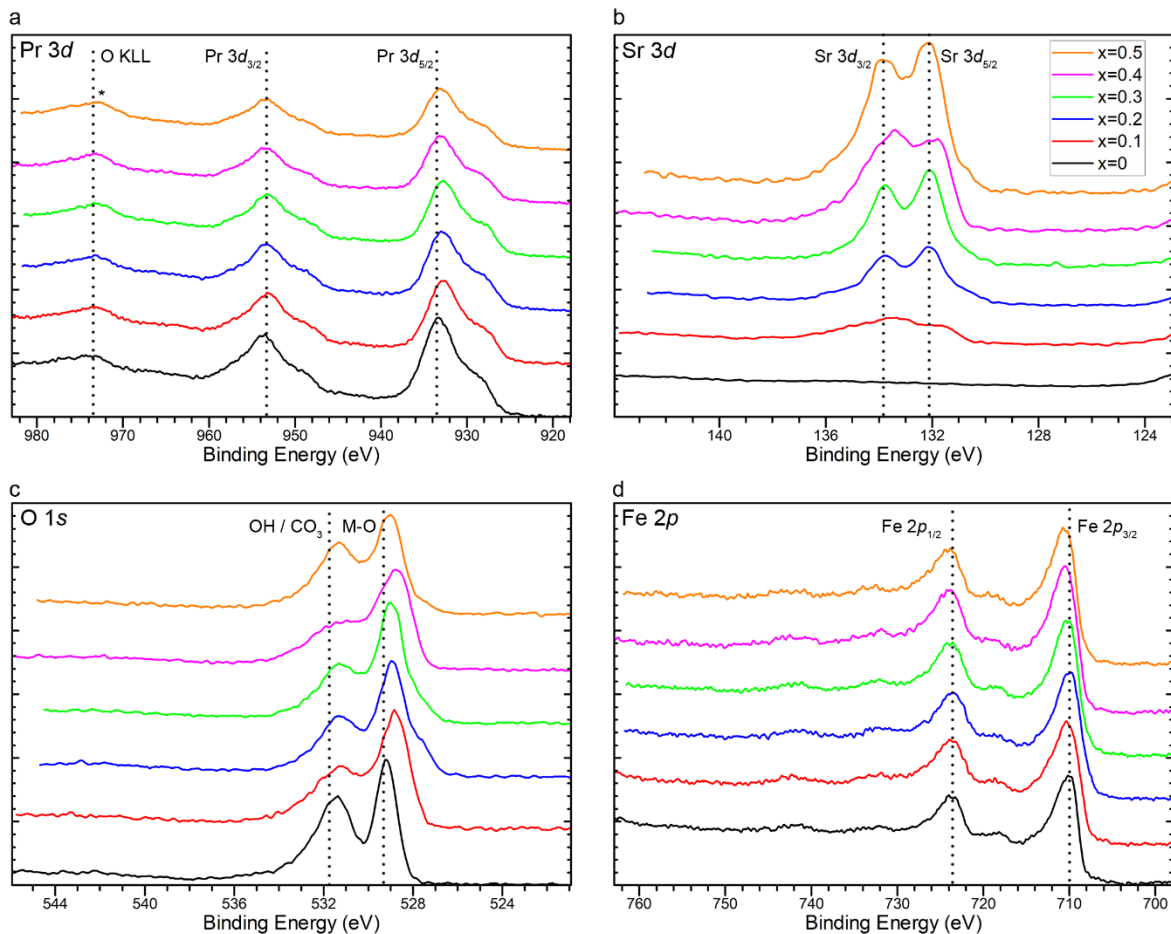
Figure 19 – X-ray photoelectron spectra of a) Pr 3d, b) Sr 3d, c) O 1s, and d) Fe 2p core orbitals of Pr$_{1-x}$Sr$_x$FeO$_{3-\delta}$ (x = 0, 0.1, 0.2, 0.3, 0.4, and 0.5).

The binding energies (BE) obtained from XPS were corrected by calibrating the scans so that the dominant low binding energy C 1s peak was at 284.8 eV. High resolution scans of Pr 3d in Figure 19a display a common lineshape characteristic of Pr^{3+}.[162] Figure 19a shows two distinct typical peaks at around 933 and 953 eV, which are attributed to Pr 3d$_{5/2}$ and Pr 3d$_{3/2}$ respectively.[163, 164] The difference of ~ 20 eV is consistent with literature values for the spin orbital splitting of the 3d$_{5/2}$ and 3d$_{3/2}$ praseodymium orbitals.[162, 165] Unfortunately, the determination between Pr 3+ and 4+ is challenging due to the complex nature of final state effects in such systems. For example, It has been reported[162, 165] that a satellite peak at 967 eV, arising from $3d4f^1$

71

final states, is exclusive of Pr^{4+} from studies of PrO_2, which is absent in the scans presented in Figure 19a. This could indicate that the praseodymium is present in a 3+ oxidation state as would be expected in $ABO_{3-\delta}$ perovskite oxides. However, there is overlap between this satellite peak and the oxygen O KLL Auger peak (~973 eV) which makes satellite peak determination difficult.[166] However, careful analysis of the Pr $3d_{5/2}$ lineshape and high energy final state effects affords an appropriate methodology for praseodymium oxidation state determination. Analysis of the $3d_{5/2}$ photoemission reveals the presence of one photoemission peak (*m*) and one shake-down satellite (*s*) at lower binding energy arising from well screened $4f^3$ final states. The ratio between these two peaks varies between Pr^{3+} and Pr^{4+}, with Pr_2O_3 reporting a higher ratio of *m:s* than PrO_2.[162] Deconvolution of our experimental data reports a constant *m:s* ratio of 3.05 ± 0.05 a.u. which is consistent with the theoretically determined ratio for Pr^{3+}.[167]

As the value for x increases, praseodymium is replaced with strontium. As expected, intensities of the peaks found in photoelectron scans of the Sr 3d core orbital increase with increasing values of x (Figure 19b). Peak models were fit using an Sr 3d doublet separation of 1.76 eV and defining two species, SrO at 132 eV and $SrCO_3$ at 133.8 eV (Figure 20).[168] It was determined that as the strontium content increased in the perovskite, the ratio between SrO and $SrCO_3$ also increased in favour of the oxide with the exception of x = 0.4, which reported an anomalous quantity of carbonate in relation to the rest of the series. It is of note that no carbonate species was detected within detection limits of the XRD scans. This is indicative that the carbonate species is located mainly at the surface of the catalyst which will play a critical role in blocking the surface catalytic reaction.[169] It is reasoned that this carbonate interference is the primary factor in explaining the anomalous electrochemical result seen for the x = 0.4 material, which is further elaborated in the next section. This performance was replicated in experimental repeats which suggests that the $Pr_{0.6}Sr_{0.4}FeO_{3-\delta}$ (x = 0.4) is prone to carbonate formation at this specific stoichiometry. The mechanism behind this specific carbonate formation is unclear, especially as this phenomenon is not seen in the surrounding stoichiometries (x = 0.3 and 0.5), which presents an opportunity for future study.
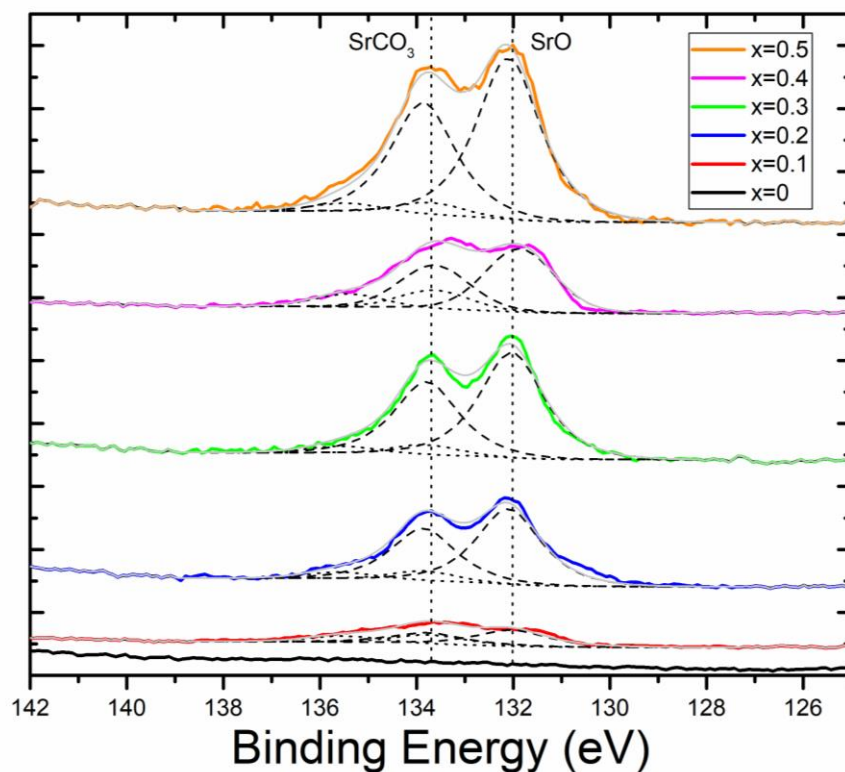
Figure 20 – Deconvoluted XPS scans of the Sr 3d core orbitals for PSFO perovskite oxide catalyst series where dashed and dotted lines show contributions from SrO and SrCO$_3$ respectively. Grey lines indicate peak fitting, with all samples showing good fit.

The presence of both oxide and carbonate environments is further confirmed from O 1s scans (Figure 19c), where there are two distinct peaks. Contributions from the lattice oxide at 528 eV are accompanied by contributions at a higher binding energy of around 531 eV, which is attributed to a mixed contribution of hydroxide and/or carbonate environments. Unfortunately, the binding energies of hydroxide and carbonate environments are very close together and therefore difficult to distinguish from each other from the O1s spectra.[170]

Figure 19d shows Fe 2p spectra across the series. The lineshape is characteristic of Fe(III) and was fit using a model developed via a combination of hematite (α-Fe$_2$O$_3$) reference material and the work of Grovesnor *et al*.[171] From these fits we can see an increase in binding energy of the principle photoemission rising from 709.7 eV (x = 0) to 710 eV (x = 0.5), indicating an increased localised charge (>δ^+) among the iron centres. The shift in the Fe 2p core orbital towards a higher binding energy with increased Sr^{2+} content is consistent with the iodometric titration results.

Ultraviolet photoelectron spectroscopy was used to determine the workfunction for each of the perovskite catalysts. The workfunction decreased as the concentration of Sr^{2+} cations increased on the A site of the perovskite lattice (Figures 31a and b). This decrease is related to the energy requirement to ionise the perovskite lattice, or to move electrons throughout the material. The increased electron movement within the crystal lattice will aid in the increased electrocatalytic performance, as discussed in the next section.

4.3.3 3.3. Electrochemistry

Cyclic voltammetry (CV) and electrochemical impedance spectroscopy (EIS) scan results are in line with what is suggested by the changes in crystal structure. Material with a higher Sr^{2+} concentration demonstrated considerably higher electrochemical performance than that of unaltered $PrFeO_{3-\delta}$. *iR* corrected CV plots for the PSFO series are presented in Figure 21. The undoped $PrFeO_{3-\delta}$ catalyst is still OER inactive up to 1.70 V against the reversible hydrogen electrode (RHE).

The oxygen vacancies in the Sr^{2+} doped PSFO catalysts play a crucial role in the increase in the oxygen evolution electrocatalytic activity. When a vacancy is introduced to the oxygen site of the crystal lattice, the coordination number of the Fe-O is reduced from 6 to 5. The 5 coordinated Fe-O unit will have a greater availability of the Fe 3d orbital with which the 2p orbital of the adsorbing OH^- species, creating an intermediate OH^--FeO_5 octahedral unit. The overlap between the Fe 3d and O 2p orbital leads to increased catalytic activity as discussed in previous sections.[172] The concentration of lattice oxygen vacancies increases with Sr^{2+} concentration (Figure 18d), allowing for more of this OH^--FeO_5 octahedral unit to be present at one time in the catalyst, explaining the high performance seen in the x = 0.5 catalyst. The improved OER performance of perovskite oxide catalysts through oxygen vacancy creation via A site doping is also observed in similar systems, which show comparable performance to the PSFO catalysts documented in this study.[140, 159, 160, 173, 174] Figure 21 shows *iR* corrected CV scans where maximum current density response comes from the x = 0.5 sample.

There is an anomalous result in the cyclic voltammogram for x = 0.4 (Figure 21). This can be explained by the high concentration of carbonate present in the sample as determined by X-ray photoelectron spectroscopy (Figures 19c and 20). Increased carbonate concentration can

impair the performance of the OER catalytic reaction. The effect of the carbonate species on the catalyst are twofold. The carbonate interferes with the electrolyte by depleting charge carrying hydroxyl ions, lowering the overall conductivity of the electrolyte solution. The formed carbonates may also precipitate within the electrode, potentially blocking catalyst active sites, whilst also reducing the hydrophobicity of the electrode backing layer which can lead to structural degradation and electrode flooding.[169]
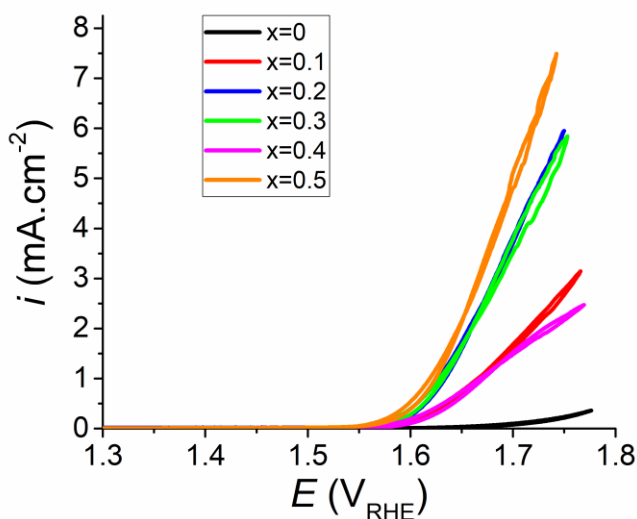
Figure 21 - Cyclic Voltammogrammes demonstrating the effect of higher Sr^{2+} doping on the electrocatalysis of the OER in $Pr_{1-x}Sr_xFeO_{3-\delta}$ perovskite oxides. CV analysis cycling between $1.30 - 1.80$ V_{RHE} at a scan rate of 5 mV s^{-1}, with a 0.1 M KOH electrolyte.

The onset potential for the OER, taken as the potential required to generate 1 mA cm^{-2} of current response, reduced in line with Sr^{2+} concentration, except for x = 0.4. The onset potential for the doped samples ranges from 1.67 V_{RHE} (overpotential, η = 440 mV) for x = 0.10 to 1.62 V_{RHE} (η = 390 mV) for x = 0.5. The improved performance with regards to the onset potential is a great success of this material design as the undoped $PrFeO_{3-\delta}$ (x = 0) material did not produce a current response of 1 mA cm^{-2} even at a potential of 1.70 V_{RHE} in half-cell testing. Lowering onset potentials is a critical metric in designing materials for electrolyser anodes due to the cost factor and durability associated with long-term operation of electrolyser systems.

Figure 22 highlights the huge difference in the electrical impedance response between the undoped sample with the doped ones, with the highest doped x = 0.5 material having the lowest polarisation resistance, R_p. These measurements were taken at 1.70 V_{RHE} as this is in the active

electrochemical region as shown in Figure 21. All tested materials showed a semi-circle behaviour, with similar values for the total ohmic resistance, R_s.
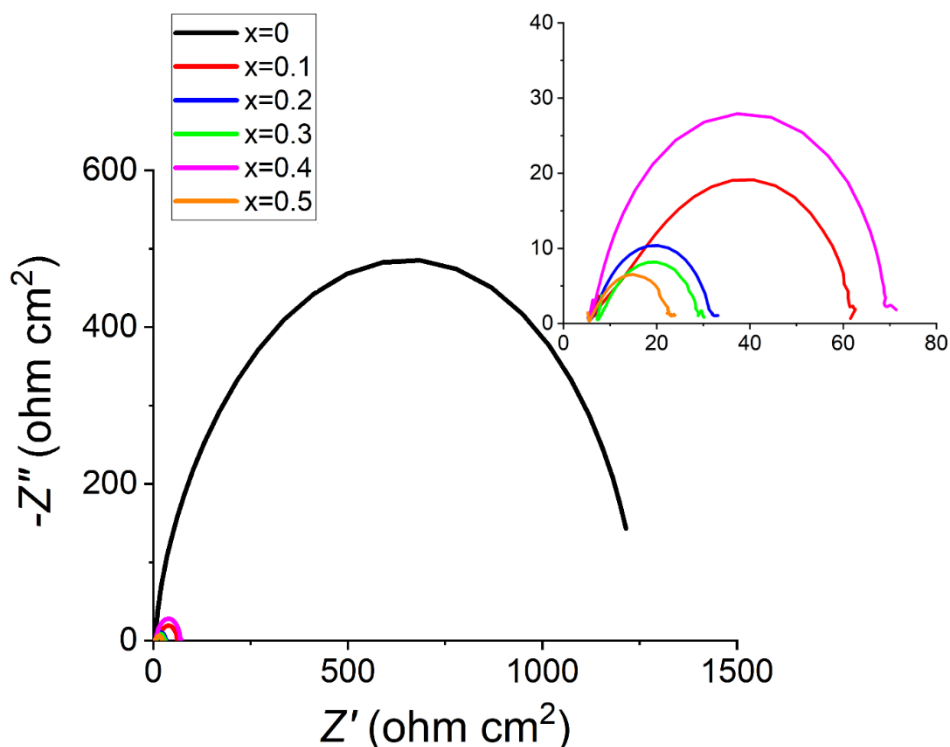
Figure 22 - EIS Measurements taken at 1.70 V_{RHE} demonstrating the drastic difference in between doped and undoped PSFO perovskite oxides. No significant difference was observed in EIS measurements before and after cyclic voltammetry scans.

The undoped $PrFeO_{3-\delta}$ has a Tafel slope of ~ 108 mV dec^{-1}, when compared to around 50 mV dec^{-1} for the doped catalyst perovskite oxides (Figure 23). The 60 mV dec^{-1} shift is indicative of a possible change in the rate limiting reaction. The 4-electron OER reaction per mole of oxygen consists of 4 reactions (equations 4-7) on the transition metal surface (*M*), each of which can act as the rate determining step,

$$M + OH^- \leftrightarrow MOH + e^- \tag{4}$$

$$MOH + OH^- \leftrightarrow MO + H_2O + e^- \tag{5}$$

$$MO + OH^- \leftrightarrow MOO^- + H_2O \tag{6}$$

$$MOO^- \leftrightarrow M + O_2 + e^- \tag{7}$$
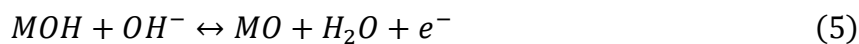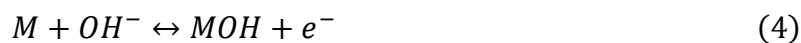
Kinetic simulations undertaken by Shinagawa *et al.* (2015) determined that for electrocatalysis of the oxygen evolution reaction where the Tafel slope is around 120 mV dec^{-1}, as is the case for the x = 0 material, then the reaction is rate limited by the formation of the metal oxide bond (equation 4). The reductive tendency in the Tafel slope seen when Sr^{2+} is introduced to the unit cell tends towards the OER rate limiting step to be shifted to the formation of the peroxide bond on the metal surface (equation 6), or the desorption of O$_2$ from the metal surface (equation 7).[175]
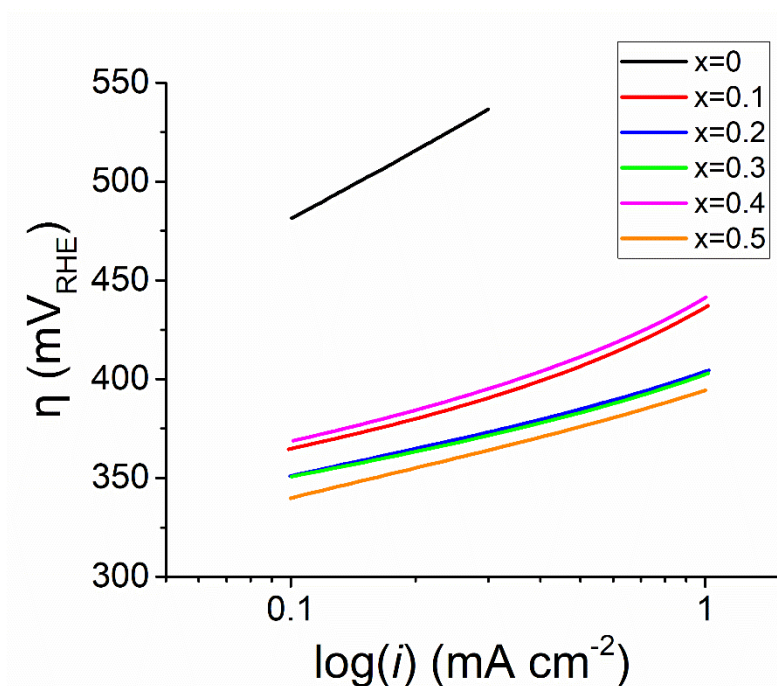
Figure 23 – Tafel plots of all PSFO perovskite oxides. The difference between the undoped x=0 and the Sr^{2+} doped samples (x=0.1 – 0.5) is clearly shown. The reduction of the Tafel slope is indicative of a shift in the limiting reaction in the 4-electron oxygen evolution reaction.

Figure 24 shows forward cyclic voltammetry measurements for x = 0, 0.2, and 0.5 at 20 °C, 40 °C, 60 °C, and 80 °C in the full cell configuration. As expected, the current response of the material increases with increased temperature. Electrolyser tests confirm electrochemical results from half-cell testing (Figure 6), in that the addition of Sr^{2+} cations increases the electrocatalytic performance of the PSFO catalysts with regards to the oxygen evolution reaction. At an operating temperature of 80 °C the overpotential (η) required to elicit a current response of 10 mA cm^{-2} is

442 mV, 353 mV, and 335 mV for x = 0, 0.2, and 0.5 respectively; and for 150 mA cm^{-2} the overpotential required is 752 mV and 680 mV for x = 0.2 and 0.5 respectively.
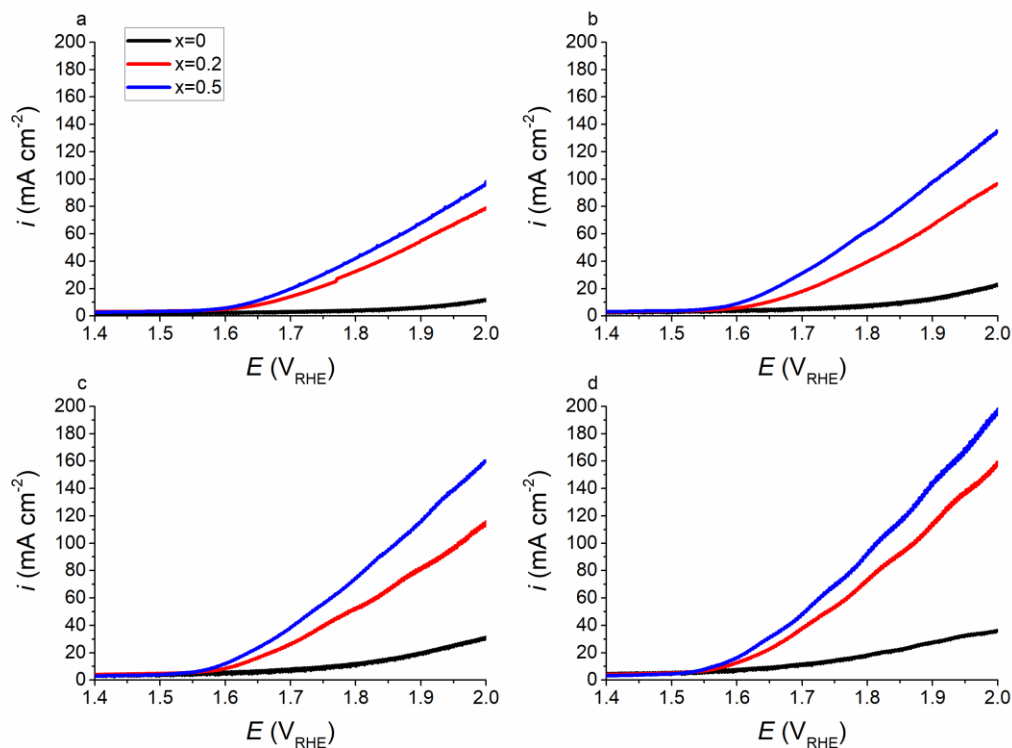
Figure 24 – Cyclic Voltammograms using Pt/C as a cathode material, PSFO x = 0, 0.2, and 0.5 as anode material, LDPE with VBA as a radiation grafted Anion Exchange Membrane, and an electrolyte of 0.1 M NaOH. Cycles measured at temperatures of a) 20 °C, b) 40 °C , c) 60 °C , and d) 80 °C.

4.4 4. Conclusions

Praseodymium strontium ferrite perovskite oxides with the formula of $Pr_{1-x}Sr_xFeO_{3-\delta}$ (x = 0 , 0.1, 0.2, 0.3, 0.4, 0.5) have been successfully synthesised by wet chemistry citrate sol gel method, and have demonstrated increased OER electrocatalytic activity for higher values of x. The mechanism behind the increased activity due to the addition of Sr^{2+} via A site substitution of Pr^{3+} to the perovskite lattice is attributed to increased oxygen vacancy concentration allowing for a higher availability of the B site transition metal catalyst surface, a shift in the average oxidation state of the B site iron ion leading to a d shell e_g electron orbital filling closer to the well-defined activity descriptor of unity, all of which allows for higher electron-ion conductivity and catalyst activity. This improvement is especially impressive as the undoped $PrFeO_{3-\delta}$ (x = 0) material was demonstrated to be essentially inactive towards oxygen evolution at 1.70 V_{RHE} in 0.1 M KOH

78

electrolyte in 3 electrode setups and requiring relatively high overpotentials and operating temperatures in order to start becoming active in electrolyser cells, compared to the performance of the A site doped material. This relatively small change to the stoichiometry of the material, whilst retaining the crystal structure of perovskites, demonstrates how the OER performance can be further enhanced with the implementation of more environmentally and economically attractive materials.

4.5 Appendix
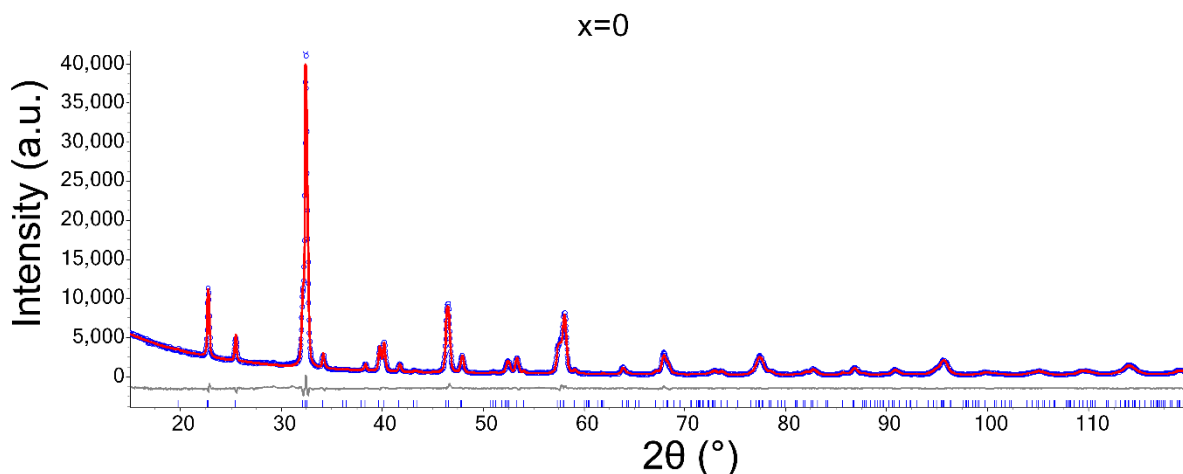
Figure 25 – Rietveld plot of the powder XRD data for PrFeO$_{3-\delta}$ (x = 0). This data was collected at room temperature and under ambient pressure. The observed intensity is shown in blue, the calculated intensity is shown in red, and the difference is shown in grey underneath. Vertical markers indicate Bragg reflections. (R$_{wp}$ = 4.76%, R$_{Bragg}$ = 1.55%).
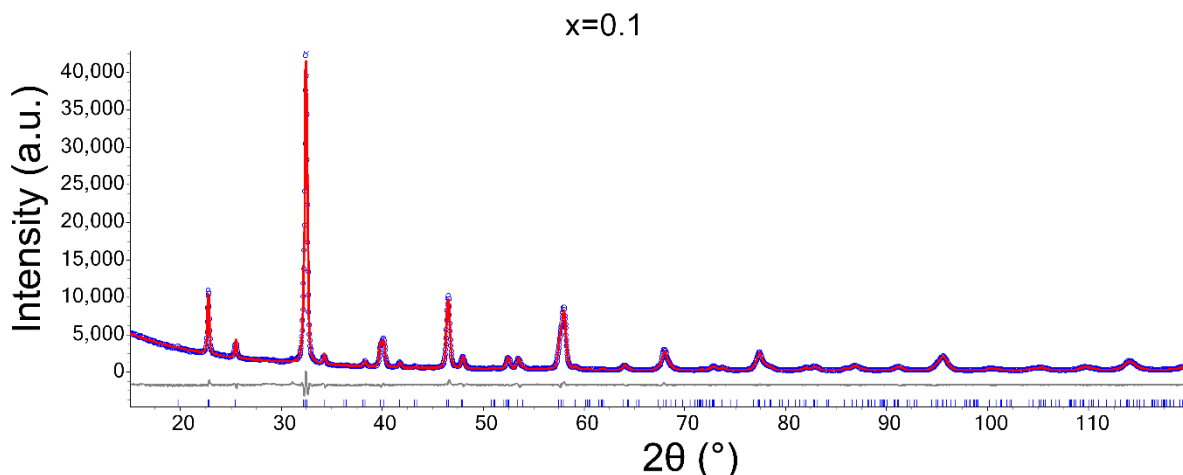
Figure 26 – Rietveld plot of the powder XRD data for Pr$_{0.90}$Sr$_{0.10}$FeO$_{3-\delta}$ (x = 0.1). This data was collected at room temperature and under ambient pressure. The observed intensity is shown in blue, the calculated intensity is shown in red, and the difference is shown in grey underneath. Vertical markers indicate Bragg reflections. (R$_{wp}$ = 5.10%, R$_{Bragg}$ = 1.57%).

x=0.2
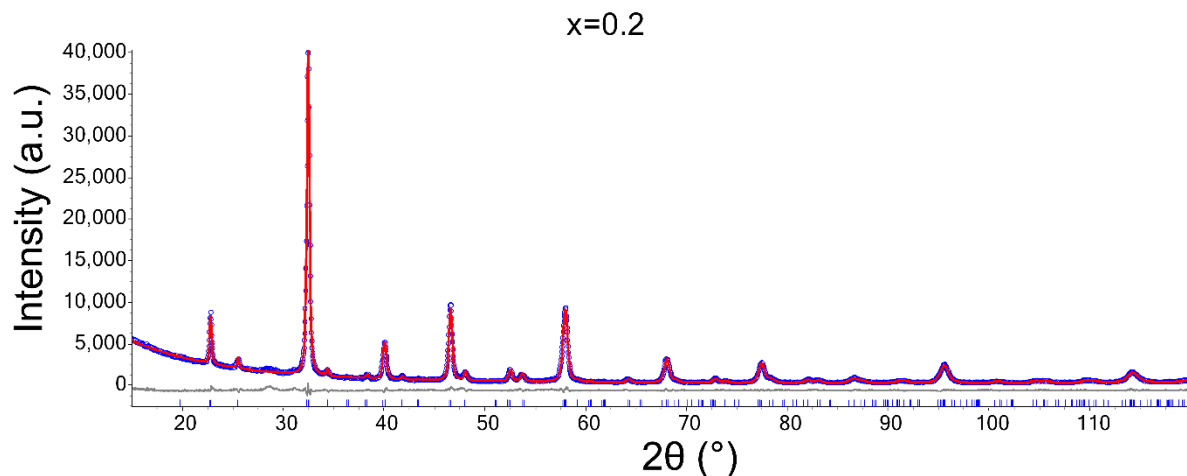
Figure 27 – Rietveld plot of the powder XRD data for $Pr_{0.79}Sr_{0.21}FeO_{3-\delta}$ (x = 0.2). This data was collected at room temperature and under ambient pressure. The observed intensity is shown in blue, the calculated intensity is shown in red, and the difference is shown in grey underneath. Vertical markers indicate Bragg reflections. (R_{wp} = 5.23%, R_{Bragg} = 1.18%).

x=0.3
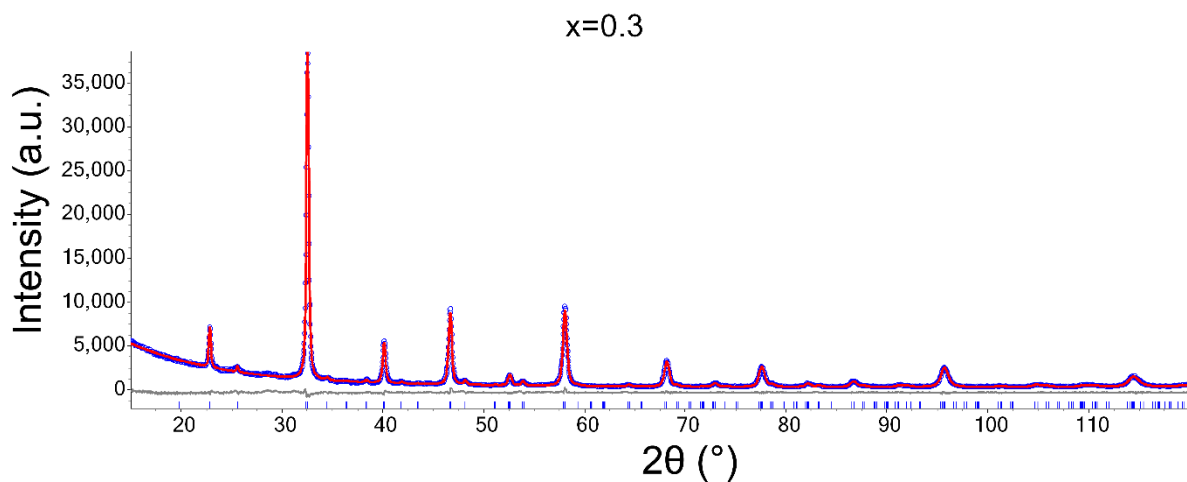
Figure 28 – Rietveld plot of the powder XRD data for $Pr_{0.70}Sr_{0.30}FeO_{3-\delta}$ (x = 0.3). This data was collected at room temperature and under ambient pressure. The observed intensity is shown in blue, the calculated intensity is shown in red, and the difference is shown in grey underneath. Vertical markers indicate Bragg reflections. (R_{wp} = 4.71%, R_{Bragg} = 1.31%).
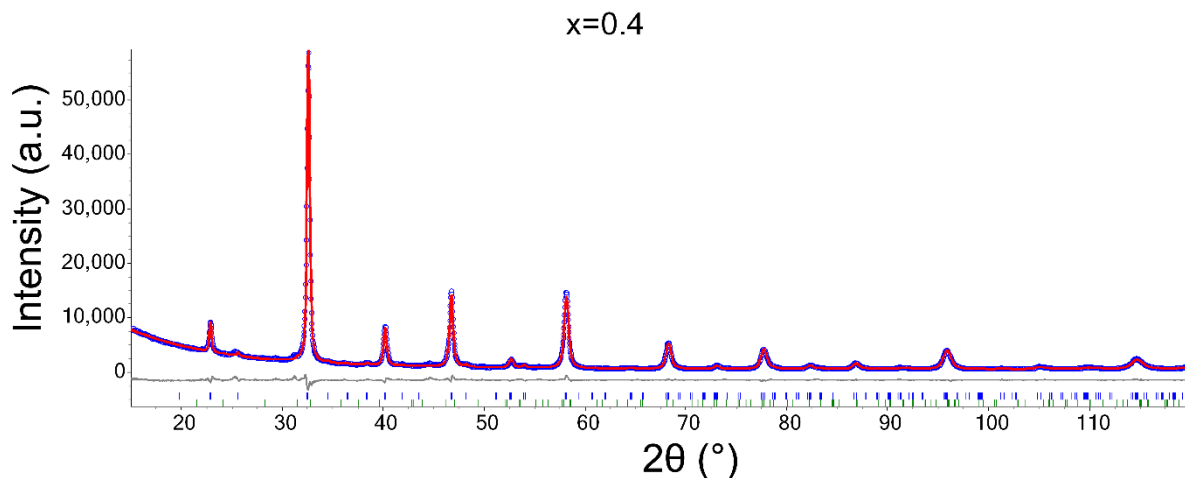
Figure 29 – Rietveld plot of the powder XRD data for $Pr_{0.58}Sr_{0.42}FeO_{3-\delta}$ (x = 0.4). This data was collected at room temperature and under ambient pressure. The observed intensity is shown in blue, the calculated intensity is shown in red, and the difference is shown in grey underneath. Vertical markers indicate Bragg reflections of 99.04(9) wt.% P6S4FO (top) and 0.96(9) wt.% Pr_2FeO_4 (bottom) phases (R_{wp} = 5.23%, R_{Bragg} = 1.71%).
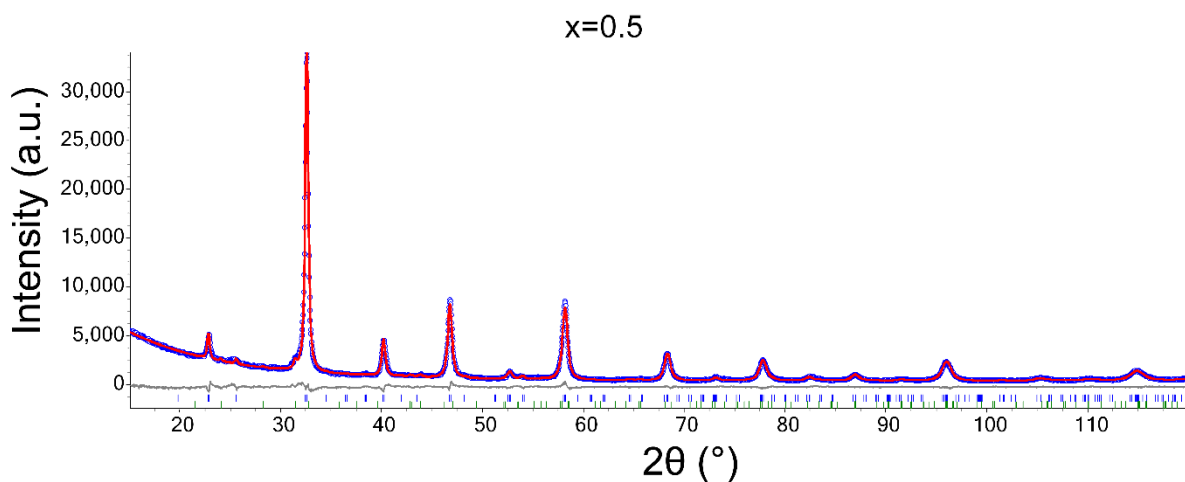
Figure 30 – Rietveld plot of the powder XRD data for $Pr_{0.48}Sr_{0.52}FeO_{3-\delta}$ (x=0.5). This data was collected at room temperature and under ambient pressure. The observed intensity is shown in blue, the calculated intensity is shown in red, and the difference is shown in grey underneath. Vertical markers indicate Bragg reflections of 96.95(1) wt.% P5S5FO (top) and 3.05(1) wt.% Pr_2FeO_4 (bottom) phases (R_{wp} = 5.24%, R_{Bragg} = 1.32%).
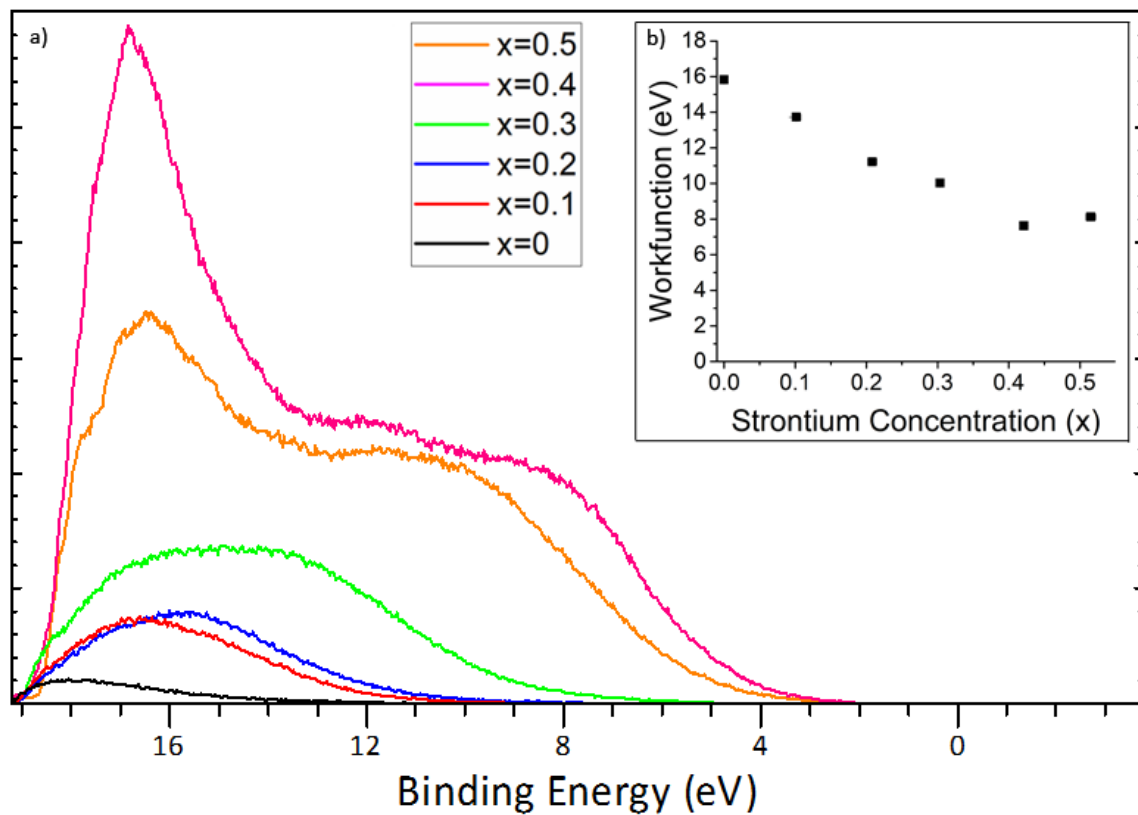
Figure 31 – a) Ultraviolet photoelectron spectroscopy (UPS) of PSFO perovskite catalysts. UPS Scans were used to calculate the workfunction values. b) Workfunction as a function of Sr^{2+} concentration.

Chapter 5. Effect the substitution of Co by Fe in PrBaCo$_{2(1-y)}$Fe$_{2y}$O$_6$ double perovskites has on the Oxygen Evolution Reaction

5.1 Introduction

This chapter will discuss how modifying the crystal structure from single perovskite oxides, as discussed in the previous chapter, to doubled perovskite can improve the catalytic activity of the material. Although this has been discussed in the review of the literature review, a brief description of the hypotheses will be provided. The initial hypothesis is that the catalytic activity of undoped double perovskite will be superior to that of an equivalent single perovskite oxide. Specifically, the addition of Ba^{2+} cations to the undoped PrFeO$_{3-\delta}$ from chapter 4 to create PrBaFe$_2$O$_6$ will increase the catalytic activity of the oxygen evolution reaction due to the doubling of the c lattice parameter, causing ordering of the oxygen vacancies along the z crystallographic axis.

The catalytic activity of the double perovskite oxides can be further increased by altering the stoichiometry of the B site transition metal through doping. This has been well documented as a method of improving the OER catalytic behaviour of the material, as discussed in the literature review chapter. Briefly, the catalytic performance of perovskite oxides for the oxygen evolution reaction is intrinsically linked to the filling of the 3d e$_g$ antibonding orbital of the transition metal. In their groundbreaking paper, Suntivich *et al*[41] determined through molecular orbital principles that there exists a volcano relationship between the 3d e$_g$ filling and the catalytic activity, with the highest activity being found around a filling of ~1.2. Obviously, a molecular orbital can only have an integer unit filling, so by modifying the stoichiometric ratio of transition metal elements we can design a material in which the average 3d e$_g$ filing is a non-integer value. Therefore, it is hypothesized that having mixed iron/cobalt cations on the B site will show a improvement in the oxygen evolution reaction.

5.1.1 Chapter Hypotheses

- The catalytic activity of double perovskites will be superior to single perovskites, specifically PrBaFe$_2$O$_6$ and PrFeO$_3$.

- Mixed cobalt/iron stoichiometries will provide higher performance than intrinsic $PrBaCo_{2(1-y)}Fe_{2y}O_6$ perovskite oxides.

5.2 Material Characterisation

5.2.1 The Pseudo-cubic Unit Cell

The PBCF materials were synthesized as per the procedure outlined in the materials and methods chapter (chapter 3). A range of stoichiometries were synthesized, with an iron doping concentration (y) of 0, 0.2, 0.5, 0.8, and 1 (denoted as PBCO, PBCF-2, PBCF-5, PBCF-8, PBFO respictvely). The PBCF materials were characterized by ambient temperature powder X-Ray Diffraction (XRD), and the resulting diffraction patters were fit using Rietveld method.[114] The powder diffraction patterns were refined using tetragonal space group *P4/mmm* (Z = 2) (space group number 123) for y = ≤0.5, and cubic space group *Pm$\bar{3}$m* (space group number 221) for y = ≥0.8. This is consistent for similar materials found in the literature.[176, 177] As the value for y increases, the material moves towards a cubic symmetry. The relationship between an ideal cubic and ideal tetragonal geometry is that in tetragonal geometry, the *c* parameter will be double the length of the *a* parameter, and the *a* parameter will be the same for both tetragonal and cubic. Therefore, in order to provide a clearer indication of the phase change of the behaviour, the tetragonal *c* lattice parameters are shows as half of the measured length which is denoted by *c'*. Lattice parameters and their pseudo-cubic representations from the PBCF perovskite oxides are listed in Table 6.

Table 6 – Unit cell parameters for PrBaCo$_{2(1-y)}$Fe$_{2y}$O$_6$, with errors in parenthesis.

Fe (y)	Space Group	Lattice Parameter (Å)			Vol (Å³)	Vol' (Å³)
		a = b	c	c'		
0	*P4/mmm*	3.8981(2)	7.6434(5)	3.8217(3)	116.15(2)	58.07(1)
0.2	*P4/mmm*	3.8949(3)	7.6854(7)	3.8417(3)	116.59(2)	58.29(1)
0.5	*P4/mmm*	3.9148(2)	7.7174(4)	3.8587(2)	118.27(1)	59.14(1)
0.8	*Pm$\bar{3}$m*	a = b = c = 3.9148(5)			60.00(2)	
1.0	*Pm$\bar{3}$m*	a = b = c = 3.9338(2)			60.87(1)	

5.2.2 Crystal Structure

The resulting powder diffraction patterns for the PBCF double perovskite series are shown in Figure 32. The diffraction patterns indicate the presence of the predicted pure perovskite phase within the detection limits of the XRD instrument. Additional peaks representing impurity phases can be observed in the iron rich stoichiometries (y ≥ 0.8), which have been indexed as small amounts (≤5 wt%) of ABO_3 single perovskite and $A_{n+1}B_nO_{3n+1}$ Ruddlesden-Popper phase. The formation of these impurity phases has been previously discussed in the literature[178] and due to the small amounts it is assumed that these phases play an insignificant part in any catalytic reactions. However, these phases have been considered during the refinement of the data in order to get accurate unit cell parameter volumes. Rietveld fits for the 5 samples are shown in figures Figure 46 to Figure 50.

As previously discussed, the higher cobalt containing materials (y ≤0.8) have been characterized in a tetragonal space group (*P4/mmm*, space group number 123). From a visual inspection of the PBCF powder diffraction patterns (Figure 32) it can be observed that the main perovskite peak located around 32 – 33 °2θ is a singlet for the high iron stoichiometries (y≥0.8), and a doublet for the high cobalt stoichiometries (y≤0.5). The singlet peak observed in PBCF-8 and PBFO is indexed as a (110) Bragg reflection, which splits into (102) and (110) reflections for the higher cobalt stoichiometries. This peak splitting is indicative of the lower symmetry tetragonal *P4/mmm* space group with doubling along the *c* crystallographic axis and is consistent with structural characterisation studies of other tetragonal double perovskites.[179-184]

Interestingly, the addition of a dopant into the double perovskite lattice leading from a lower to higher symmetry system is the same trend that was observed in the results of the PSFO material series (chapter 4), with higher Sr^{2+} doping concentration leading to a higher symmetry pseudo-cubic unit cell. However, the isovalent B-site doping mechanism in PBCF double perovskites is an entirely different process compared to aliovalent A-site doping in PSFO ($Pr_{1-x}Sr_xFeO_{3-\delta}$) single perovskite oxides, and thus the effects on both the electrochemical performance and the crystal structure will be different. This chapter will provide discussion about the primary differences observed between these 2 processes, and how this may be used to produce a high-performance catalyst.
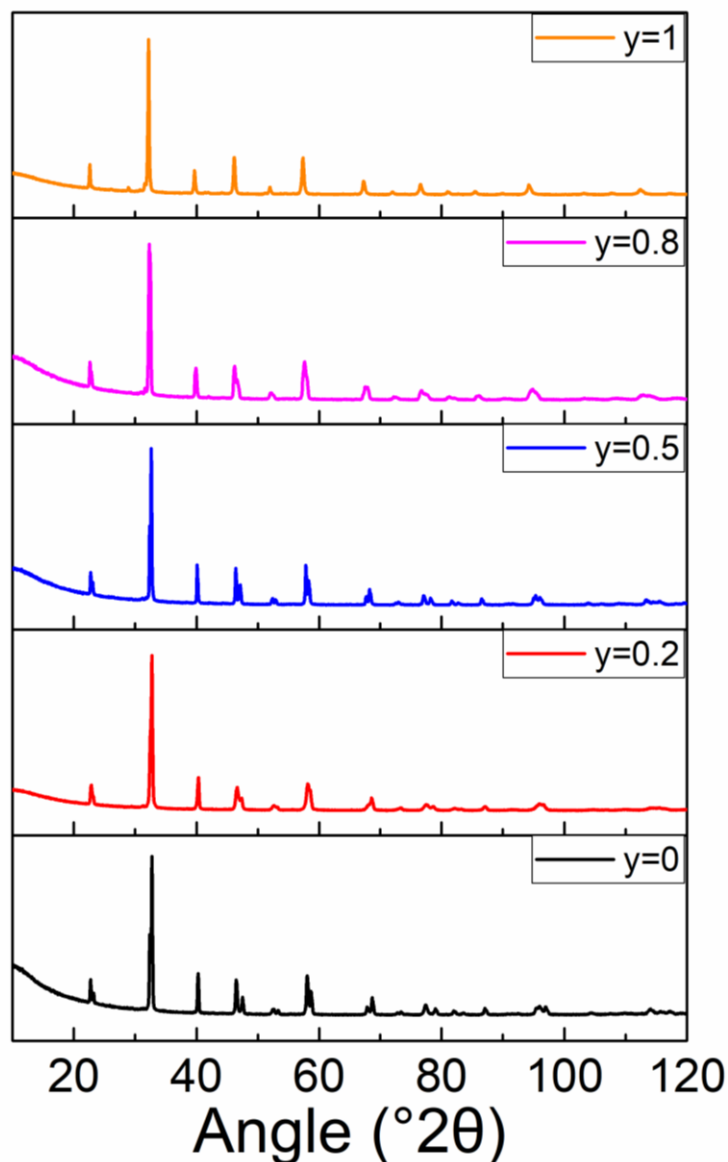
Figure 32 – Diffraction patterns for the PBCF double perovskite series

During the process of refining the powder diffraction data using Rietveld method, fundamental parameter peak shape profile[117] and X-ray form factors of Pr^{3+}, Ba^{2+}, Co^{3+}, Fe^{3+} and O^{2-} were used. For each data set, Chebychev polynomial (7 order) and $1/x$ background, a zero error, unit cell parameters, scale factors, crystal size/strain were refined sequentially, whilst the occupancy of the cations was constrained to unity.
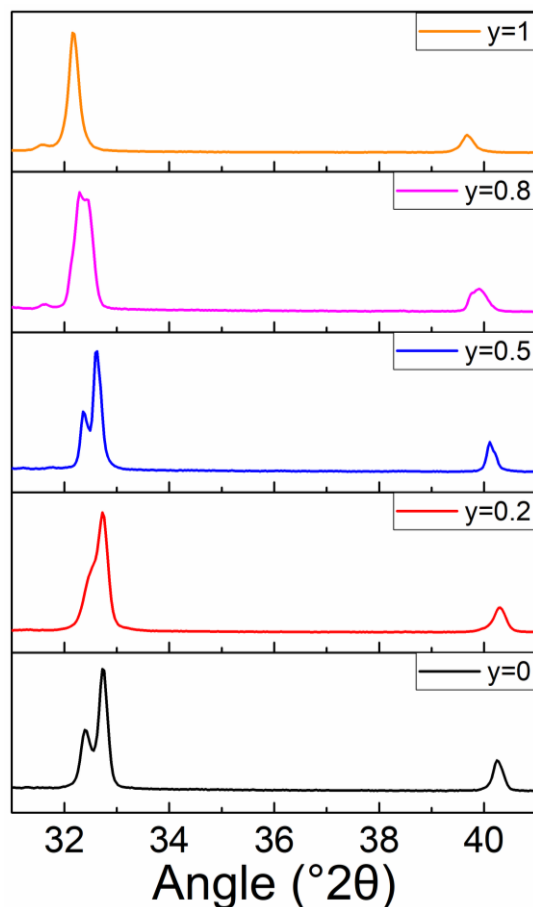
Figure 33 – Powder XRD patterns of the PBCF double perovskite oxides, with a °2Θ range of 30 – 42 to highlight the shift towards a lower angle as iron concentration increases, indicative of an expansion of the unit cell.

Unit cell parameters shown in Table 6 show an expansion of both the lattice parameters and the unit cell volume as the concentration of iron (y) increases. This can also be seen by observing the peaks in the powder diffraction patterns as shown in Figure 33, which depicts a shift towards lower a lower °2θ diffraction angle which is indicative of a unit cell expansion. As previously discussed, this can be determined from Bragg's law which states that as lattice spacing increases (through unit cell expansion or other means), the measured diffraction angle decreases. Figure 33 also displays the peak splitting from a (110) singlet into (110) and (102) doublet, showing an increase of the symmetry of the material as iron content increases.
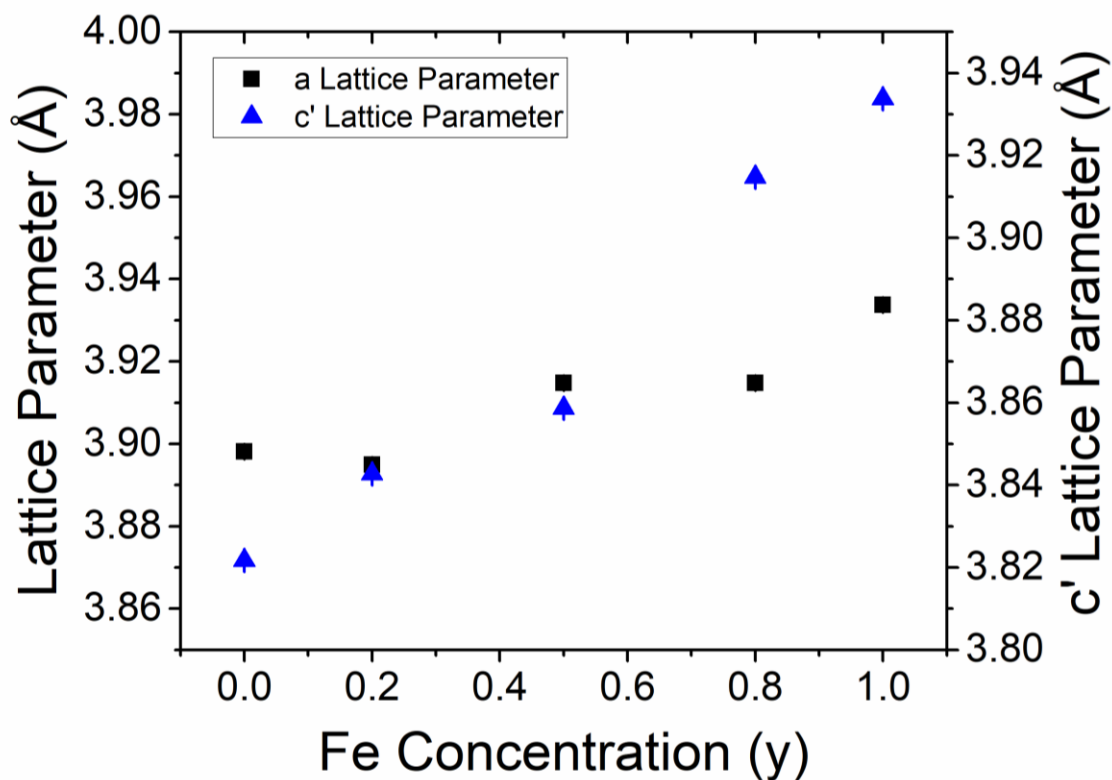
Figure 34 – Pseudo-cubic lattice parameters of the PrBaCo$_{2(1-y)}$Fe$_{2y}$O$_6$ double perovskite series against Fe doping concentration.

Figure 34 shows the relationship between dopant concentration and lattice parameters. As discussed, the *c* lattice parameter is displayed as pseudo-cubic to allow like for like comparison between the *P4/mmm* and the *Pm$\overline{3}$m* materials. The pseudo-cubic lattice parameter is denoted as *c'*. Similar to what was observed in the PSFO (Pr$_{1-x}$Sr$_x$FeO$_{3-\delta}$) perovskite oxides (Chapter 4), the biggest change in the lattice parameters when dopants are introduced to the materials is along the *c* lattice parameter, whereas the *a = b* lattice parameters remain relatively unchanged. For PBCF double perovskite oxides this change is a predictable one, as doubling along the *c* crystallographic axis is characteristic of the tetragonal *P4/mmm* structure, and this is typically where lattice defects will manifest, such as oxygen vacancies on the Ba-O layer, which affords more flexibility within the lattice. It is also clear from observations of the *c'* lattice parameter in Figure 34 that there is a phase transition occurring between y = 0.5 and y = 0.8, as made apparent by the sharp increase in the *c'* lattice parameter between those two points. This observed phase transition does not appear to have had any significant effect on the electrocatalytic activity of the material, which will be discussed further on in this chapter. However, the specific mechanism of

this phase change and stoichiometry at which it occurs, and what effects this has on the properties of the material is not often discussed within the literature, which presents a novel opportunity for future materials research.
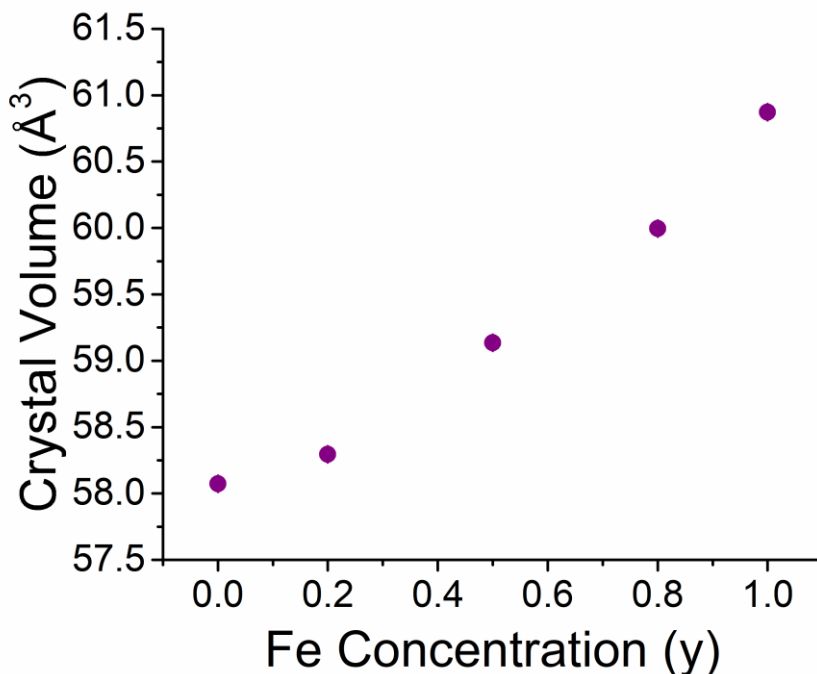
Figure 35 – Unit cell volume for the PBCF double perovskite oxide series. Values have been normalised by formula unit (Z) to allow for material comparison.

The relative volume of the unit cell for the PBCF double perovskite oxides is displayed in Figure 35. In order for a like for like comparison, the values have been normalised by the number of formula units per unit cell, denoted as *Z*. For the *Pm$\bar{3}$m* (cubic) material, the number of formula unit cells is equal to 1, and for the *P4/mmm* (tetragonal) unit cells *Z* is equal to 2. These normalised values are listed in Table 6 under the column titled Vol'.

The primary mechanism behind the increase in the lattice parameters and the unit cell volume is intuitive, as in 6-coordination high spin complexes, the ionic radii of Fe^{3+} is larger than that of Co^{3+} (0.645 Å and 0.61 Å respectively).[154] Replacing a smaller cation with a larger one will increase the overall unit cell volume of the material.

5.2.3 Bond Valence Sum and Bond Length

Bond valence sum (BVS) analysis[157] which gives an estimation of the strength of a bond in ionic compounds was calculated for the PBCF double perovskites using equation 1.

$$s_i = \sum exp^{\frac{(R_0 - R)}{B}} \tag{1}$$

Where s_i is the bond valence sum, R_0 and B are previously determined parameters,[157] and R is the bond length.[158] When determining the BVS of the B site cation, 1.685 Å and 0.370 were used to the R_0 and B respectively. For the calculation of the bond valence sum it was assumed that all B site cations were in a high spin configuration. Bond valence sum values for the PBCF double perovskite series are shown in Figure 36.
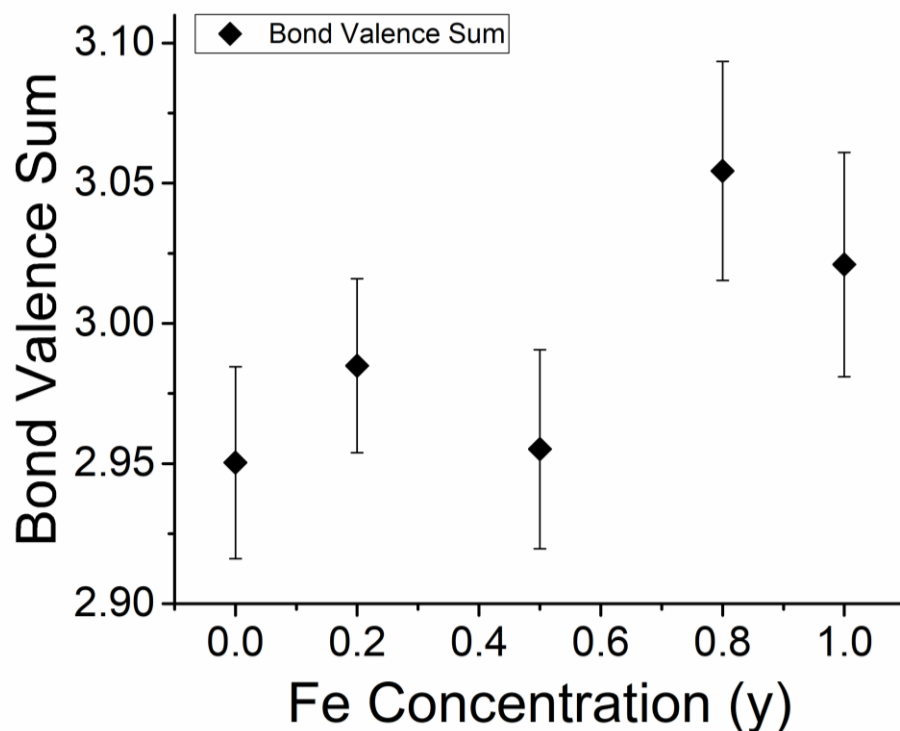
Figure 36 – Bond Valence Sums (BVS) for PrBaCo$_{2(1-y)}$Fe$_{2y}$O$_6$ double perovskites, showing an approximation of the bond strength at varying Co:Fe stoichiometries.

As discussed, bond valence sum values can provide an insight into the bonding strength in ionic environments. Figure 36 clearly indicates that the overall bonding environment is slightly weaker in the *P4/mmm* tetragonal material relative to the *Pm3̄m* cubic material. This is to be expected due to the closer packing of the atoms in a Z = 1 cubic unit cell compared to a Z = 2 tetragonal unit cell. However, as the variation in the bond valence sum is fairly low (most of the values are within error of each other), and the nature of the bond valence sum being an approximate calculation due to the oxidation state of the B-site transition metal cation, no solid conclusions should be drawn from the bond valence calculations alone. However, it is still a useful

metric, as the strength of the bond between the transition metal cation and the incoming oxygen species is an integral part of optimizing the electrocatalytic performance of oxygen evolution anodes.
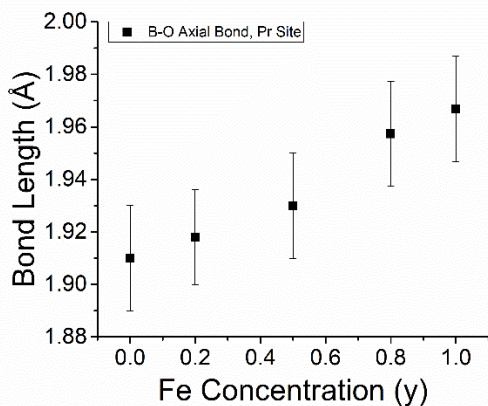
Figure 37 – A site axial B-O bond length
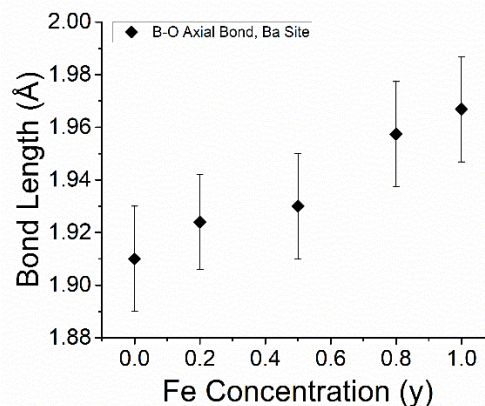
Figure 38 – A' site axial B-O bond length
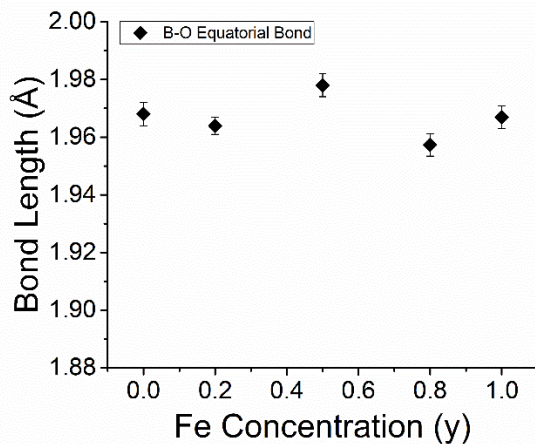
Figure 39 – Equatorial B-O bond length
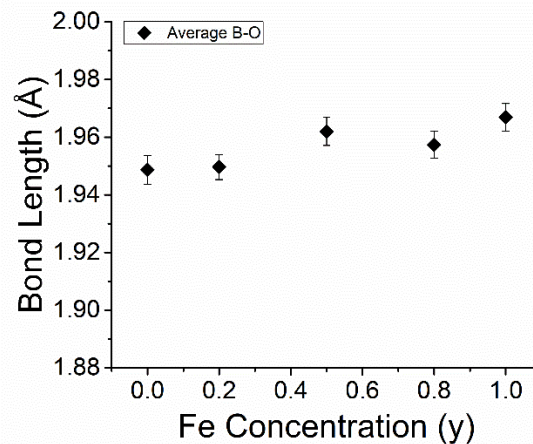
Figure 40 – Total average B-O bond length

The different transition metal to oxygen bond environments are displayed in Figure 37 – Figure 40. It is clear from Figure 37 and Figure 38 that increased iron dopant concentration increases the bond length of the axial metal oxygen bonds. This is in line with previous discussion, as the axial metal oxygen bonds align along the *c* crystallographic axis. Interestingly, the values for the A and A' site axial bonds are almost identical for the PBCF material, with the exception of PBCF-2 ($PrBaCo_{1.6}Fe_{0.4}O_6$), where the A' bond length is slightly longer compared to the A site bond. This is an interesting observation as any oxygen vacancies that are present in the material will exist in the A' plane, which was discussed in PSFO chapter and literature review can increase the

oxygen evolution activity. However, the increase in the bond length is ultimately in line with the increased ionic radius of the Fe cation as it replaces the Co cation.

5.3 Electrochemistry

5.3.1 Cyclic Voltammetry

Cyclic voltammograms showing the electrocatalytic performance of the material as OER electrodes are showing in Figure 41. From the resulting scans, it is clear that a mixed B-site material delivers better overall electrocatalytic activity when compared to undoped $PrBaCo_2O_6$ and $PrBaFe_2O_6$, with the mixed B site material generating a current response in the range of 2.85 – 3.38 mA cm^{-2} at 1.70 V_{RHE}, compared with 1.66 – 2.28 mA cm^{-2} for the undoped material at the same potential. In this study the results indicate that PBCF-2 ($PrBaCo_{1.6}Fe_{0.4}O_6$) is the optimal stoichiometry, as this material generated the highest amount of oxygen gas, as shown by the high current density in Figure 41. The comparative performance of the undoped materials is also of note, as the cobalt saturate material outperforms the iron saturated material. The performance of the doped material being higher than that of the undoped material is consistent with the hypothesis for this chapter, and the cobalt material outperforming the iron material, based on *d* shell electron states is consistent with findings for similar catalytic materials in the literature.[41, 185-188]

Furthermore, the intrinsic nature of the double perovskite structure delivers considerably higher performance than that of single perovskite oxides, with $PrBaFe_2O_6$ out-performing undoped $PrFeO_3$ single perovskite oxide by some orders of magnitude. This increase in the activity is often theorised in the literature to be related to the ordering of oxygen vacancies along a specific crystallographic plane due to vacancies manifesting on the A' site, due to the difference in A and A' site cation's ionic radii.[189] As previously discussed in the review of the literature (chapter 2) and $Pr_{1-x}Sr_xFeO_{3-\delta}$ results chapter (chapter 4) , the introduction of an oxygen vacancy, the coordination of the B-site transition metal to oxygen bond (M–O) will be reduced from 6 to 5. The 5 coordinated M-O unit provides a higher availability of the B site 3d orbital for the 2p orbital of the absorbed oxygen species (in this case a hydroxyl (OH-) ion due to the alkaline nature of the electrolyte), creating an intermediate OH-MO5 octahedral unit. Due to the nature of the double perovskite, this oxygen vacancy will be ordered along the c lattice plane. Due to Fe doping

in the B site of the higher performing catalysts (PBCF-2, PBCF-5, and PBCF-8) the overall filling of the 3d eg antibonding orbital will be closer to 1 than in the undoped PBCO and PBFO. This altered eg filling facilitates higher electron transfer between the metal oxide catalyst surface and the adsorbed oxygen species, and thus increases the rate of the electrochemical reaction, leading to the higher performance shown in Figure 41. This increased activity from double perovskite oxide electrocatalysts is well documented within the literature.[190-193]
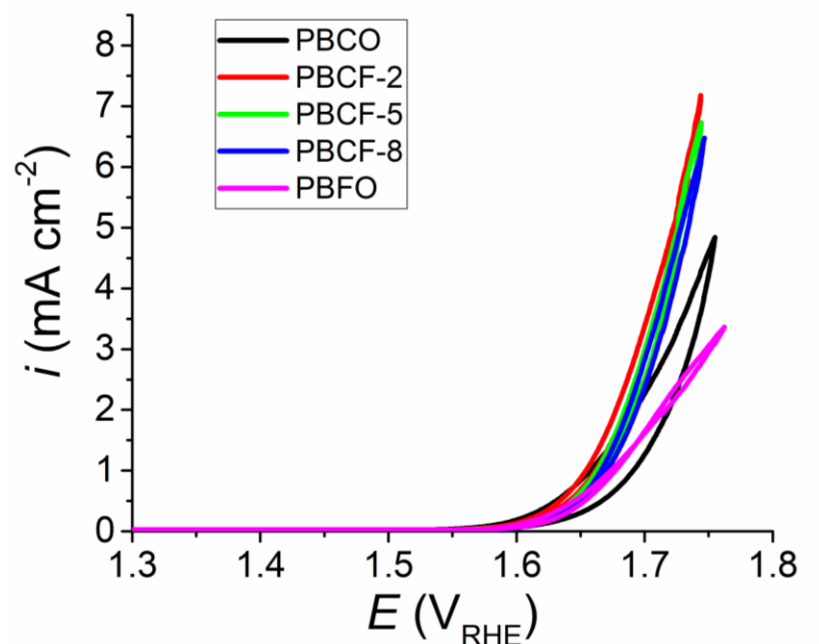
Figure 41 – iR corrected Cyclic Voltammetry (CV) scans of PBCF perovskites in 0.1 M KOH electrolyte, scanned over a potential range of 1.30 – 1.80 V_{RHE} with a scan rate of 5 mV s^{-1}.

The *iR* corrected peak current density determined during the cyclic voltammetry scans for the PBCF double perovskite oxide electrocatalysts occur at around 1.75 V_{RHE}, as well as literature values for similar systems, are listed in Table 7 below. It is clear from the values shown in Table 7 that the B-site doped PBCF double perovskite oxides that were analysed in this work are consistent, and in some cases out-perform other catalyst materials.

Table 7 – Current density measurements of various perovskite oxides acting as oxygen evolution electrocatalysts in alkaline media. Results are compared with those gained within this thesis and from literature.

Material	Electrolyte	Current Density @ ~1.75 V_{RHE} (mA cm^{-2})	Reference
PBCO	0.1 M KOH	4.84	This Study
PBCF-2	0.1 M KOH	7.18	This Study
PBCF-5	0.1 M KOH	6.73	This Study
PBCF-8	0.1 M KOH	6.48	This Study
PBFO	0.1 M KOH	3.36	This Study
$Pr_{0.5}Sr_{0.5}FeO_3$	0.1 M KOH	7.49	This Study
$PrBaCoO_6$	1.0 M KOH	2.00	[194]
$CaCu_3Ti_4O_{12}$	0.1 M KOH	6.00	[195]
$Ba_2Sc_{0.2}Co_{1.7}O_6$	0.1 M KOH	3.00	[196]
$Ba_{0.9}Bi_{0.1}Sc_{0.2}Co_{1.7}O_6$	0.1 M KOH	5.00	[196]
$Ba_{08}Bi_{0.2}Sc_{0.2}Co_{1.7}O_6$	0.1 M KOH	4.00	[196]
$Ba_{0.7}Bi_{0.3}Sc_{0.2}Co_{1.7}O_6$	0.1 M KOH	4.00	[196]
$PrBaCo_2O_6$	0.1 M KOH	1.80	[196]

Interestingly for the $PrBaCo_2O_{6-\delta}$ (PBCO) material, a noticeable degree of hysteresis is observed in the CV scans compared to the other materials. Due to the multiple complex kinetic reactions taking place at the electrode during the electrocatalytic process, it is not so simple to narrow down one reason as to why hysteresis would appear in cyclic voltammetry scans. There are a few different reasons why hysteresis may appear during cyclic voltammetry, but the most common mechanisms associated with hysteresis arise in CV scans of metal catalysts arise from either material capacitance,[197] or the formation of catalytically inactive species at the surface of the electrode.[198] Although distinguishing between mechanisms of hysteresis in cyclic voltammograms is complex and requires computational modelling alongside experimental data, ultimately the effect of the hysteresis in the PBCO material does not appear to have had much of an effect on the electrochemical performance, as this is in line with previously discussed literature

and hypothesis. However, analysis of the electrical impedance spectroscopy (EIS) shows no significant difference in the capacitance of the PBCO material, so it would stand to reason that the hysteresis seen in Figure 41 may be due to the formation of inactive metal oxides at the surface of the electrocatalyst.

5.3.2 Electrical Impedance Spectroscopy

Nyquist plots for obtained via electrical impedance spectroscopy (EIS) measurements for the PrBaCo2(1-y)Fe2yO6 (PBCF) double perovskite oxide electrocatalysts are shown in Figure 42. The solution resistance (R_s), the point of the real impedance (Z') where the imaginary impedance (-Z'') is equal to 0, for all materials lies at very similar points which indicates that similar electrolyte concentration was present for all electrochemical testing. This ensures that the difference in the electrocatalytic performance between the different material stoichiometries, best shown by cyclic voltammetry (Figure 41), is not a result of higher or lower electrolyte concentrations, but a direct effect of the difference in material properties. The value for the internal resistances is used in the results of the CV scans, giving *iR* corrected potentials which ensures that the performance of the electrocatalyst displayed in CV scans is true for the material and comparable between different 3 electrode cell set ups.
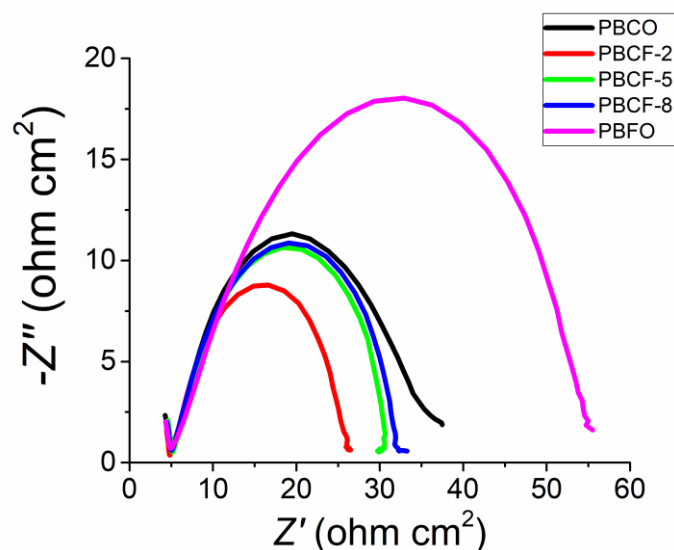
Figure 42 – Nyquist plots of the EIS measurements for the PBCF double perovskite oxide catalyst materials in 0.1 M KOH, measured 1.70 V$_{RHE}$

Polarisation resistance (R_p) is the resistance of a material species to oxidation from an externally applied voltage.[199] It is measured as the range between the points where the semi-

circle meets in *x* axis. In other words, it is measured as the point in the low frequency range minus the resistance arising from internal connections and the electrolyte solution (R_s). The polarisation resistances for the PBCF electrocatalysts shown in Figure 42 are in line with the current responses shown in Figure 41, with the highest polarisation resistance coming from the PBFO and PBCO, which display the lowest activity in the CV scans, and the smallest polarisation resistance arising from PBCF-2 ($PrBaCo_{1.6}Fe_{0.4}O_6$) which shows the highest current response in the CV tests.

The Nyquist plot of the impedance spectroscopy are an extremely useful metric for determining the performance and suitability of electrocatalysts. In particular, the capacitance of the electrocatalyst can be estimated through computational fitting of a particular model to the recorded data series. Although the main parameters to consider when designing a model for EIS data fitting are discussed in detail in the materials and methods section, a brief overview of model formulation is presented in this chapter for clarity.

When a model is developed for a specific process, there are a few key things to consider. The initial descriptor is what type of electrical process the material class can facilitate such as resistors or conductors. Perovskite based alkaline electrolyser anodes are generally considered semiconductors which, as the name suggests, are a class of materials where the level of conductivity is somewhere in between a conductor and an insulator. The second consideration is more specific to the chemical aspect of the electrochemical reaction. Alkaline electrolyser systems are composed of a liquid electrolyte in contact with a solid electrode, which causes a boundary known as double layer capacitance at the junction where the catalyst surface meets the electrolyte. When an electrical system contains a double layer which is an imperfect capacitor, such as in alkaline oxygen evolution electro catalysis, this is accounted for in the equivalent electrical circuit model by constant phase elements (CPE). As Nyquist plots show a range of frequencies, both the high and low frequencies (HF and LF) are taken into consideration within this model, as well as the internal resistances occurring from connections in the experimental set up and internal potentiostat wiring shown by a small, poorly defined, semi-circle at the high frequency (low value of Z') range,[200] and the resistances from the catalyst material displayed as the main semi-circle from Rs to Rp. As the difference between these two semi-circles is larger

than an order of magnitude, it is best to consider both semi-circles in the model.[201] The model used for the 3 electrode cell testing is shown in Figure 43.
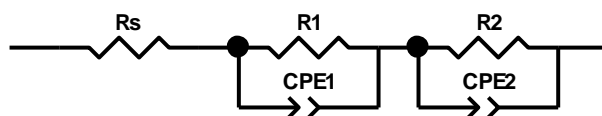
Figure 43 – Equivalent electrical circuit used for modelling EIS data, encompassing both semi-circles.

Where R_s models the resistance of the electrolyte, R_1 and CPE_1 are the resistance and constant phase element for respectively the initial semi-circle arising from internal resistances within the system, and R_2 and CPE_2 refer to the resistance and constant phase element for the semi-circle arising from the catalyst.

Each of the fitted parameters shown in Figure 43 can be used to calculate the approximate value for the capacitance of the material using equation 2.[202]

$$C = R^{\left(\frac{1-n}{n}\right)} \times Q^{\left(\frac{1}{n}\right)} \tag{2}$$

Where C is the capacitance (in Farads), R is the resistance, Q is the pseudo capacitance, and n is related to the shape of the semicircle (0 for a true insulator, and 1 for a true conductor).

The approximate capacitances, as well as the values used to calculate them are listed in Table 8. As this is an approximate value, care should be taken whilst drawing conclusions from the analysis. However, although the specific number is unlikely to be accurate, all materials are in the same order of magnitude being 10^{-4} Farads. As there are multiple different ways that capacitance is measured, depending on how important the analysis is for the study, and which specific capacitance is being measured, it is difficult to find like for like comparisons in the literature. However, as this method is the same for the PSFO ($Pr_{1-x}Sr_xFeO_{3-\delta}$) catalyst material discussed previously, a like for like comparison can provide some insight into the relative performance of the electrocatalysts.

Table 8 – Capacitance values for the PBCF double perovskite oxide oxygen evolution electrocatalysts with $Pr_{0.5}Sr_{0.5}FeO_3$ single perovskite oxide as a comparison.

Fe (y)	C (F)
0	3.00×10^{-4}
0.2	3.98×10^{-4}
0.5	2.53×10^{-4}
0.8	1.92×10^{-4}
1.0	3.89×10^{-4}
$Pr_{0.5}Sr_{0.5}FeO_3$	1.33×10^{-3}

5.3.3 Tafel slope and kinetics

Tafel plot analysis is a key metric for understanding the kinetics of the oxygen evolution reaction on the electrocatalyst surface. Simply, Tafel plots provide insight into kinetic factors of the electrochemical reaction such as the rate limiting reaction step and the exchange current density (i_o). The more commonly reported value for oxygen evolution anodes is the Tafel slope, which, as previously discussed in chapter 3, materials and methods, is derived from the Butler-Volmer equation, and describes the relationship between the rate of an electrochemical reaction and the overpotential. The equation for the Tafel slope is displayed in equation 3.

$$\eta = A \times \log_{10}\left(\frac{i}{i_o}\right) \tag{3}$$

Where η is the overpotential in volts, calculated from the *iR* correct measured potential minus 1.23 V (the thermodynamic limit of water splitting), *A* is the Tafel slope, *i* is the current density ($A.m^{-2}$) and i_o is the exchange current density ($A.m^{-2}$). The simplest method for determining the kinetic factors is linear fitting of lines on a Tafel plot, which is a plot of the current density against overpotential (η), over one decade of current in the electrochemically active region, taken from the cyclic voltammograms. Linear Tafel plots between 0.1 and 1 $mA.cm^{-2}$ are shown in Figure 44. All linear fittings had a R^2 over 0.995 and were taken around the onset of the electrochemical reaction, and the Tafel slope is taken as the gradient of the Tafel line.
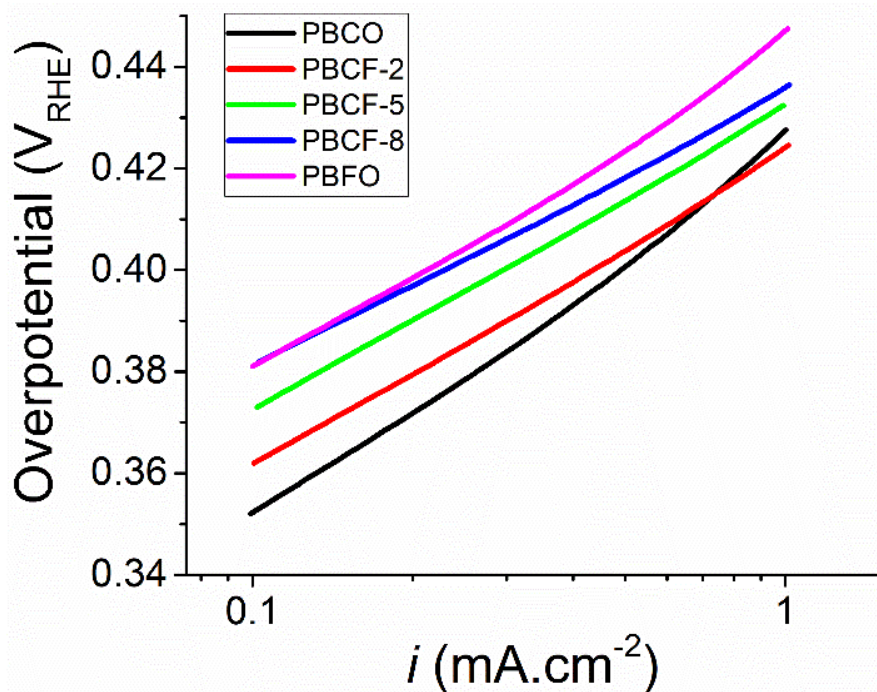
Figure 44 – Tafel Slopes for the PBCF double perovskite oxide electrocatalysts, taken over a range of 0.1 – 1 mA.cm^{-2}. All linear fitting had an R^2 value of more than 0.995.

The Tafel slopes for the material are in line with the hypothesis that the doped B site leads to increased OER electrocatalytic performance. A graph displaying the Tafel slope compared to iron dopant concentration (y) is shown in Figure 45. The Tafel slope values for the materials reduced from 74 mV.dec^{-1} for PBCO, falling to around 60 mV.dec^{-1} for the doped samples, and rising again to 66 mV.dec^{-1} for PBFO. These values are comparable to high performing similar materials from the literature, such as a study of $(Ln)BaCo_2O_6$ (Ln = Pr, Sm, Gd, and Ho) by Grimaud et al (2013),[191] and $SrNb_{0.1}Co_{0.7}Fe_{0.2}O_3$ (which has been shown to outperform IrO_2 and BSCF).[203] The intrinsic double perovskites PBCO and PBFO also have a considerably smaller Tafel slope than previously discussed $PrFeO_3$ (chapter 4), which is to be expected as PBCO and PBFO both showed activity in the CV tests unlike $PrFeO_3$. This displays further evidence of intrinsic double perovskite oxides being a superior crystal structure for OER electrocatalysts when compared to their single perovskite counterparts.
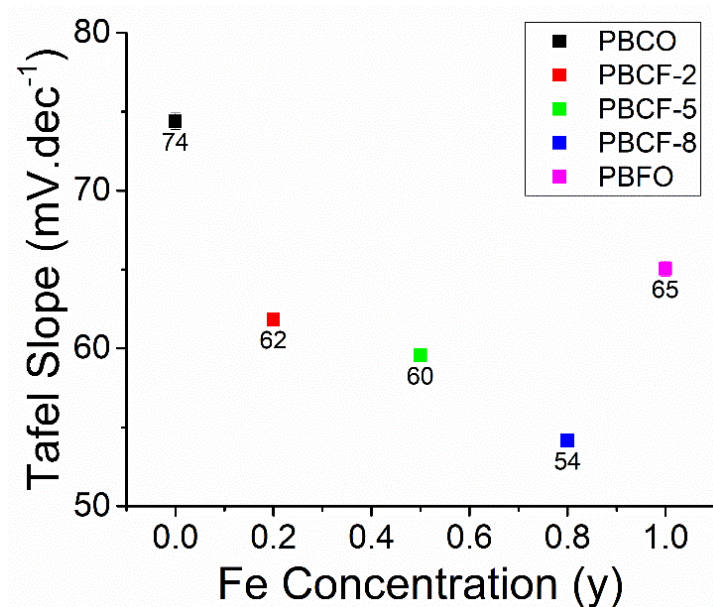
Figure 45 – Tafel slopes as a function of iron doping concentration in PBCF double perovskite oxide oxygen evolution electrocatalysts

As discussed, Tafel slopes are an incredibly useful metric for determining catalyst performance. In their 2015 paper, Shinagawa investigated the relationship between the Tafel slope and the microkinetics of various electrocatalytic reactions.[175] In the case of the oxygen evolution reaction, it was determined that the value for the Tafel slope will fall within a range depending on the limiting reaction step. As previously discussed, the oxygen evolution reaction consists of a 4-electron process (equations 4 to 7).

$$M + OH^- \leftrightarrow MOH + e^- \tag{4}$$

$$MOH + OH^- \leftrightarrow MO + H_2O + e^- \tag{5}$$

$$MO + OH^- \leftrightarrow MOO^- + H_2O \tag{6}$$

$$MOO^- \leftrightarrow M + O_2 + e^- \tag{7}$$
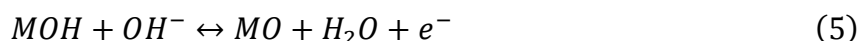
All Tafel slope values obtained from analysis of the PBCFO double perovskite oxide electrocatalysts fall within the same range, which is indicative of the rate limiting step being the formation of the peroxide ion on the transition metal surface (equation 6), or the desorption from the metal catalyst surface.[175] This is expected based on literature discussed in chapter 4. If the rate limiting step is the formation of peroxide (equation 6) then this will likely be due to complex

material interaction between the adsorbed oxygen species and the catalyst. However, both limiting reactions (equations 6 and 7) may be hypothetically easy to improve in a full alkaline electrolyser set up by having a constant flow of the electrolyte passed the electrode surface, which would help manually remove O_2 from the surface by reducing the double layer capacitance and could help to drive reaction 6 by removing water molecules which will help drive the reaction due to Le Chatelier's principle. However, this is speculative as it is out of the scope of this research project, but this may provide the basis of an interesting scale up based project in the future.

5.4 Conclusions and future work

Altering the crystal structure to form double perovskite oxides $PrBaCo_{2(1-y)}Fe_{2y}O_6$ lead to an overall increase in the performance of the material as an OER electrocatalyst when compared to single perovskite alternatives. This is especially evident when the performance of $PrFeO_3$ (PFO) single perovskite oxide is compared with $PrBaFe_2O_6$ (PBFO) double perovskite as within the same testing conditions there was little to no catalytic response from the PFO material whilst there was clear activity from the PBFO material. This simple addition also has the additional benefit of introducing a considerably cheaper element into the crystal structure, meaning that for every 2 praseodymium ions used in single perovskites, only 1 praseodymium and 1 barium ions are used in double perovskites. Valuations gathered from sigma show praseodymium to be around £4.50 per gram, compared to barium which is around £0.25 per gram. This adds further advantage to double perovskite structures from an industrial/commercial standpoint.

The presence of a mixed B-site containing varying stoichiometries of Co and Fe cations has also seen to improve the catalytic activity of the electrocatalysts. All 3 of the mixed site materials (PBCF-2, PBCF-5, and PBCF-8) showed noticeable improvements in current response, electrical conductivity, and Tafel slop when compared to the undoped PBCO and PBFO materials. The best performing double perovskite in this study was $PrBaCo_{1.6}Fe_{0.4}O_6$ (PBCF-2) in terms of current response and electrical resistance, and only a marginal difference in Tafel slope performance compared with the other doped materials. The current response of the PBCF-2 material is comparable with the strontium doped $Pr_{0.5}Sr_{0.5}FeO_3$ from chapter 4, which was slightly unexpected. However, the capacitance of the double perovskite material was one order of

magnitude lower than the single perovskite, which is a considerable material advantage during electrolyser start up.

The results in this chapter are in line with what was proposed in the initial hypothesis set out in the beginning of the chapter. The following chapter will explore how combining the concepts of both A and B site doping effects the material structure and the electrocatalytic performance as alkaline electrolyser anodes.

5.5 Appendix
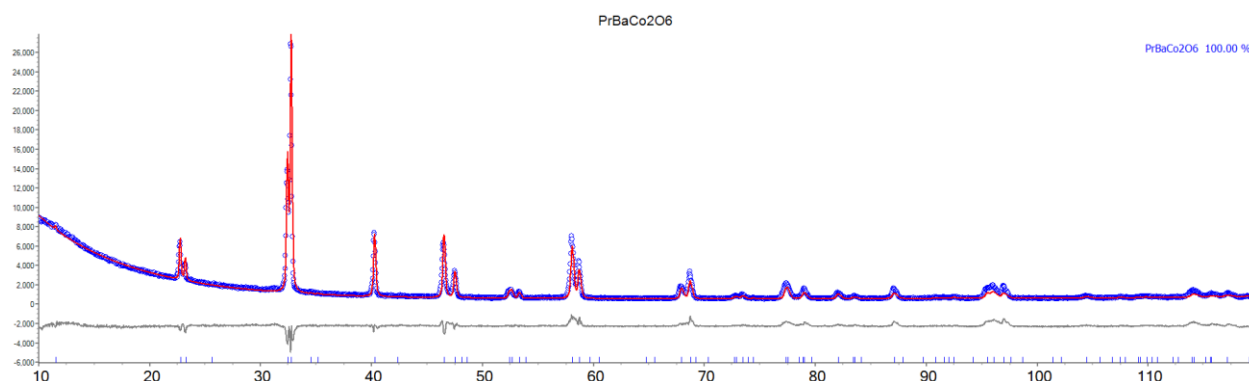
Figure 46 – PBCO
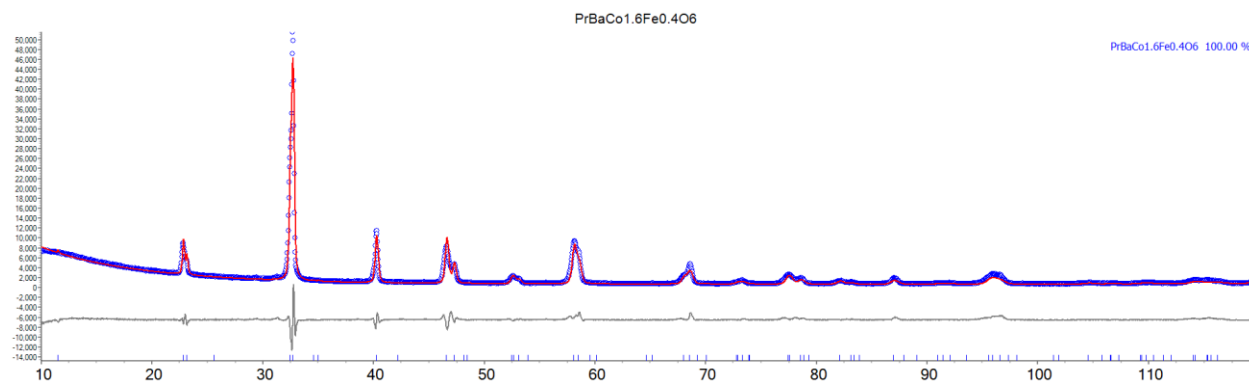
Figure 47 – PBCF-2
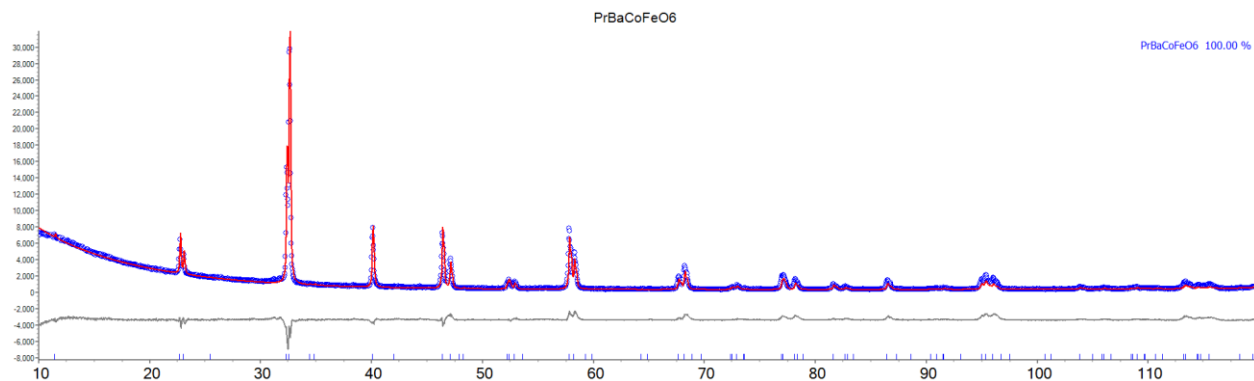
Figure 48 – PBCF-5
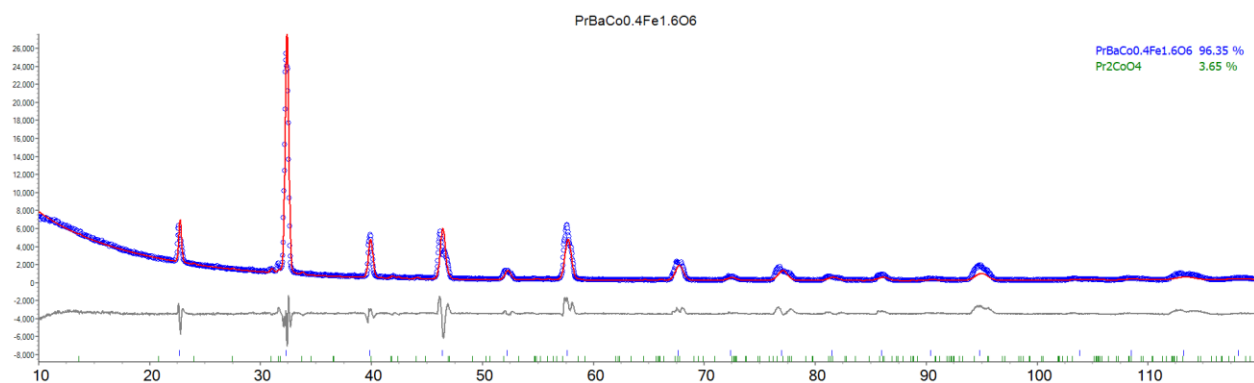
Figure 49 – PBCF-8
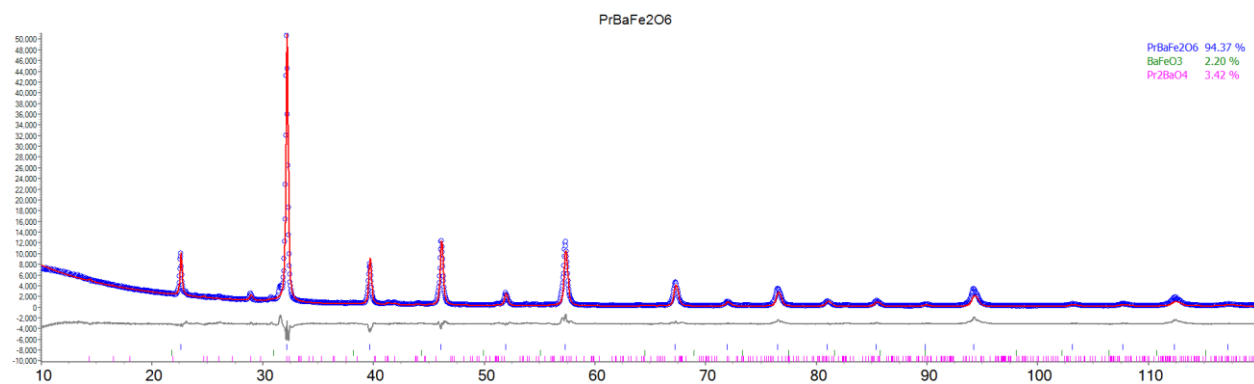
Figure 50 – PBFO

Chapter 6. Hydrothermal Synthesis of Single and Double Perovskite Oxide Oxygen Evolution Reaction Catalysts.

6.1 Introduction

Although the primary focus of this thesis is to determine the changes structural doping has on the electrocatalytic facilitation of the oxygen evolution reaction, a secondary line of investigation has also begun which could act as a springboard for further research projects. This, as mentioned in the introduction of this thesis, is the investigation of how altering the synthetic pathway of the perovskite oxide effects both the crystalline nature of the product, and the catalytic nature. The following short chapter outlines some of the ideas of this hypothesis and provides some preliminary results and discussions.

Altering the synthetic pathway for the perovskite oxide electrocatalysts is hypothesised to result in materials with poorer phase purity, but advantageous morphological properties such as increased surface area due to the formation of mesopores. A novel modification to the synthetic route of perovskite oxides is to expose the dissolved metal cations to a high-pressure environment using an acid digestion vessel. This vessel allows the use of lower temperature when compared to the dehydration step of the sol-gel process (around 190 °C compared to 300 °C for the sol-gel process), at the cost of a smaller sample size and higher equipment costs. The fundamental question which is to be answered when determining the long-term suitability of these hydrothermal based materials is that if the theorised improved performance from the morphological changes is worth the sacrifices of poorer and less reliable phase purity, higher equipment cost, and smaller batch sample size.

6.2 Results and Discussion

In order to test the hypothesis outlined for the hydrothermal materials, a synthesis method was required. There are many different synthesis routes reported in the literature which alter the morphology of the perovskite material grain to produce structures such as microcubes, yolk-shell, hollow-shell, various microspheres, nanowires, nanotubes, nano-powders to name but a few.[46, 49, 52, 132, 204-208] These differences in grain shape are modified through the use of different

ligand chemistries, hydrothermal temperature/pressure, and length of time spent in the hydrothermal vessel.

6.2.1 Material Synthesis

As discussed in the hypothesis of this chapter, the hydrothermal method is hypothesised to lead to a reduction in the phase purity, meaning that perovskite oxide will be accompanied by relatively high amounts of other material configurations. The exact mechanism behind the higher degree of impurity formation during hydrothermal method for perovskite oxides is not well understood, most likely because of the vast array of variables arising from starting materials, desired product properties, choice of mineraliser or polymerisation chemical, hydrothermal conditions, solvent choice, sintering conditions, pH and more lead a direct study of finding a one size fits all mechanism for this phenomenon extremely difficult, if not impossible. Several reasonable causes can be assumed to play a part in the formation of these multiple phases, such as purity of the starting materials, exposed facets of the starting crystalline materials, and differences in activation energy for formation of specific crystal species in high-pressure environments.

Synthesis techniques to remove impurity phases such as centrifuge and solvent wash have been implemented during the synthesis of the perovskite oxide materials with minimal effect, except for the sintering step after the hydrothermal material was removed and dried. This increased the phase purity considerably but was kept to a very short time (~2 hours) in order to maintain grain structure and to reduce potential synthesis upscale costs. However, any novelty that would be due to synthesis parameters would ultimately inconsequential if the material produced was inactive as an oxygen evolution reaction (OER) electrocatalyst in alkaline environments. Therefore, materials were synthesised using different chemicals and synthesis parameters and cyclic voltammetry measurements were taken of each material, and the results were compared to each other as well as the same material produced via sol-gel synthesis.

A material series of $PrFeO_3$ using different chelating agents and hydrothermal conditions was therefore synthesised and tested. The relevant synthesis procedure was also used for further hydrothermal synthesis of other perovskite oxides once a method had shown promise as an OER

electrocatalyst. A brief outline of the synthesis methodology and nomenclature (in bold) is as follows:

- **PFO_180_2hr:** 2g of KOH was added to 5 mL of 0.4 M B-site metal nitrate dissolved in deionised water with rapid stirring. To this, 5 mL of 0.4 M A-site metal nitrate was added and the mixture was allowed to stir. Finally, 4 g KOH was added to this solution and this was left for 15 minutes under vigorous stirring before being transferred to the autoclave. The autoclave was then sealed and placed in an oven, which was then heated to 180 °C. The vessel was allowed to sit at 180 °C for 24 hours before cooling to room temperature. Once cool, the solution was removed from the autoclave, separated using via centrifuge, washed with deionised water until a neutral pH was observed and allowed to dry. The resulting powder was then sintered in a muffle furnace at 800 °C for 2 hours with a heating rate of 2 °C min^{-1}. This synthesis method was adapted from literature for hydrothermal synthesis of similar materials.

- **PFO_210_2hr:** The same methodology for PFO_180_2hr, except the autoclave was heated to 210 °C for 24 hours rather than 180 °C.

- **PFO_PVP:** A stoichiometric molar ratio of A and B site metal nitrates was mixed in acetone and placed in an ultrasonic bath for 30 minutes. To this solution, deionised water was added along with K-30 polyvinylpyrrolidone (PVP) and KOH under vigorous stirring. This solution was transferred to an autoclave, heated to 180 °C for 24 hours, collected via centrifuge and deionised water and ethanol washing, and allowed to dry. This method was adapted from literature of similar materials using this surfactant. [206, 209, 210]

- **PFO_SG:** This is PrFeO$_3$ prepared by sol-gel method as described in the previous chapter. This was used as a baseline for comparison.

In order to determine which synthetic method to use going forward, cyclic voltammograms of the as synthesised materials were recorded using a 3-electrode set up. The conditions used in CV testing were the same as previously utilised, with a potential range of 1.30

− 1.80 V_{RHE} with a scan rate of 5 mV s^{-1} in a 0.1 M KOH electrolyte. The CV scans for all of the materials is shown in Figure 51.
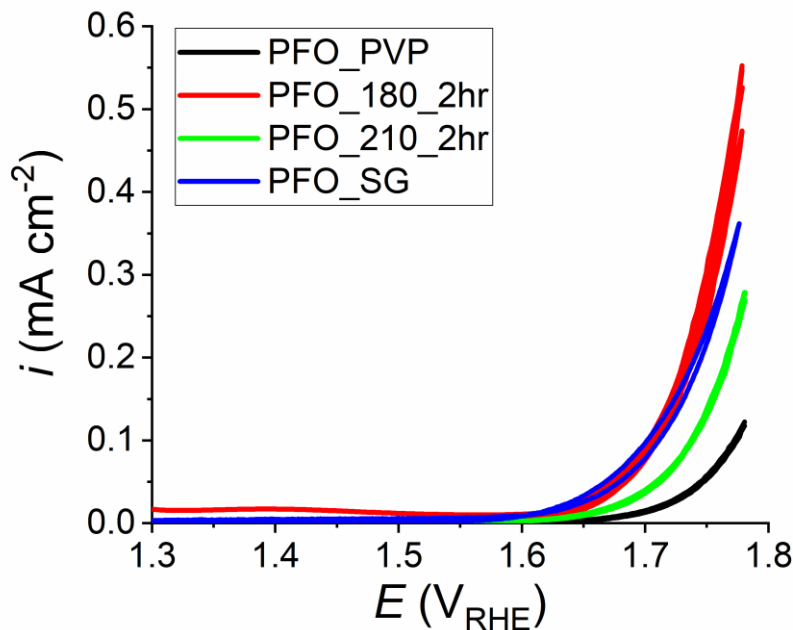
Figure 51 – Cyclic Voltammetry scans showing comparison between the OER electrocatalytic activities of the hydrothermal PrFeO₃ perovskite oxides.

It is clear to see from Figure 51 that the hydrothermal method that produces the most active material in this case is the KOH method with 180 °C hydrothermal temperature. This is the only material that out-performed the original sol-gel material, and was used as the basis for expansion into more complex stoichiometries. A more detailed investigation of the material performance is detailed in Table 9.

Table 9 – Performance comparison of the various PrFeO₃ hydrothermal synthesis methods

	Onset Potential (V_{RHE} at 0.1 mA cm^{-2})	Peak Current Density (mA cm^{-2})
PFO_PVP	*1.78*	*0.12*
PFO_180_2hr	*1.71*	*0.55*
PFO_210_2hr	*1.74*	*0.28*
PFO_SG	*1.71*	*0.36*

6.2.2 Phase Purity

After the synthesis method was decided upon, it was utilised to test some high performing stoichiometries that have been discussed during this thesis. In order to attempt to observe the effect of the different synthesis route has on a non-active catalyst material $PrFeO_3$ (PFO) was investigated. To analyse the effect the synthesis route had on the doped material, the best performing A and B site doped stoichiometries were chosen, these being the single perovskite oxide $Pr_{0.5}Sr_{0.5}FeO_3$ (PSFO), and the double perovskite oxide $PrBaCo_{1.6}Fe_{0.4}O_6$ (PBCF). These 3 materials were synthesised as described above for the 180_2hr synthesis route.

As mentioned in the hypothesis for this chapter, the hydrothermal method is expected to include a higher degree of impurity phases present when compared to other wet chemical methods such as sol-gel methods. This hypothesis is confirmed through powder X-Ray Diffraction patterns which indicates the presence of multiple phases present in all materials synthesised through hydrothermal method. Phase identification of the crystal phases present in the different hydrothermal provides confirmation of the different crystal phases, however a visual comparison between XRD patterns for the sol-gel (stylised as SG) and hydrothermal (stylised as HT) versions of the same material stoichiometry show a clear difference in the number of phases present. It appears from the diffraction patterns of the material series that increased complexity of the stoichiometry of the material leads to a higher degree of multiple phases being present, which follows logic due to the higher variety in types of atoms present allowing for more potential crystal configurations. Ambient temperature and pressure powder X-ray diffraction patterns of the hydrothermal material, as well as the related sol-gel stoichiometry are shown in Figure 52 to Figure 54.
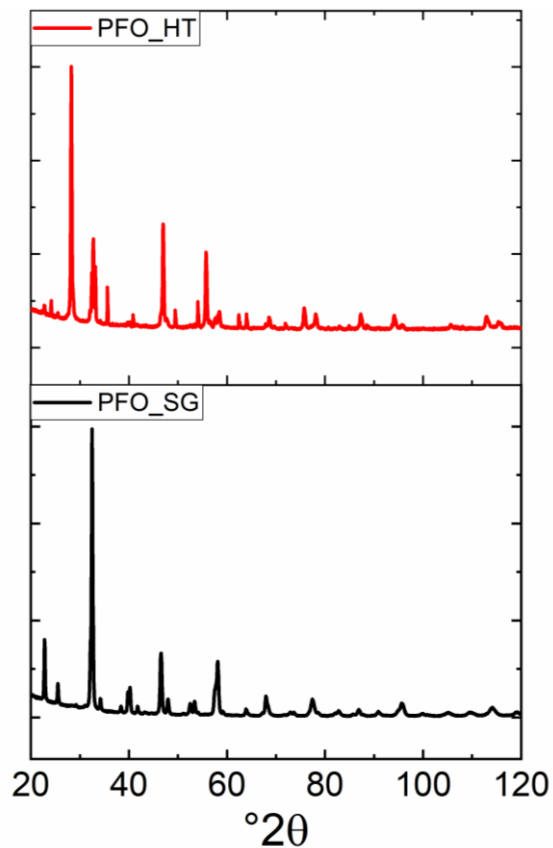
Figure 52 – XRD patterns for hydrothermal (HT) and sol-gel (SG) produced $PrFeO_3$ (PFO)
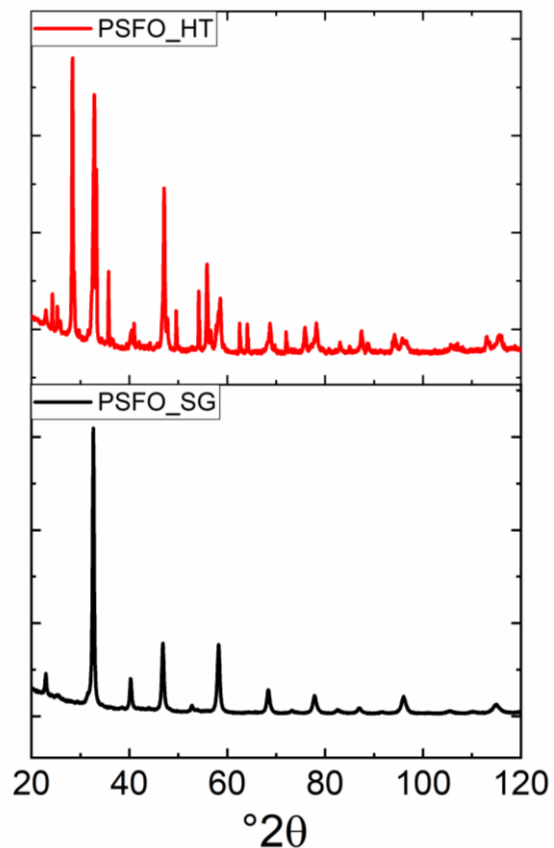
Figure 53 - XRD patterns for hydrothermal (HT) and sol-gel (SG) produced $Pr_{0.5}Sr_{0.5}FeO_3$ (PSFO)
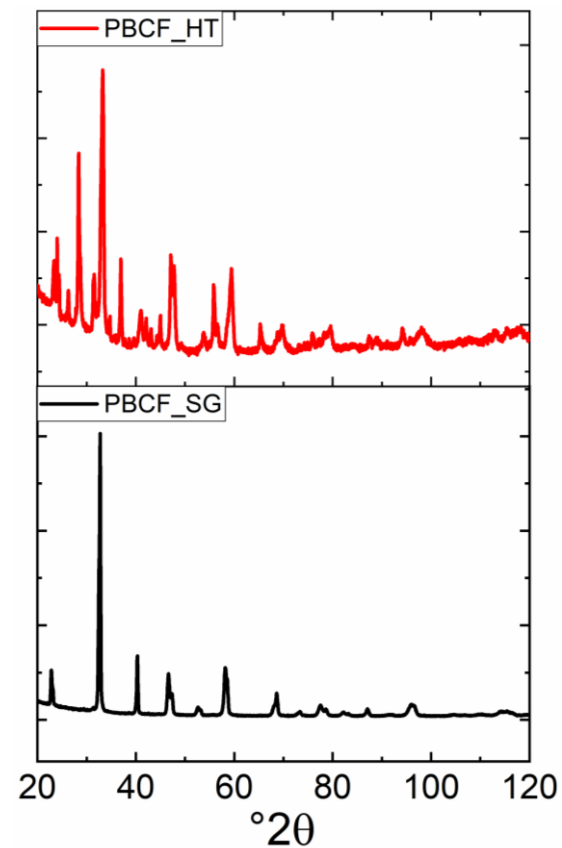
Figure 54 - XRD patterns for hydrothermal (HT) and sol-gel (SG) produced $PrFeO_3$ $PrBaCo_{1.6}Fe_{0.4}O_6$ (PBCF)

The impurity phases of the material were identified throughout the materials as a mix of desired perovskite oxide phase, metal oxides, and stoichiometric configurations such as spinel and Ruddlesden-Popper phases. The presence of impurity phase in the material is not ideal which indicates future optimisation of the synthesis method is required. As previously mentioned, there are multiple factors that can affect the crystal phase homogeneity of the final product, it is difficult to say with certainty what procedural changes will be the most effective in correcting this issue. However, the presence of the desired perovskite oxide phase in all 3 samples is a positive sign, and as the starting materials were almost identical between the sol-gel and hydrothermal synthesis procedures, a comparison between the electrochemical performance of the electrocatalysts can be investigated.

6.3 Electrocatalytic Activity – Sol-gel vs Hydrothermal

The catalytic activity of the hydrothermal material and the relevant sol-gel counterpart were tested via cyclic voltammetry under the same conditions as previously described in this thesis. Briefly, the catalyst material was suspended in an ink and drop cast onto a gold working electrode, amounting to a loading of ~153 µg cm^{-2}_{Geo}. The working electrode was then submerged in an electrolyte of 0.1 M KOH, and connect to a 3-cell set up with a Pt mesh counter electrode and a Au/AuCl reference electrode. Cyclic voltammetry scans were taken between 1.30 and 1.80 V_{RHE} at a scan rate of 5 mV s^{-1}. Cyclic voltammograms showing comparison between sol-gel (SG) and hydrothermal (HT) produced materials for $PrFeO_3$ (PFO_SG/HT), $Pr_{0.5}Sr_{0.5}FeO_3$ (PSFO_SG/HT), and $PrBaCo_{1.6}Fe_{0.4}O_6$ (PBCF_SG/HT) are shown in Figure 55, Figure 56, and Figure 57 respectfully.
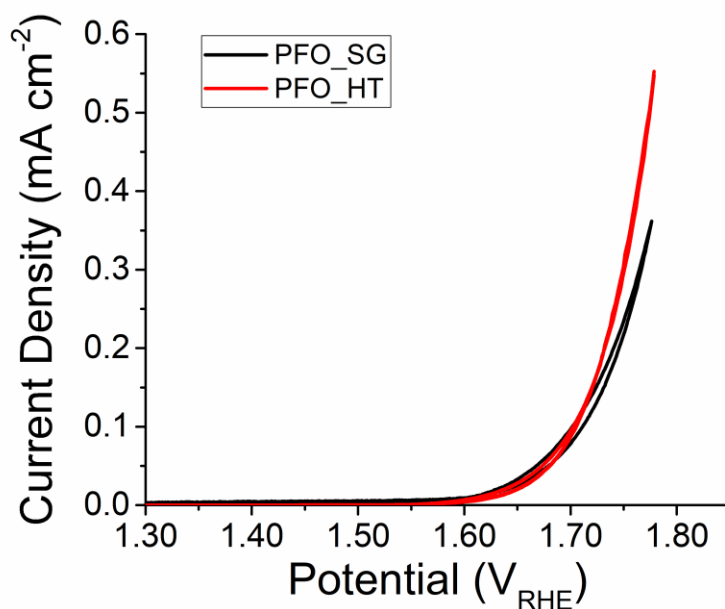
Figure 55 – Cyclic Voltammograms of PFO single perovskite oxide electrocatalyst materials synthesised through both hydrothermal (HT) and sol-gel (SG) routes. Red line represents the hydrothermal materials, and black line represents the sol-gel material. It is clear that the hydrothermal material is the highest performing catalyst.
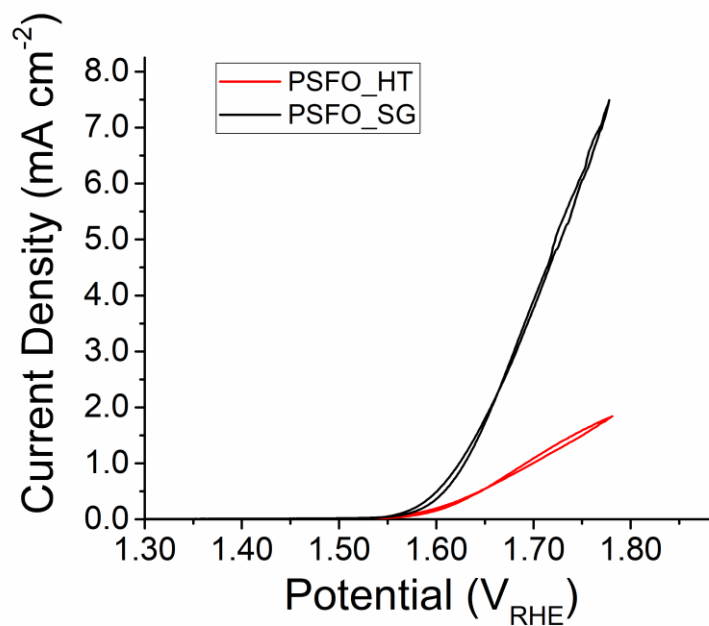
Figure 56 – Cyclic Voltammograms of PSFO doped single perovskite oxide electrocatalyst materials synthesised through both hydrothermal (HT) and sol-gel (SG) routes. Red line represents the hydrothermal materials, and black line represents the sol-gel material. It is clear that the sol-gel material is the highest performing catalyst.
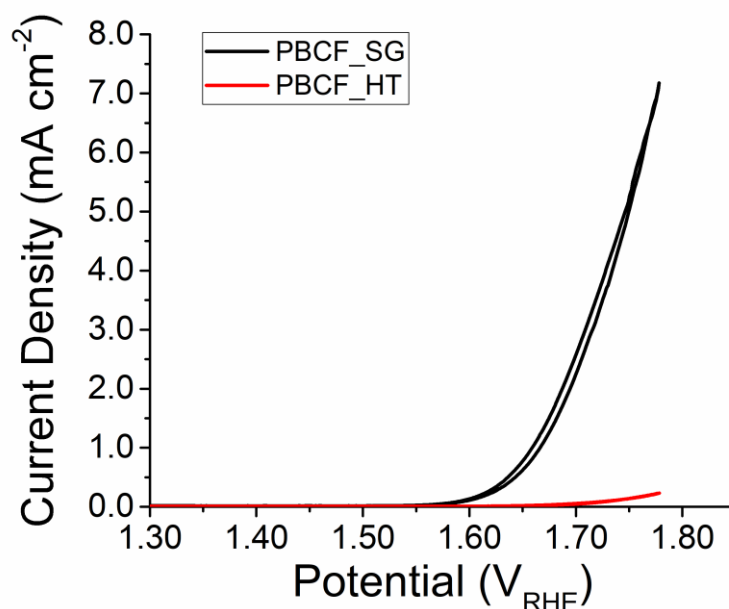
Figure 57 – Cyclic Voltammograms of PBCF double perovskite oxide electrocatalyst materials synthesised through both hydrothermal (HT) and sol-gel (SG) routes. Red line represents the hydrothermal materials, and black line represents the sol-gel material. It is clear that the sol-gel material is the highest performing catalyst.

Building on the initial PFO study (Figure 51), Figure 55 shows that the material synthesised by hydrothermal method out-performs the sol-gel material by a margin of around 50%. Unfortunately, this does not extend to the more complex stoichiometry PSFO and PBCF materials. The hydrothermal material it utterly dwarfed by the sol-gel material in both the PSFO and PBCF electrocatalysts. There are many potential factors that could be the reason for this massive underperformance of the hydrothermal material, however it is almost impossible to make a reasonable assumption based on this data due to the poor phase purity of the hydrothermal materials. The perovskite phase is an effective electrocatalyst for the oxygen evolution reaction in alkaline conditions as demonstrated in part by the contents of this thesis, so by this metric any other phase will lower the effectiveness of the catalyst material.

The issues attributed to the phase impurity could be rectified in two ways. Firstly, each individual phase present in the material could be synthesised and tested in order to normalise the results displayed in this section. This would require the quantification of each material phase present in the material powder by adding a known %wt of a standard material such as LaB_6 or Cristobalite and calculating the %wt of the material phases through refinement of the powder X-ray diffraction data. However, this would be redundant outside of the purpose of material

characterisation and understanding the synthetic reaction pathway, as this will not remove the impurity phase, nor stop it from forming. In fact, even if this was the case it would leave the methodology highly inefficient due to poor conversion of raw materials on an already small yield due to the nature of the sealed reaction vessel. In reality a systematic investigation into changing synthetic conditions such as pH, autoclave retention time, and choice of mineraliser/polymer chemical would be required in order to grow perovskite crystals with minimum amounts of impurity phase. This is outside of the scope of this thesis but presents an interesting point to build upon for developing single phase electrocatalysts whilst maintaining the novel morphology that arises from hydrothermal method.

6.4 Scanning Electron Microscopy (SEM) Images

The primary interest in using the hydrothermal vessel for the synthesis of perovskite oxides is that the products of this synthesis offer novel and interesting particle morphology that is either extremely difficult, or impossible to replicate by other means. In fact, when designing a catalyst material this is an important factor, as the benefits arising from the novel morphology must outweigh the relatively severe drawbacks of the hydrothermal method, predominately small product yield and expensive synthesis equipment. As discussed earlier in this thesis, there are a multitude of particle morphologies that can been synthesised through hydrothermal method, and those which use KOH as a mineraliser have been observed to form grains with visible facets often resembling a cuboid shape.[204] Having clear facets exposing the reactant species adsorption sites could be extremely useful for catalytic materials, as if the orientation of the grains could be controlled then this would allow for maximum utility of the catalytically active sites.

To examine the shape of the crystal grain, images of both the hydrothermal and the sol-gel material were taken using a Scanning Electron Microscope (SEM). Two main observations can be made from a visual comparison of the images for both the hydrothermal and sol-gel materials. As expected, the sol-gel material (Figure 58) shows very little uniformity in the particle shape and size. The best description for the sol-gel material would be a disordered gathering of flakes or shavings with no size or distribution pattern. This is a different story with the hydrothermal synthesised materials (Figure 59 to Figure 61) which from spherical particles with porous surfaces, to dodecahedron shaped particles with defined surface facets. Simply from the scale bar present

113

in each of the SEM images it can be deduced that the hydrothermal particles are considerably smaller (1 – 2 microns) than the sol-gel material (20 + microns). This smaller particle size provides a hypothetical advantage due to the much higher state of division leading to considerably more availability of active catalytic sites in the same geographic space.
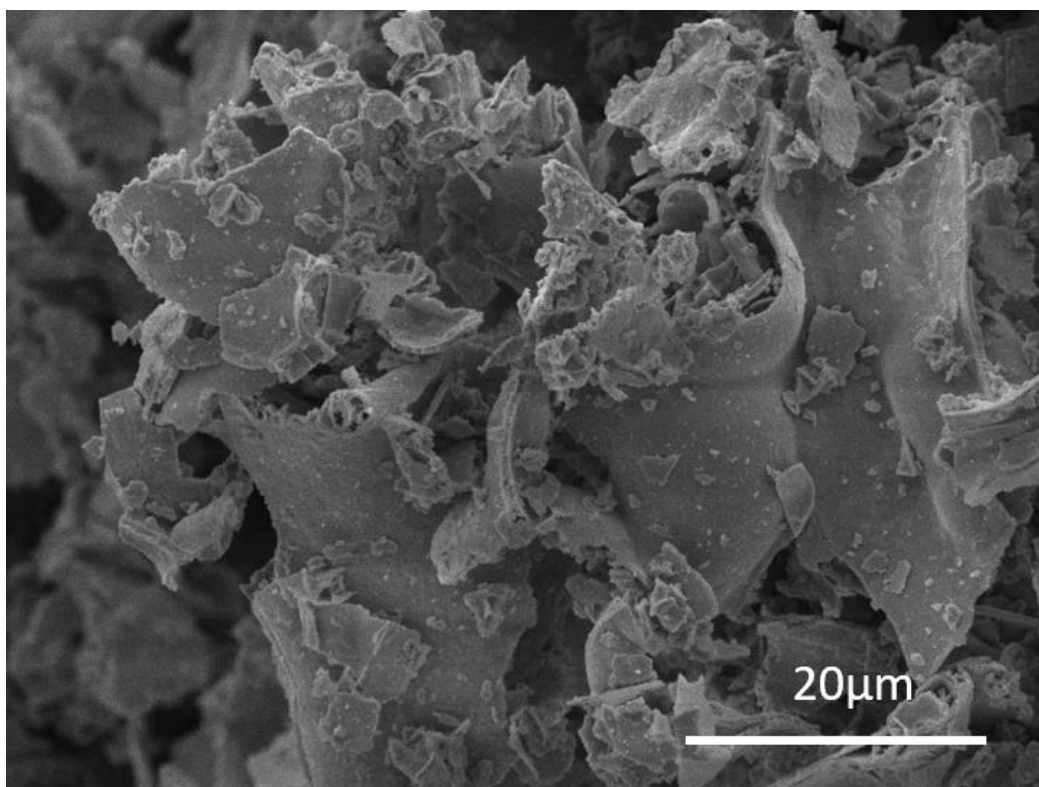
Figure 58 – SEM image of perovskite oxide electrocatalyst produced through sol-gel method using citric acid as a chelating agent. General grain morphology indicates a lack of uniformity in both shape and size of the particles. However, the crystal grain is considerably larger than that of the hydrothermal materials.
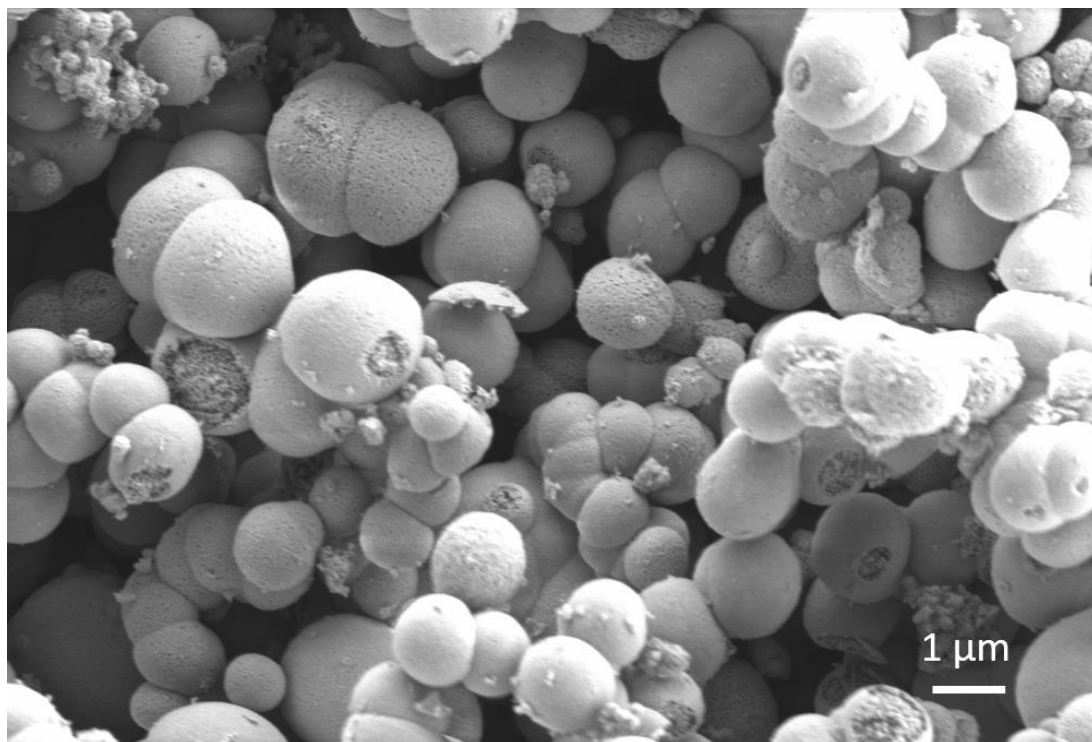
Figure 59 – SEM images of PSFO_HT synthesised through hydrothermal method using KOH as a mineraliser and hydrothermal conditions of 180 °C for 24 hours. General grain morphology indicates porous spherical material grain with a moderately uniform shape and size. Particles are considerably smaller in size than for the sol-gel synthesised perovskite oxide.
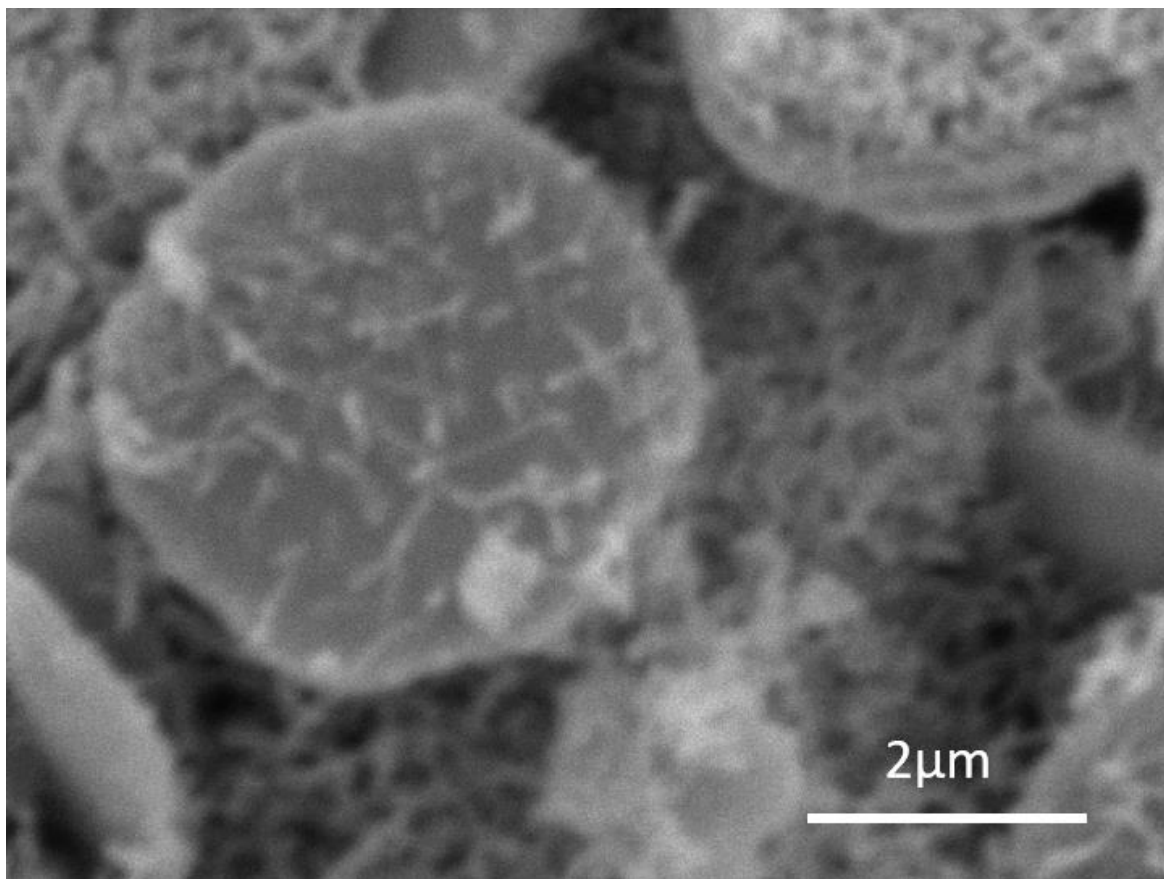
Figure 60 – SEM images of PFO_HT synthesised through hydrothermal method using KOH as a mineraliser and hydrothermal conditions of 180 °C for 24 hours. General grain morphology indicates spherical material grain with a moderately uniform shape and size. However, there appears to be less pores present on the surface of the spheres, although this may be down to a lower resolution image. Particles are considerably smaller in size than for the sol-gel synthesised perovskite oxide.
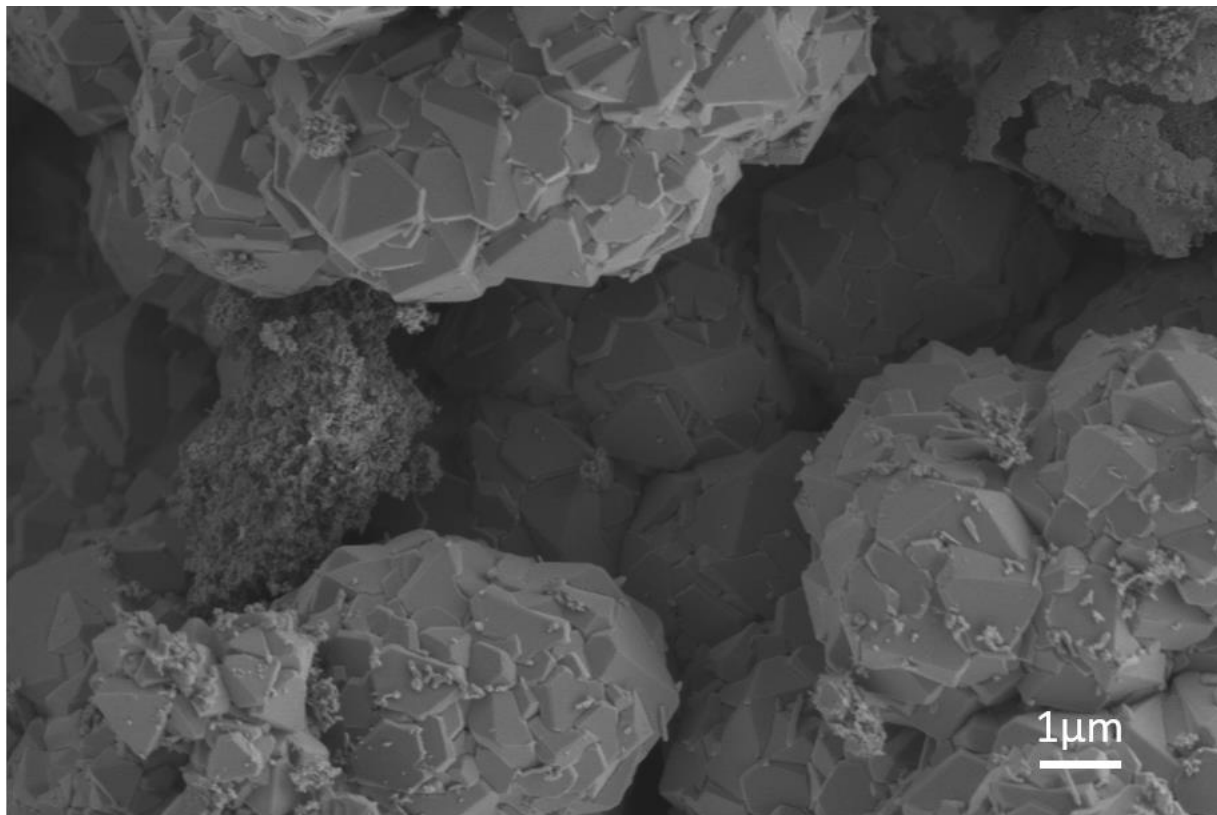
Figure 61 – SEM images of PBCF_HT synthesised through hydrothermal method using KOH as a mineraliser and hydrothermal conditions of 180 °C for 24 hours. General grain morphology indicates a dodecahedron shaped material grain with a moderately uniform shape and size, with clearer definition of surface facets. Particles are considerably smaller in size than for the sol-gel synthesised perovskite oxide.

6.5 Conclusions and Future Work

The results presented in this mini chapter show promise for a future project focussing on increasing catalytic activity through changes to the morphology and porosity of the particles. It has been clearly demonstrated that novel and interesting particle morphology can be attained through use of an autoclave during the synthesis of perovskite oxide materials. This novel morphology can hypothetically increase the electrochemical performance of the materials with regards to alkaline oxygen evolution due to increased state of division, especially with a layered or hollow-shell morphology. This has been somewhat demonstrated by the results presented in this chapter, as the performance of the intrinsic $PrFeO_3$ single perovskite oxide was improved by various synthesis parameter modifications, especially the use of KOH and an autoclave temperature of 180 °C and a retention time of 24 hours. This proof of concept is highly encouraging and should be investigated further outside the scope of this thesis.

However, any changes (positive or negative) in the electrochemical activity of the electrocatalysts between different synthesis methods (sol-gel and hydrothermal) is clouded by the issue of high levels of phase impurity present in the hydrothermal material. It is impossible to determine if the positive or negative effects with regards to electrocatalytic activity are related to the particle size and morphology when high levels of other, potentially active or inactive, phases are present. Optimising the synthesis method to remove the vast majority of these impurity phases whilst retaining regimented particle morphology is the first major obstacle to overcome in order to fully understand the effect of the different synthetic methods. This challenge becomes considerably more difficult when attempting to synthesise non-stoichiometric materials, which is necessary as these, as demonstrated through the results in this thesis and in the wider literature, consistently outperform intrinsic non-doped perovskite oxides. This additional challenge is hypothesised to be due to the addition of as more diverse range of metal cations, which will readily form species with lower activation energies than their perovskite oxide counterpart. As mentioned in this chapter, changes to the starting materials and hydrothermal retention time and temperature will be the most effective in facilitating this change.

Chapter 7. Loading of Sr^{2+} ions into PBCF crystal lattices with varying Co/Fe stoichiometries to create $Pr(Ba_{0.5}Sr_{0.5})Co_{2(1-y')}Fe_{2y'}O_6$ electrocatalysts for the oxygen evolution reaction (OER).

7.1 Introduction

The previous chapter discussed the effect altering the stoichiometric ratio of Co and Fe cations in $PrBaCo_{(2-y)}Fe_{2y}O_6$ (PBCF) double perovskite oxides has on the electrocatalytic facilitation of the oxygen evolution reaction (OER) in alkaline electrolytes. From the results presented, it can be seen that a Fe/Co stoichiometry of y = 0.2 ($PrBaCo_{1.6}Fe_{0.4}O_6$) provided the highest performance in terms of current density and electrical resistance at 1.70 V_{RHE}, and all of the mixed B site materials (y = 0.2, 0.5, and 0.8) outperformed the Co and Fe saturated materials. This is hypothesised to be due to the mixed electron valency throughout the material, as the filling of the transition metal 3d e_g orbital is a crucial activity descriptor for transition metal based oxygen evolution electrocatalysts.[41] The performance of the double perovskite material was compared with single perovskite materials as discussed in chapter 4. The $PrBaCo_{1.6}Fe_{0.4}O_6$ (y = 0.2) was seen to have a comparable Tafel slope and current response to the highest performing single perovskite material $Pr_{0.5}Sr_{0.5}FeO_3$ (x = 0.5)[127], whilst out-performing the single perovskite in terms of electrical capacitance.

In this chapter the concepts of the 2 previous chapters are combined by adding strontium into the double perovskite lattice, and analysing the effect this has on mixed B site stoichiometries by synthesising $Pr(Ba_{0.5}Sr_{0.5})Co_{2(1-y')}Fe_{2y'}O_6$, or PBSCF, where y' = 0, 0.2, 0.5, 0.8, 1.0. The theoretical reasoning behind replacing barium with strontium is that higher oxidation states of the B site ion, especially Co^{4+} will be more stable with the strontium addition. On initial conception this may seem counterintuitive, as the Ba^{2+} ion is more electropositive than Sr^{2+}, so higher transition metal oxidation states should theoretically be stabilised by Ba^{2+}. However, due to the A and A' site layer stacking in double perovskite oxide structures the distance between the transition metal B site ion and the Ba^{2+} ion is too large. Strontium ions on the other hand do not readily form double perovskite structures due to the smaller ionic radii. This addition causes disruption in the layers of the double perovskite oxide structure which reduces the steric issues between the Ba^{2+} and the transition metal, allowing for increased stability of higher B site oxidation states. Alongside

the theoretical stabilisation of higher oxidation states such as Co^{4+} by the introduction of Sr^{+2} into the crystal lattice, the addition of strontium ions leads to a higher oxygen content in the material, which in turn leads to a high electrical conductivity.[211]

The electrical conductivity of double perovskite oxides is often limited by the nature of the crystal structure, as the distance between the trivalent rare-earth ion and the divalent alkaline-earth ion can result in lower oxygen content values for the material.[212] This is intrinsic of the double perovskite oxide structure as the 4f electrons of the lanthanide atom are incredibly unlikely to exist in the outer regions of the atoms. This means that effects to the bonding environment due to orbital geometry arising from overlap between the lanthanide ion and incoming species is non-existent, and so steric factors are the driving force behind the bonding environment.[213] As previously discussed however, the addition of Sr^{2+} into the crystal structure will lead to perturbations in the layers due to the smaller ionic radii of the Sr^{2+} ion compared to Ba^{2+} ions, thus improving the electrical performance of the material.[214] However, as the strontium (and therefore oxygen) content increases, the ions are less likely to order along the c crystallographic axis.[190] Therefore, a balance must be maintained between improved catalytic facilitation and phase purity. In line with results gathered from chapter 4, PBCF double perovskites were first doped with 50 wt% Sr^{2+} creating $Pr(Ba_{0.5}Sr_{0.5})Co_{2(1-y')}Fe_{2y'}O_6$ (PBSCF B Site). The 50 wt% doping concentration is consistent with what has reported in literature.[215-218] Although $Pr(Ba_{0.5}Sr_{0.5})Co_{2(1-y')}Fe_{2y'}O_6$ and similar materials have been discussed within the literature, the primary focus has been as an electrocatalyst in solid oxide fuel cells (SOFC), which presents an opportunity for novel discovery by using this material in an alkaline electrolyser system.[40, 218]

- Introducing 50 wt% Sr^{2+} into PBCF double perovskite oxides will increase the performance of the electrocatalyst, this will primarily be through improvements to the electrical resistance.
- Mixed B site stoichiometries will out-perform Co or Fe saturated materials, but Sr^{2+} addition will improve performance, primarily through electrical conductivity.
- Phase purity will decrease with increased Sr^{2+} content due to reduced ordering.
- Varying strontium content will lead to a volcano like relationship due to lack of phase purity with increased Sr^{2+} doping.

7.2 Material Characterisation

7.2.1 The Pseudo-cubic Unit Cell

In order to ensure a fair comparison between Sr^{2+} containing and Sr^{2+} free materials, the same stoichiometric ratio of B site cations (y' = 0, 0.5, 0.5, 0.8, 1) and synthesis conditions were used in the production for the $Pr(Ba_{0.5}Sr_{0.5})Co_{2(1-y')}Fe_{2y'}O_6$ (PBSCF B Site) perovskite oxides. These were denoted as PBSCO, PBSCF-2, PBSCF-5, PBSCF-8, and PBSFO for y' = 0, 0.2, 0.5, 0.8, and 1 respectively. As before, the materials were characterized by ambient temperature powder X-Ray Diffraction (XRD), and the resulting diffraction patterns were fit using Rietveld method of least squares.[114] The PBSCF series indicate a phase transition trend as Fe concentration increases, where the symmetry of the material series for y' = ≤0.5 is tetragonal, specifically *P4/mmm* (Z = 2) (space group number 123), which transitions to cubic, specifically *Pm$\overline{3}$m* (Z = 1) (space group number 221), for y' = ≥0.8. This is in line with the series found in the PBCF ($PrBaCo_{2(1-y)}Fe_{2y}O_6$) double perovskites, and is consistent with what has been reported in the literature.[217]

As described in previous chapters (chapter 5), the pseudo-cubic unit cell is a useful parameter when comparing lattice properties such as lattice parameters or the crystal volume of a material series which has a phase transition to a different space group. The pseudo-cubic lattice parameters are calculated using equation 1.[219]

$$a_p \approx \frac{a_o}{\sqrt{2}} \approx \frac{b_o}{\sqrt{2}} \approx \frac{c_o}{2} \qquad (1)$$

Where a_p is the pseudo-cubic unit cell parameter (individual lattice parameters denoted as a', b', and c'), and a_o, b_o, c_o are the lattice parameters from the tetragonal fitting. The crystal volume is normalised with respect to the formula unit (Z), so the normalised volume for the tetragonal materials (stylized as Vol') is the half of the refined volume of the *P4/mmm*, as Z = 2 for *P4/mmm* and Z = 1 for *Pm$\overline{3}$m.* Lattice parameters, crystal volume, and their pseudo-cubic representations from the PBSCF perovskite oxides are listed inTable 10.

Table 10 – Unit cell parameters for $Pr(Ba_{0.5}Sr_{0.5})Co_{2(1-y')}Fe_{2y'}O_6$, with errors in parenthesis.

Fe (y)	Space Group	Lattice Parameter (Å)			Vol (Å³)	Vol' (Å³)
		a = b	c	c'		
0	$P4/mmm$	3.898(1)	7.796(4)	3.898(2)	118.44(9)	59.22(5)
0.2	$P4/mmm$	3.8690(3)	7.7515(9)	3.8757(4)	116.03(2)	58.02(1)
0.5	$P4/mmm$	3.8562(2)	7.7285(7)	3.8642(4)	114.93(2)	57.46(1)
0.8	$Pm\overline{3}m$	a = b = c = 3.8907(1)			58.87(2)	
1.0	$Pm\overline{3}m$	a = b = c = 3.8531(1)			57.21(5)	

Table 10 shows a general trend of iron concentration being inversely proportional to the volume of the crystal lattice. There is a clear anomaly in the PBSCF-8 material which will be discussed further in the next section.

7.2.2 Phase Purity

Powder diffraction patterns for the PBSCF B site mixed material series are shown in Figure 62. Powder diffraction patterns were taken under ambient temperature and pressure, and confirm the presence of the anticipated double perovskite phase, as well as some impurity phases which were hypothesised to be present due to the perturbation of the crystal lattice by the difference in the ionic radii between Ba^{+2} and Sr^{+2}.[154] The specific phase concentrations relative to mass are shown in the refined diffraction patterns (Figure 69 – Figure 73).

Interestingly the highest concentration of phase impurity in the $PrBaCo_{2(1-y)}Fe_{2y}O_6$ (PBCF) material series was found in the iron rich (y = 0.8 and 1) stoichiometries. Whereas, for the PBSCF B Site series by far the highest concentration of phase impurities exists within the cobalt saturated material $PrBa_{0.5}Sr_{0.5}Co_2O_6$ (y' = 0), as shown by the large peak around 28 °θ in the y' = 0 diffraction pattern shown in Figure 62. The refined diffraction pattern for the cobalt saturated material (Figure 69) shows that the $PrBa_{0.5}Sr_{0.5}Co_2O_6$ double perovskite phase in $P4/mmm$ tetragonal configuration makes up around 80 %wt of the sample, alongside *circa* 18 %wt of the spinel $(Ba_{0.5}Sr_{0.5})Co_2O_4$ phase in orthorhombic *Cmc21* configuration, and *circa* 2% of the n = 1 Ruddlesden-Popper phase Pr_2CoO_4 in orthorhombic *Bmab* configuration. The refined powder diffraction patterns (Figure 69 – Figure 73) shows that the highest intensity impurity phase Bragg

reflection at around 28°θ is from the $(Ba_{0.5}Sr_{0.5})Co_2O_4$ spinel phase, and the Ruddlesden-Popper is the primary reason for the small peak just before the main perovskite peak (which is the case for the rest of the material series).
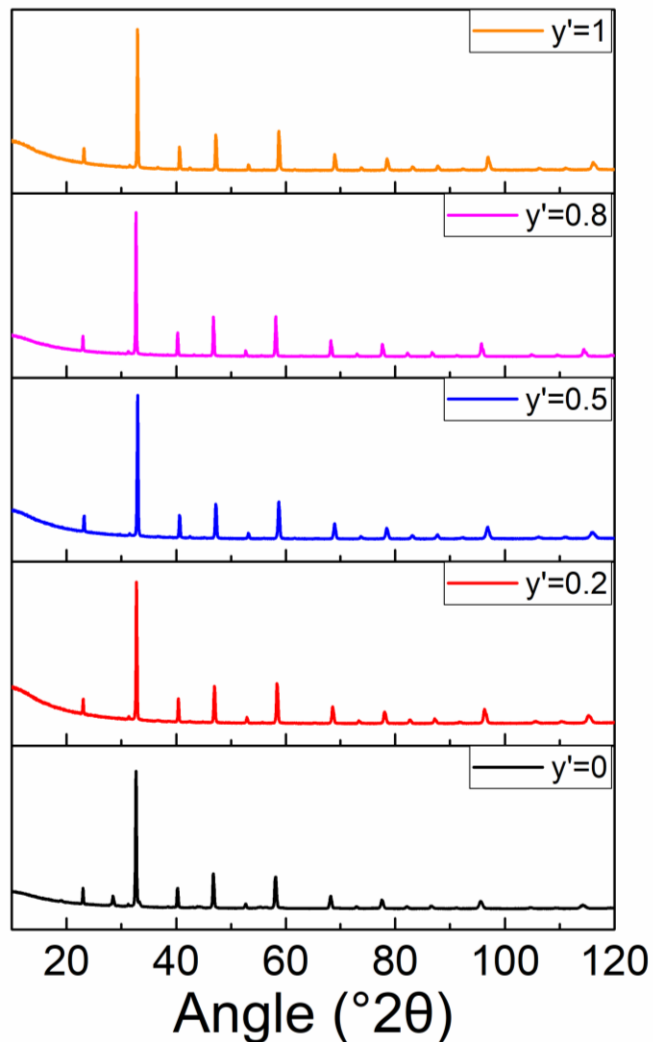
Figure 62 – Ambient temperature and pressure powder X-Ray Diffraction (XRD) patterns of the Pr(Ba$_{0.5}$Sr$_{0.5}$)Co$_{2(1-y')}$Fe$_{2y'}$O$_{6-\delta}$ (PBSCF B-site) double perovskite oxides, showing Bragg reflection intensity as a function of the diffraction angle.

The mechanism behind the lower phase purity in the cobalt saturated material is unknown. However, throughout multiple repeated synthesis attempts this phase purity persistently observed. This indicates that the formation energy for pure $Pr(Ba_{0.5}Sr_{0.5})Co_2O_6$ double perovskite phase is higher than the synthesis route could provide. It could be hypothesised that this is related to the stabilisation of higher cobalt ion oxidation states by the presence of Sr^{+2} ions as discussed above, so the probability of other cobalt containing complexes forming when there is a saturation of cobalt ions is higher than when mixed Co/Fe ions are present. However, although

this is an interesting phenomenon which was consistent across repeated samples, the purpose of this study is to investigate how the addition of 50 %$_{wt}$ Sr^{2+} ions into the PBCF lattice changes crystal structure and the electrocatalytic facilitation of the oxygen evolution reaction, rather than ensuring homogenous phase purity. The synthesis parameters such as the sintering time and/or temperature could be optimised to ensure phase purity, but that would introduce more variables into the material comparison, which could cloud the actual results. It is for these reasons that this is deemed to be outside the scope of this research project.

7.2.3 Lattice Parameters and Crystal Volume

As discussed, the lattice parameters and volume shown in Table 6 indicate an anomalous result for y' = 0.8, as the volume and lattice parameters are much larger than the apparent trend would suggest. The results were consistent for repeated synthesis of y' = 0.8, suggesting the data is correct. Anomalies in powder X-Ray Diffraction data could be due to poor refinements, so this was investigated as a potential route cause. However, this can be ruled out before having to analyse fitting statistics by analysing the powder diffraction patterns. Figure 63 shows a much smaller 2θ range of Figure 62, highlighting the position of the (110) Bragg reflection peak. It can be seen that as for samples where y' ≤ 0.5, the peak is shifting towards a higher 2θ value, but then for y' = 0.8 the peak shifts towards a lower 2θ value.
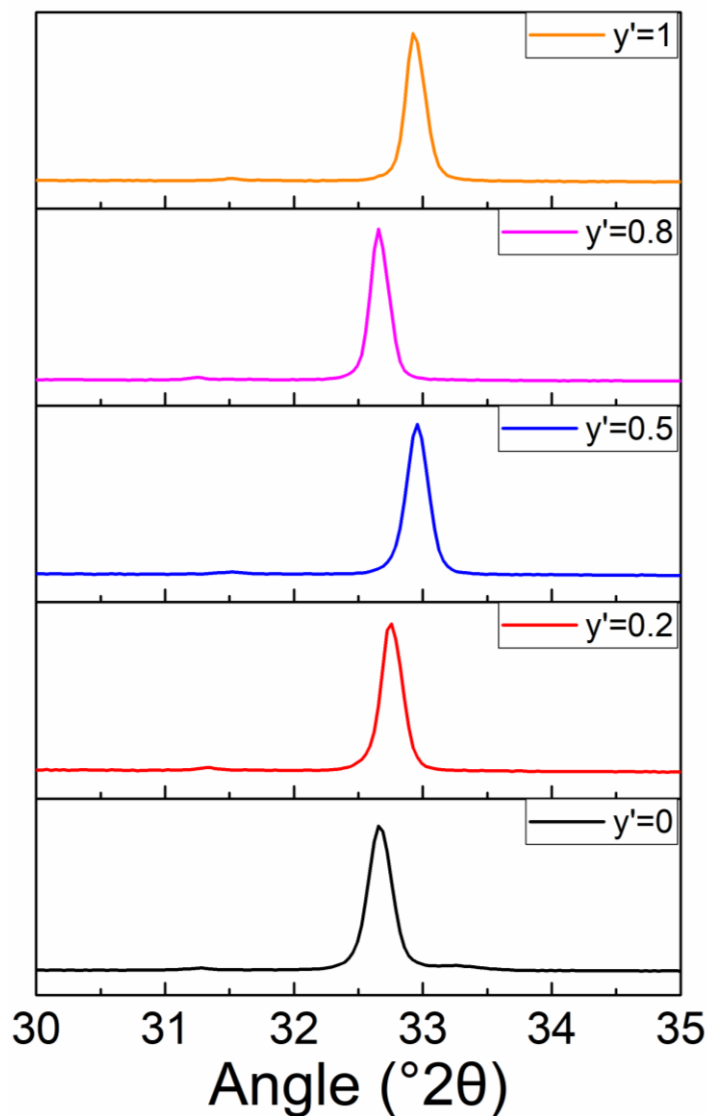
Figure 63 – Powder XRD patterns of the PBSCF B site perovskite, highlighting the shift in the diffraction angle on the (110) Bragg Reflection. All data was gathered at ambient temperature and pressure

This shift towards a lower Bragg angle is indicative of larger spacing between layers in the crystal structure, as rearranging Bragg's law (equation 2) to be a function of spacing (equation 3) shows how Bragg angle and layer spacing are inversely correlated.

$$n\lambda = 2d_{hkl} \sin\theta \qquad (2)$$

Rearranged and assuming n = 1:

$$\theta = \sin^{-1}\left(\frac{\lambda}{2d_{hkl}}\right) \qquad (3)$$

125

Where λ is the wavelength of the incident X-Ray beam, d_{hkl} is the interplanar lattice spacing, and θ is the Bragg angle. Therefore, it is clear through equation 3 that as in distance between lattice planes increases, the Bragg angle for a specific reflection will decrease. As the Bragg peaks for the y' = 0.8 sample has clearly shifted to a lower Bragg angle (Figure 63), it is clear that the anomalous result has not come from poor data refinement, rather the increase in lattice parameters and unit cell volume appear to be a characteristic of this particular stoichiometry.

A graphical representation of the normalised lattice parameters and crystal volume from Table 6 is displayed in Figure 64. As discussed the $Pr(Ba_{0.5}Sr_{0.5})Co_{0.4}Fe_{1.6}O_6$ (y' = 0.8) material is an outlier to the apparent trend of increasing concentrations of y' leading low lower lattice parameters. This result was consistent throughout repeat synthesis and analysis. The exact specifics of why this specific stoichiometry leads to these anomalous results is unknown.
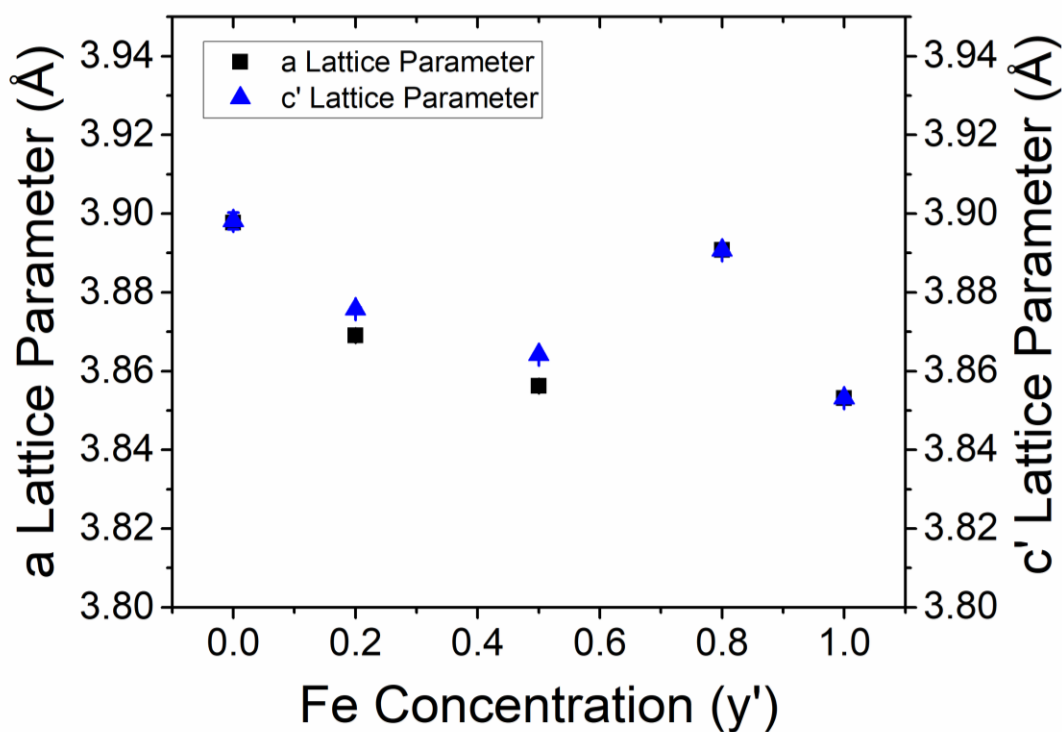
Figure 64 – Lattice Parameters for the PBSCF B-Site double perovskite oxide data series. The c' lattice parameter is displayed as the pseudo-cubic lattice parameter, calculated via equation 1.

The results shown in Figure 64 are, at initial glance, counter intuitive and at odds with the results and discussion of PBCF double perovskite oxides, where the lattice parameter and crystal volume increased with higher Fe content. The ionic radii of iron ions is around ~6% larger than that of cobalt (in high spin, 3+ oxidation state, and 6 coordinate complexes).[154] Therefore, one

would expect that increasing the saturation of Fe ions in the double perovskite crystal lattice would lead to an increase in the lattice parameters as was seen in PBCF chapter. However, as previously discussed , the addition of Sr^{2+} ions into the $PrBaCo_{2(1-y)}Fe_{2y}O_6$ crystal lattice causes perturbations in distance between the layers due to the smaller ionic radii of Sr^{2+} compared to Ba^{2+}. This decrease in the layer difference may cause a phenomenon known as octahedral tilting to occur. Whilst this has been discussed in chapter 4 ($Pr_{1-x}Sr_xFeO_3$) chapter with increasing rates of Sr^{2+} concentration into a saturated B site perovskite oxide, the environment of the PBSCF B Site double perovskites is slightly different, as the concentration of Sr^{2+} is consistent within the material series and it is the B site stoichiometry which is being altered. There are many different mechanisms behind octahedral tilting in perovskite crystal systems,[220] and a plethora of literature papers attempting to explain and manipulate the octahedral tilting in order to create advantageous material properties for a wide variety of applications. However, in the case of the PBSCF B Site double perovskite oxides, the hypothesised mechanism is steric in nature. As discussed, the addition of Sr^{2+} ions into the double perovskite structure will shorten the distance between the layers, which will cause steric interference within the unit cell. This interference can be countered by the rotation (or tilting) of the BO octahedra to a more energetically favourable state, which will cause an overall shrinking of the unit cell, and as Fe ions have a larger ionic radius than cobalt ions, this effect will be more pronounced with increasing concentration of iron. The increased octahedral tilting in iron complex compared to cobalt complexes can be confirmed through simulations using systems such as Structure Prediction Diagnostic Software (SPuDS).[221] The same trend as the lattice parameters is displayed in the formula-unit (Z) normalised crystal volume (denoted at Vol'), which is shown in Figure 65.
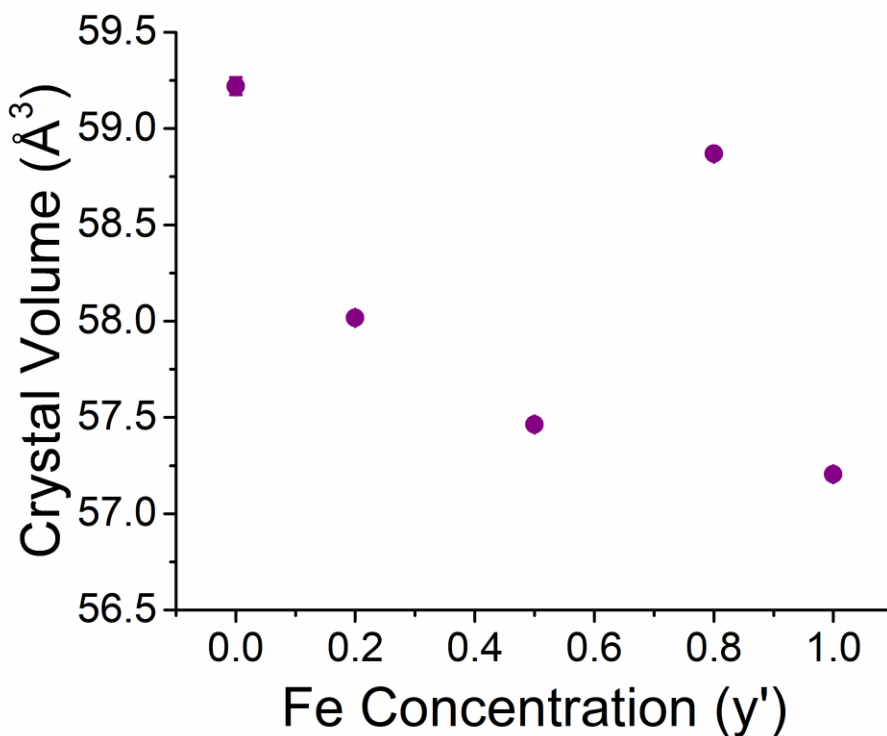
Figure 65 – Formula-unit (Z) normalised crystal volume of the B-site doped $Pr(Ba_{0.5}Sr_{0.5})Co_{2(1-y')}Fe_{2y'}O_6$ (PBSCF B Site) material series

7.2.4 Conclusion

The main conclusion from the analysis of the material's crystal structure, aside from the aforementioned anomalous result, is how the material characteristics compare to the PBCF ($PrBaCo_{2(1-y)}Fe_{2y}O_6$) double perovskite oxides studied in CHAPTER 3. The addition of the Sr^{2+} cation lead to perturbations in the crystal structure. These perturbations manifested as a reduction in phase purity, which was hypothesised in the introduction of this chapter, as well as increase steric interactions between the A' site and the B site cations which caused a reduction in the unit cell parameters and volume due to octahedral tilting of the B-O octahedra. The addition of the Sr^{2+} ion into the PBCF structure reduced the doubling in the double perovskite structure, causing a phase transition in the y ≤ 0.5 materials from *P4/mmm* tetragonal symmetry to the $Pm\overline{3}m$ cubic symmetry, as demonstrated by the lack of splitting in the (110) Bragg reflection peak as shown in Figure 63 and Figure 64.

7.3 Electrochemistry

As previously discussed, cyclic voltammetry is a valuable technique in quantifying the electrochemical activity of a material. Cyclic voltammograms for the PBSCF B site doped materials are shown in Figure 66. As described in the materials and methods (chapter 3), cyclic voltammograms were collected by scanning between 1.30 and 1.80 V_{RHE} in both directions, with a scan rate of 5 mV s^{-1} in a N_2 saturated 0.1 M KOH electrolyte solution. The working electrode was kept at an angle in order to encourage liberation of oxygen gas from the surface to prevent inaccuracies from bubbles at the electrode-electrolyte interface. Data was initially collected using a leakless Ag/AgCl reference electrode, which was then converted to the Reversible Hydrogen Electrode (V_{RHE}) post-test. All scans were *iR* corrected using data gathered from fitting of the EIS curves. In order to overcome any initial material capacitance, a full scan was completed before the data was gathered.
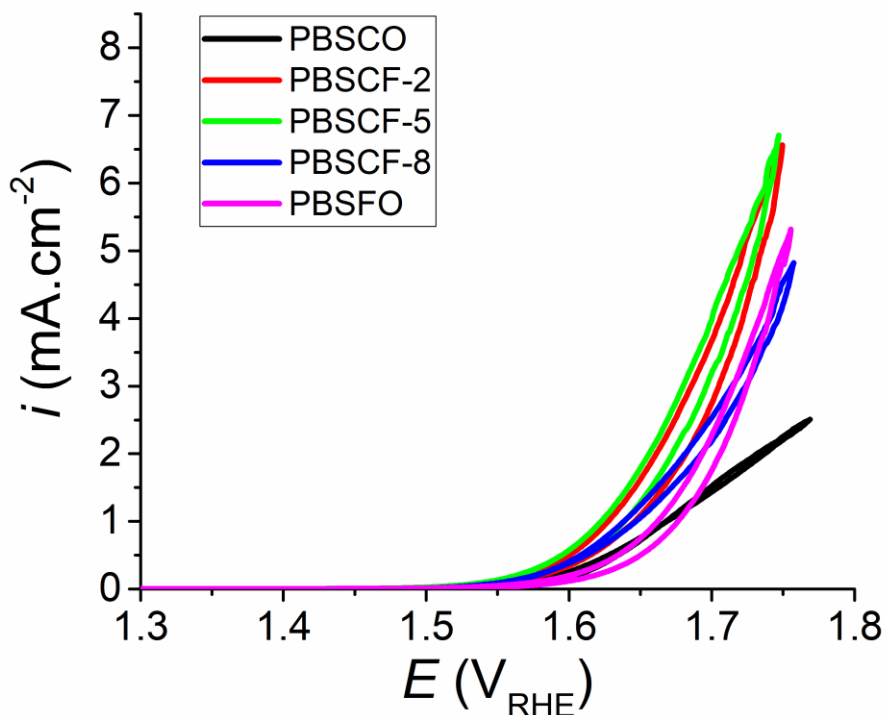
Figure 66 – Cyclic Voltammograms for the PBSCF B Site material series. Data was gathered between 1.30 and 1.80 V_{RHE}, with a scan rate of 5 mV/s in a 0.1 M KOH electrolyte solution. A full scan was undertaken before in order to overcome any material capacitance. Data has been iR corrected using the R_s value from the Electrical Impedance Spectroscopy (EIS).

From the scans shown in Figure 66, similar to the results seen in PrBaCo$_{2(1-y)}$Fe$_{2y}$O$_6$ double perovskite oxides, the materials with mixed B site stoichiometries are the superior

electrocatalysts. The y' = 0.5 and 0.8 materials show dominant performance, followed by the high iron content y' = 0.8 and Fe saturated y' = 1, and the cobalt saturated y' = 0 material exhibits the lowest performance under these conditions. The poor performance of the cobalt saturated is likely due to the relatively poor phase purity, which was hypothesised to be caused by material perturbations in the introduction of this chapter. Interestingly, the distribution in the performance of the mixed stoichiometry material and the iron saturated PBSFO material is considerably lower when compared to Sr^{2+} free $PrBaCo_{2(1-y)}Fe_{2y}O_6$ double perovskite oxide.

The PBSCF-2 and PBSCF-5 materials generated a current response in the range of 3.68 – 3.97 mA cm^{-2}, which is more active than the highest performing PBCF (maximum of 3.38 mA cm^{-2} at 1.70 V_{RHE}). This trend of the mixed B site stoichiometry materials out-performing the saturated materials is to be expected, as displayed in PBCF chapter, and is in line with reports from similar materials found in the literature.[186-188, 222-224] Despite the sub-optimal performance of the performance of the cobalt saturated PBSCO (y' = 0) material as an OER electrocatalyst and the poor phase purity from the addition of Sr^{2+} ions into the crystal lattice, the observed benefits of the intrinsic double perovskite oxide structure are still prevalent when compared to the electrocatalytic activity of the pristine $PrFeO_3$ (PFO) single perovskite oxide studied in chapter 4

In comparison to the strontium free PBCF material series, there is a higher degree of hysteresis in the mixed B site PBSCF materials. Although the phenomenon of hysteresis arising in cyclic voltammetry scans of perovskite oxides is an important discussion in the field of solar cell OER applications, it is not often explored for alkaline electrolysers. Hysteresis in solar cell devices is often attributed to interface change accumulation at the surface of the catalyst brought about by ferroelectric perovskite oxide electrodes.[225-229] However, as ferroelectricity is a function of a non-centrosymmetric unit cell, described as the lack of a point of inversion in as part of the symmetry operators, and as this material series is a $Pm\bar{3}m$ space group configuration there can be no ferroelectric effect due to the inversion point centre symbolized as $\bar{3}$.[230, 231] Therefore, as was the case for the y = 0 $PrBaCo_2O_6$ material discussed in chapter 5, the small hysteresis observed in the B Site doped PBSCF materials is most likely due to the residual material capacitance,[197] or by the *in-situ* formation of electrochemically inactive species at the material surface (electrode-electrolyte boundary).[198] However, as previously discussed, distinguishing between mechanisms

of hysteresis in cyclic voltammograms is complex and requires computational modelling alongside experimental data, however a logical hypothesis would be that the poorer electrocatalytic performance of the PBSCO (y' = 0) is more likely to be caused by phase impurities which total 20% of the sample, rather than any process that could be responsible for the hysteresis.

Nyquist plots obtained via electrical impedance spectroscopy (EIS) measurements from the PBSCF B Site doped double perovskite oxide material series are shown in Figure 67. The electrical impedance spectroscopy (EIS) measurements were taken at 1.70 V_{RHE} which was determined by the initial onset activity of the material determined by cyclic voltammetry experiments (Figure 66), over a frequency range of $10^5 - 10^{-1}$ Hz in 0.1 M KOH electrolyte solution.
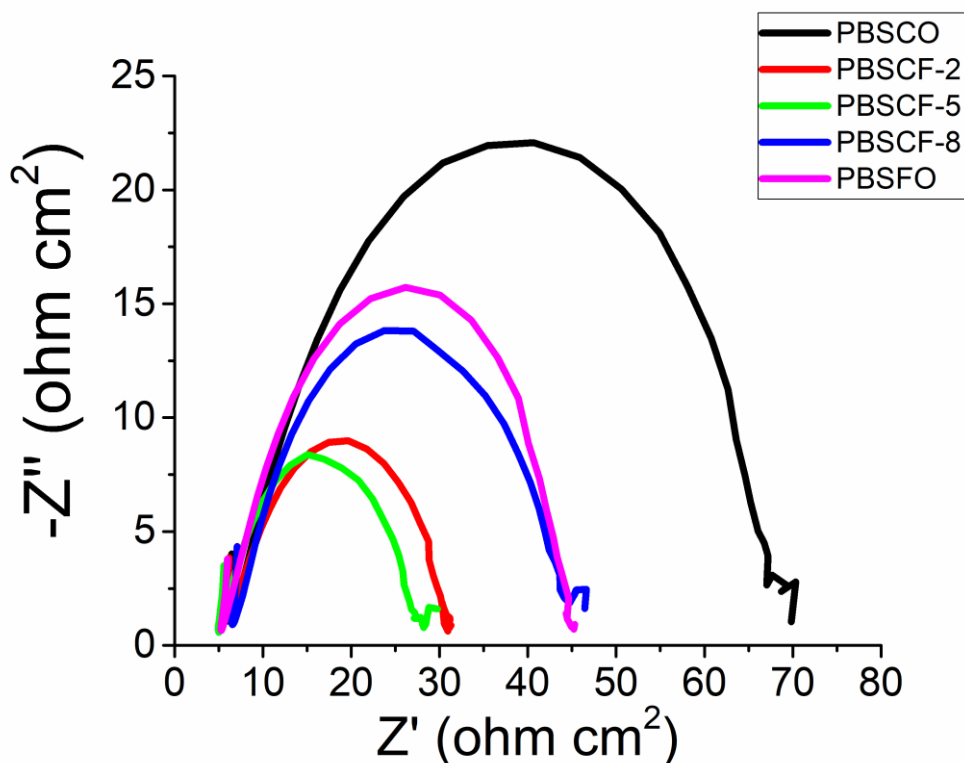
Figure 67 – Nyquist plots gathered from Electrical Impedance Spectroscopy (EIS) for the PBSCF B Site doped double perovskite oxide material series in 0.1 M KOH taken at 1.70 V_{RHE} over a frequency range of 10^5 to 10^{-1} Hz.

The solution resistance (R_s), which is the point, expressed in terms of the real impedance value (Z'), in which the imaginary impedance value (-Z'') is equal to zero, in other words when the line meets the *x* axis in the high frequency (low Z') range. The solution resistance (R_s) is an exceptional useful parameter for 2 main reasons. Firstly, it can be used to ensure that data gathered during the electrochemical testing (assuming the tests were done in series without

break), as the R_s arises from a combination of electrical impedance arising from the internal wire connections and the electrolyte solution, so any significant divergence in the R_s values may indicate faulty wiring or incorrect solution resistance. This descriptor lends itself well to the second main reason that the R_s is such a useful parameter, which is what is known as internal resistance, or *iR*, correction. The *iR* correction is used to ensure that electrochemical results gathered from different instruments are comparable, as electrochemical techniques such as cyclic voltammetry (CV) generally report the potential normalised to the reversible hydrogen electrode (RHE) as per the Nernst equation, with the internal resistances subtracted from the measurement. This ensures that results from different systems across the literature can be compared with a reasonable degree of accuracy. With this information it can be assured from observing Figure 67 that there was no significant difference in the R_s of the PBSCF B Site doped double perovskite oxide material series, ensuring that differences in the electrochemical results were more likely to be from the variations in the material rather than the electrochemical environment, which provides further validity of the various electrochemical results.

In the same way that solution resistance (R_s) is determined by the point in which the Nyquist plot touches the *x* axis in the high frequency (low Z') region, the polarisation resistance (R_p) is determined from the distance between the R_s value, and the value in which the Nyquist plot touches the *x* axis in the low frequency (high Z') range. As previously discussed, the polarisation resistance (R_p) is the resistance of a material species to oxidation from an externally applied voltage.[199] The polarisation resistances (R_p) found in Figure 67 follow the same trend as described for the cyclic voltammograms in Figure 66.

Nyquist plots of EIS data are exceptionally useful for determining the electrocatalytic performance and material suitability of electrocatalysts. Mathematical models can be used to fit the Nyquist plot in order to determine material factors such as R_p, R_s and estimated material capacitance. As previously discussed, formulating a model is further discussed in chapter 3, however a brief overview for model formulation is presented in this chapter for clarity.

When a model is developed for a specific process, there are a few key things to consider. The initial descriptor is what type of electrical process the material class can facilitate such as resistors or conductors. Perovskite based alkaline electrolyser anodes are generally considered

semiconductors which, as the name suggests, are a class of materials where the level of conductivity is somewhere in between a conductor and an insulator. The second consideration is more specific to the chemical aspect of the electrochemical reaction. Alkaline electrolyser systems are composed of a liquid electrolyte in contact with a solid electrode, which causes a boundary known as double layer capacitance at the junction where the catalyst surface meets the electrolyte. When an electrical system contains a double layer which is an imperfect capacitor, such as in alkaline oxygen evolution electro catalysis, this is accounted for in the equivalent electrical circuit model by constant phase elements (CPE). As Nyquist plots show a range of frequencies, both the high and low frequencies (HF and LF) are taken into consideration within this model, with the majority of resistance occurring from internal connections shown by a small, poorly defined, semi-circle at the high frequency (low value of Z') range,[200] and the resistances from the material displayed as the main semi-circle from Rs to Rp. As the difference between these two semi-circles is larger than an order of magnitude, it is best to consider both semi-circles in the model.[201] The model used for the 3-electrode cell testing is shown in Figure 68.
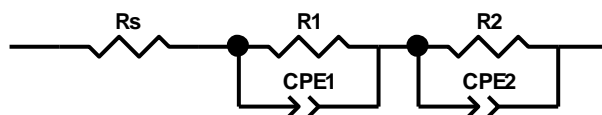
Figure 68 – Equivalent electrical circuit used for modelling perovskite oxide electrocatalysts, encompassing both semi-circles.

Where R_s models the resistance of the electrolyte, R_1 and CPE_1 are the resistance and constant phase element for respectively the initial semi-circle arising from internal resistances within the system, and R_2 and CPE_2 refer to the resistance and constant phase element for the semi-circle arising from the catalyst.

Each of the fitted parameters shown in Figure 43 can be used to calculate the approximate value for the capacitance of the material using equation 4.[202]

$$C = R^{\left(\frac{1-n}{n}\right)} \times Q^{\left(\frac{1}{n}\right)} \tag{4}$$

Where C is the capacitance (in Farads), R is the resistance, Q is the pseudo capacitance, and n is related to the shape of the semicircle.

Table 11 – Values used in the calculation of the capacitance for PBSCF B Site doped double perovskite oxides, and comparisons to other high performing materials in this study.

Fe (y')	C (F)
0	1.38×10^{-4}
0.2	3.58×10^{-5}
0.5	4.65×10^{-5}
0.8	1.27×10^{-4}
1.0	1.36×10^{-4}
$PrBaCo_{1.6}Fe_{0.4}O_6$	3.98×10^{-4}
$Pr_{0.5}Sr_{0.5}FeO_3$	1.33×10^{-3}

The estimated capacitances of the PBSCF B Site doped material series, are listed in Table 11. As previously discussed, care should be taken whilst drawing conclusions from the approximated capacitance values. However, observation of the order of magnitude of the capacitance values. The highest performing PBSCF B Site double perovskite oxides are in the order of 10^{-5} Farads, which is considerably lower than the best performing PSFO single perovskite oxide, and lower than the best performing Sr^{2+} free double perovskite oxides. The addition of Sr^{2+} into the PBCF double perovskite oxide increasing the electrical conductivity is in line with the hypothesis outlined in the beginning of this chapter.

7.4 Appendix
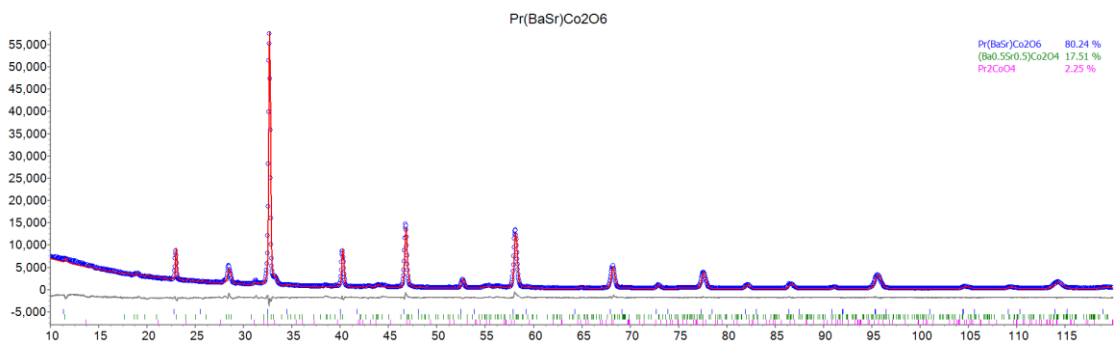
Figure 69 – Ambient temperature and pressure powder X-Ray Diffraction pattern for y' = 0 material Pr(Ba$_{0.5}$Sr$_{0.5}$)Co$_2$O$_6$ (PBSCO) in P4/mmm tetragonal configuration, refined with Rietveld method. Blue line shows experimentally measured data, red line shows calculated data, and grey line shows the difference between. Estimated %$_{wt}$ values for the relevant phases are listed in the top right-hand corner.
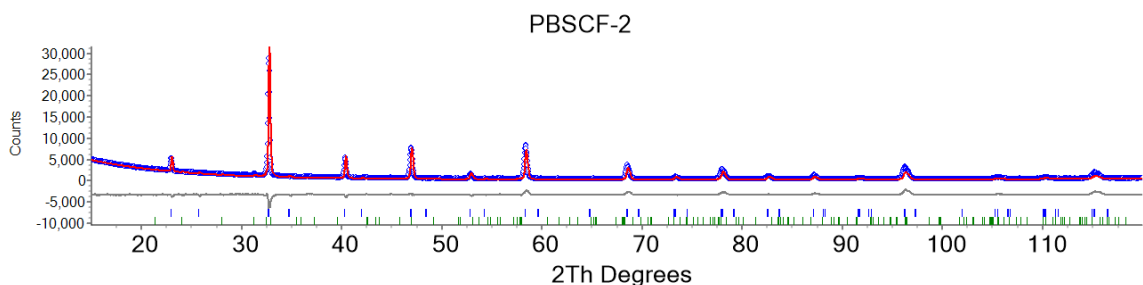
Figure 70 – Ambient temperature and pressure powder X-Ray Diffraction pattern for y' = 2 material Pr(Ba$_{0.5}$Sr$_{0.5}$)Co$_{1.6}$Fe$_{0.4}$O$_6$ (PBSCF-2) in P4/mmm tetragonal configuration, refined with Rietveld method. Blue line shows experimentally measured data, red line shows calculated data, and grey line shows the difference between. Estimated %$_{wt}$ values for the relevant phases are listed in the top right-hand corner.
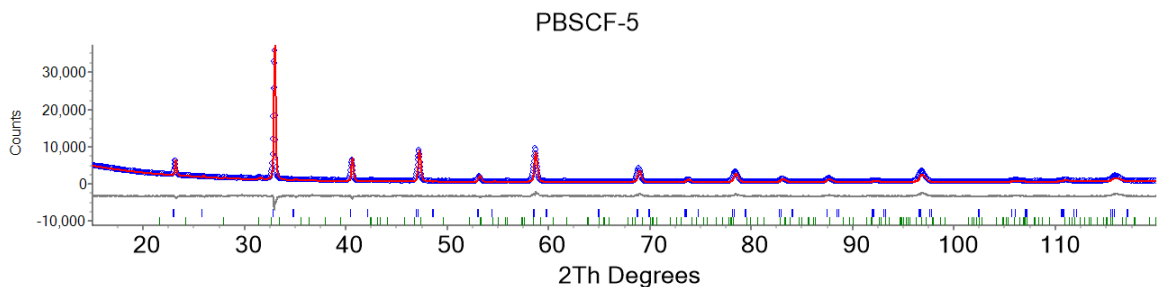
Figure 71 – Ambient temperature and pressure powder X-Ray Diffraction pattern for y' = 5 material Pr(Ba$_{0.5}$Sr$_{0.5}$)CoFeO$_6$ (PBSCF-5) in P4/mmm tetragonal configuration, refined with Rietveld method. Blue line shows experimentally measured data, red line shows calculated data, and grey line shows the difference between. Estimated %$_{wt}$ values for the relevant phases are listed in the top right-hand corner.

0.
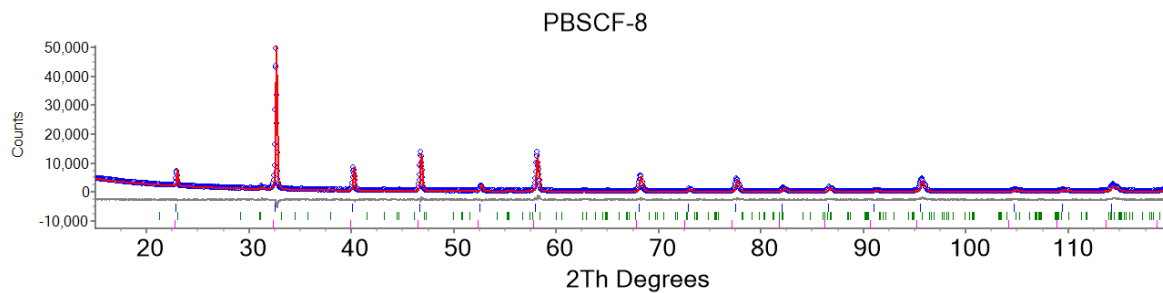
Figure 72 – Ambient temperature and pressure powder X-Ray Diffraction pattern for y' = 8 material Pr(Ba$_{0.5}$Sr$_{0.5}$)Co$_{0.4}$Fe$_{1.6}$O$_6$ (PBSCF-8) in Pm-3m cubic configuration, refined with Rietveld method. Blue line shows experimentally measured data, red line shows calculated data, and grey line shows the difference between. Estimated %$_{wt}$ values for the relevant phases are listed in the top right-hand corner.
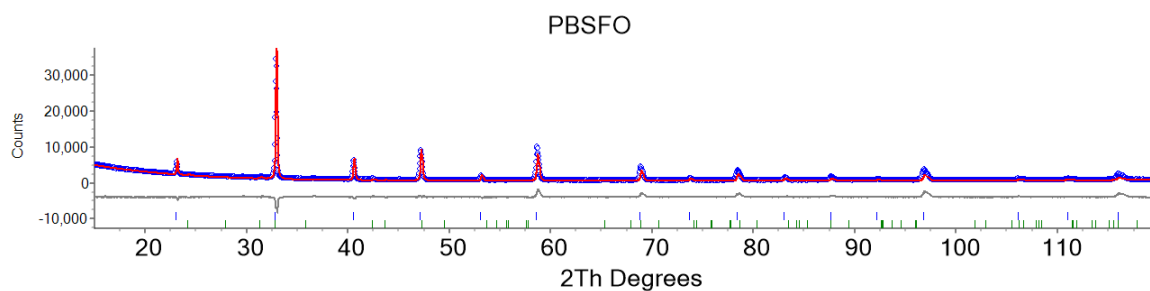
Figure 73 – Ambient temperature and pressure powder X-Ray Diffraction pattern for y' = 1 material Pr(Ba$_{0.5}$Sr$_{0.5}$)Fe$_2$O$_6$ (PBSFO) in Pm-3m cubic configuration, refined with Rietveld method. Blue line shows experimentally measured data, red line shows calculated data, and grey line shows the difference between. Estimated %$_{wt}$ values for the relevant phases are listed in the top right-hand corner.

Chapter 8. Future Work

The results and discoveries from the PhD project provide a strong possibility for further exploration. There are a variety of ways that this work could be continued, but most of these will fall under tree main schools of thought: altering the catalyst chemical composition, altering the surface and grain morphology of the material, or focussing on pH reduction of electrolytes.

There is also the opportunity to scale up the full cell electrolyser system as described in chapter 4; however, this would include mechanical and engineering challenges such as dealing with heat recycling, electrolyte flow rates, and mechanical strain as well as material considerations of the anode, cathode, and the polymer separator. This investigation is far outside of the scope and challenges faced during this research, so it would not be correct to use this work as a basis for such a scale up.

Altering the chemical composition of the catalyst materials provides an almost unlimited scope of future work due to the sheer number of possible precious metal free oxide configurations. This is true even when focussing on single and double perovskite oxide structures. Using this research (especially chapters 4 and 7) as a jump off point, tuning the band gap of the material by further A site doping with other rare/alkaline earth cations in both ABO_3 and $AA'B_2O_6$ configurations, as well as controlled oxygen vacancy concentration is hypothesised to lead to extremely high oxygen evolution activity. In order to gain a thorough understanding of this, it would be pertinent to apply further characterisation techniques than are discussed in this thesis. Specifically, density functional theory (DFT) would be an important computational technique in order to fully realise the effect of various A site doping on the band gap and further electronic structure of the material. For maximum impact, this would involve the use of beamline time and collaboration with synchrotron institutions such as Diamond or the European Synchrotron Radiation Facility (ESRF). Writing a strong proposal utilising the information presented in this PhD project to the relevant beamlines in these institutions would be a major initial milestone for any PhD or post-doctoral researcher undertaking new research using this work.

Although altering the chemical composition of the catalyst material has strong potential to lead to high performance OER catalysts, the field for this specific research is fairly saturated. A considerably more novel approach would be to continue on the work presented in chapter 6 in this thesis and develop catalyst materials with different morphologies through the use of various

wet chemical synthesis techniques. Obviously as this is a more novel approach, there is inherently more risk associated with this approach in the way that a lot of materials will show poor/no performance, so would most likely be suitable for post-doctoral research. However, there are many studies of interesting particle morphology and size of materials that have been synthesised through hydrothermal synthesis as discussed in chapter 6 that could form the basis of some novel and high impact research. In particular, high resolution TEM images could provide insights into the catalytic surface of these materials which would provide a highly specific characterisation that is not commonly seen in similar OER catalyst literature.

Finally, the third continuation of this work is more of a general electrolyser-based work in which the focus is less focussed on the specifics of the anodic performance in the set-up and is instead focussed on the performance of the alkaline electrolyser cell with electrolyte pH values closer to 7. Obviously being able to generate clean, high purity hydrogen and oxygen fuel from neutral pH water sources would be a massive step forward in the large-scale implementation of the technology. Not only would this improve the safety of the systems as operators need not come into contact with high alkaline or acidic electrolytes, but this would also reduce costs associated with electrolyte preparation and maintenance and reduce dependency on mined compounds such as potash. However, the relative lack of free OH^- ions in a solution of neutral water in comparison to 0.1+ mol solution of KOH/NaOH means that the performance of these so-called neutral electrolyser systems would be very poor. This would take concentrated efforts in altering both the anode and cathode composition, as well as separator material, and could possibly require intricate mechanical solutions in order to gather feasible results.

Overall, this body of work provides multiple opportunities for future work, be it in the form of PhD studies or post-doctoral research. This, combined with both the published and surrounding work discussed in this thesis, will hopefully be of use to any future researchers working in the field of electrolysers or catalyst characterisation.

Chapter 9. References

1. IEA, Global Energy Review 2021, https://www.iea.org/reports/global-energy-review-2021, (accessed 22/12/2021, 2021).

2. J. C. Minx, W. F. Lamb, R. M. Andrew, J. G. Canadell, M. Crippa, N. Döbbeling, P. M. Forster, D. Guizzardi, J. Olivier, G. P. Peters, J. Pongratz, A. Reisinger, M. Rigby, M. Saunois, S. J. Smith, E. Solazzo and H. Tian, *Earth Syst. Sci. Data*, 2021, **13**, 5213-5252.

3. P. Friedlingstein, M. W. Jones, M. O'Sullivan, R. M. Andrew, D. C. E. Bakker, J. Hauck, C. Le Quéré, G. P. Peters, W. Peters, J. Pongratz, S. Sitch, J. G. Canadell, P. Ciais, R. B. Jackson, S. R. Alin, P. Anthoni, N. R. Bates, M. Becker, N. Bellouin, L. Bopp, T. T. T. Chau, F. Chevallier, L. P. Chini, M. Cronin, K. I. Currie, B. Decharme, L. Djeutchouang, X. Dou, W. Evans, R. A. Feely, L. Feng, T. Gasser, D. Gilfillan, T. Gkritzalis, G. Grassi, L. Gregor, N. Gruber, Ö. Gürses, I. Harris, R. A. Houghton, G. C. Hurtt, Y. Iida, T. Ilyina, I. T. Luijkx, A. K. Jain, S. D. Jones, E. Kato, D. Kennedy, K. Klein Goldewijk, J. Knauer, J. I. Korsbakken, A. Körtzinger, P. Landschützer, S. K. Lauvset, N. Lefèvre, S. Lienert, J. Liu, G. Marland, P. C. McGuire, J. R. Melton, D. R. Munro, J. E. M. S. Nabel, S. I. Nakaoka, Y. Niwa, T. Ono, D. Pierrot, B. Poulter, G. Rehder, L. Resplandy, E. Robertson, C. Rödenbeck, T. M. Rosan, J. Schwinger, C. Schwingshackl, R. Séférian, A. J. Sutton, C. Sweeney, T. Tanhua, P. P. Tans, H. Tian, B. Tilbrook, F. Tubiello, G. van der Werf, N. Vuichard, C. Wada, R. Wanninkhof, A. Watson, D. Willis, A. J. Wiltshire, W. Yuan, C. Yue, X. Yue, S. Zaehle and J. Zeng, *Earth Syst. Sci. Data Discuss.*, 2021, **2021**, 1-191.

4. B. Metz, O. Davidson, P. Bosch, R. Dave and L. Meyer, *Climate change 2007: Mitigation of climate change*, Cambridge Univ. Press, 2007.

5. M. S. Dresselhaus and I. L. Thomas, *Nature*, 2001, **414**, 332-337.

6. G. Boyle, *Renewable Energy*, Oxford University Press and the Open University, Oxford, 2004.

7. R. Subbaraman, D. Tripkovic, K.-C. Chang, D. Strmcnik, A. P. Paulikas, P. Hirunsit, M. Chan, J. Greeley, V. Stamenkovic and N. M. Markovic, *Nat. Mater.*, 2012, **11**, 550-557.

8. I. Dincer, *Renew. Sust. Energ. Rev.*, 2000, **4**, 157-175.

9. M. Liserre, T. Sauter and J. Y. Hung, *IEEE. Ind. Electron. M.*, 2010, **4**, 18-37.

10. M. Ni, M. K. H. Leung, K. Sumathy and D. Y. C. Leung, *Int. J. Hydrogen Energ.*, 2006, **31**, 1401-1412.

11. S. Y. Gómez and D. Hotza, *Renew. Sust. Energ. Rev.*, 2016, **61**, 155-174.

12. V. Kyriakou, I. Garagounis, A. Vourros, E. Vasileiou and M. Stoukides, *Joule*, 2020, **4**, 142-158.

13. E. Fabbri and T. J. Schmidt, *ACS Catal.*, 2018, **8**, 9765-9774.

14. E. Fabbri, A. Habereder, K. Waltar, R. Kötz and T. J. Schmidt, *Catalysis Science & Technology*, 2014, **4**, 3800-3821.

15. I. Katsounaros, S. Cherevko, A. R. Zeradjanin and K. J. Mayrhofer, *Angew. Chem. Int. Edit.*, 2014, **53**, 102-121.

16. W. L. Leong, Z.-E. Ooi, D. Sabba, C. Yi, S. M. Zakeeruddin, M. Graetzel, J. M. Gordon, E. A. Katz and N. Mathews, *Advanced Materials*, 2016, **28**, 2439-2445.

17. J. Sehested, *Catal. Today*, 2006, **111**, 103-110.

18. D. Wilhelm, D. Simbeck, A. Karp and R. Dickenson, *Fuel Process. Technol.*, 2001, **71**, 139-148.

19.   L. Barelli, G. Bidini, F. Gallorini and S. Servili, *Energy*, 2008, **33**, 554-570.
20.   B. Neumann and K. Jacob, *Zeitschrift für Elektrochemie und angewandte physikalische Chemie*, 1924, **30**, 557-576.
21.   L. Feio, C. Hori, S. Damyanova, F. Noronha, W. Cassinelli, C. Marques and J. Bueno, *Applied Catalysis A: General*, 2007, **316**, 107-116.
22.   W. Cassinelli, L. Feio, J. Araujo, C. Hori, F. Noronha, C. Marques and J. Bueno, *Catal. Lett.*, 2008, **120**, 86-94.
23.   J. R. Rostrup-Nielsen, J. Sehested and J. K. Nørskov, 2002.
24.   H. Zhang, Z. Sun and Y. H. Hu, *Renew. Sust. Energ. Rev.*, 2021, **149**, 111330.
25.   I. Bobrova, N. Bobrov, V. Chesnokov and V. Parmon, *Kinetics and catalysis*, 2001, **42**, 805-812.
26.   V. Kuznetsov, O. Vitovsky and O. Gasenko, *Journal of Engineering Thermophysics*, 2009, **18**, 187-196.
27.   P. Prieto, A. Ferreira, P. Haddad, D. Zanchet and J. Bueno, *J. Catal.*, 2010, **276**, 351-359.
28.   J. D. Holladay, J. Hu, D. L. King and Y. Wang, *Catal. Today*, 2009, **139**, 244-260.
29.   S. Stucki, G. G. Scherer, S. Schlagowski and E. Fischer, *J. Appl. Electrochem.*, 1998, **28**, 1041-1049.
30.   M. Rashid, M. K. Al Mesfer, H. Naseem and M. Danish, *International Journal of Engineering and Advanced Technology*, 2015.
31.   M. E. G. Lyons and S. Floquet, *Phys. Chem. Chem. Phys.*, 2011, **13**, 5314-5335.
32.   E. Antolini, *ACS Catal.*, 2014, **4**, 1426-1440.
33.   Y. Lee, J. Suntivich, K. J. May, E. E. Perry and Y. Shao-Horn, *J. Phys. Chem. Lett.*, 2012, **3**, 399-404.
34.   L. Giordano, B. Han, M. Risch, W. T. Hong, R. R. Rao, K. A. Stoerzinger and Y. Shao-Horn, *Catal. Today*, 2016, **262**, 2-10.
35.   W. Tian, C. Wang, R. Chen, Z. Cai, D. Zhou, Y. Hao, Y. Chang, N. Han, Y. Li, J. Liu, F. Wang, W. Liu, H. Duan and X. Sun, *RSC. Adv.*, 2018, **8**, 26004-26010.
36.   F. Lyu, Q. Wang, S. M. Choi and Y. Yin, *Small*, 2019, **15**, 1804201.
37.   M. Tariq, W. Q. Zaman, W. Sun, Z. Zhou, Y. Wu, L.-m. Cao and J. Yang, *ACS Sustain. Chem. Eng.*, 2018, **6**, 4854-4862.
38.   W. T. Hong, M. Risch, K. A. Stoerzinger, A. Grimaud, J. Suntivich and Y. Shao-Horn, *Energ. Environ. Sci.*, 2015, **8**, 1404-1427.
39.   J. Rossmeisl, Z. W. Qu, H. Zhu, G. J. Kroes and J. K. Nørskov, *J. Electroanal. Chem.*, 2007, **607**, 83-89.
40.   B. Zhao, L. Zhang, D. Zhen, S. Yoo, Y. Ding, D. Chen, Y. Chen, Q. Zhang, B. Doyle, X. Xiong and M. Liu, *Nat. Commun.*, 2017, **8**, 14586.
41.   J. Suntivich, K. J. May, H. A. Gasteiger, J. B. Goodenough and Y. Shao-Horn, *Science*, 2011, **334**, 1383-1385.
42.   J. O. M. Bockris and T. Otagawa, *J. Electrochem. Soc.*, 1984, **131**, 290-302.
43.   B. Han, A. Grimaud, L. Giordano, W. T. Hong, O. Diaz-Morales, L. Yueh-Lin, J. Hwang, N. Charles, K. A. Stoerzinger, W. Yang, M. T. M. Koper and Y. Shao-Horn, *The Journal of Physical Chemistry C*, 2018, **122**, 8445-8454.
44.   M. T. Buscaglia, M. Bassoli, V. Buscaglia and R. Alessio, *J. Am. Ceram. Soc.*, 2005, **88**, 2374-2379.

45. A. M. Huízar-Félix, T. Hernández, S. de la Parra, J. Ibarra and B. Kharisov, *Powder Technol.*, 2012, **229**, 290-293.

46. X. Li, C. Tang, M. Ai, L. Dong and Z. Xu, *Chem. Mater.*, 2010, **22**, 4879-4889.

47. M. Lebid and M. Omari, *Arab. J. Sci. Eng.*, 2014, **39**, 147-152.

48. M. L. Moreira, E. C. Paris, G. S. do Nascimento, V. M. Longo, J. R. Sambrano, V. R. Mastelaro, M. I. B. Bernardi, J. Andrés, J. A. Varela and E. Longo, *Acta Mater.*, 2009, **57**, 5174-5185.

49. G. Xu, Z. Ren, P. Du, W. Weng, G. Shen and G. Han, *Advanced Materials*, 2005, **17**, 907-910.

50. E.-h. Yang and D. J. Moon, *RSC. Adv.*, 2016, **6**, 112885-112898.

51. C. Zhu, A. Nobuta, I. Nakatsugawa and T. Akiyama, *Int. J. Hydrogen Energ.*, 2013, **38**, 13238-13248.

52. S. Bie, Y. Zhu, J. Su, C. Jin, S. Liu, R. Yang and J. Wu, *J. Mater. Chem. A*, 2015, **3**, 22448-22453.

53. K. J. May, C. E. Carlton, K. A. Stoerzinger, M. Risch, J. Suntivich, Y.-L. Lee, A. Grimaud and Y. Shao-Horn, *J. Phys. Chem. Lett.*, 2012, **3**, 3264-3270.

54. J.-I. Jung, M. Risch, S. Park, M. G. Kim, G. Nam, H.-Y. Jeong, Y. Shao-Horn and J. Cho, *Energ. Environ. Sci.*, 2016, **9**, 176-183.

55. C. Jin, X. Cao, F. Lu, Z. Yang and R. Yang, *Int. J. Hydrogen Energ.*, 2013, **38**, 10389-10393.

56. J.-I. Jung, H. Y. Jeong, J.-S. Lee, M. G. Kim and J. Cho, *Angew. Chem. Int. Edit.*, 2014, **126**, 4670-4674.

57. W. G. Hardin, D. A. Slanac, X. Wang, S. Dai, K. P. Johnston and K. J. Stevenson, *J. Phys. Chem. Lett.*, 2013, **4**, 1254-1259.

58. M. Bursell, M. Pirjamali and Y. Kiros, *Electrochim. Acta*, 2002, **47**, 1651-1660.

59. J. R. Petrie, V. R. Cooper, J. W. Freeland, T. L. Meyer, Z. Zhang, D. A. Lutterman and H. N. Lee, *J. Am. Chem. Soc.*, 2016, **138**, 2488-2491.

60. Y. Zhu, W. Zhou, J. Yu, Y. Chen, M. Liu and Z. Shao, *Chem. Mater.*, 2016, **28**, 1691-1697.

61. Y. Ren, R. Küngas, R. J. Gorte and C. Deng, *Solid State Ionics*, 2012, **212**, 47-54.

62. S. Raabe, D. Mierwaldt, J. Ciston, M. Uijttewaal, H. Stein, J. Hoffmann, Y. Zhu, P. Blöchl and C. Jooss, *Adv. Funct. Mater.*, 2012, **22**, 3378-3388.

63. X. Xu, C. Su, W. Zhou, Y. Zhu, Y. Chen and Z. Shao, *Adv. Sci.*, 2016, **3**, 1500187.

64. S. K. Tiwari, S. P. Singh and R. N. Singh, *J. Electrochem. Soc.*, 1996, **143**, 1505-1510.

65. K.-N. Jung, J.-H. Jung, W. B. Im, S. Yoon, K.-H. Shin and J.-W. Lee, *ACS Appl. Mater. Inter.*, 2013, **5**, 9902-9907.

66. W. Zhou, M. Zhao, F. Liang, S. C. Smith and Z. Zhu, *Mater. Horizons*, 2015, **2**, 495-501.

67. R. N. Singh and B. Lal, *Int. J. Hydrogen Energ.*, 2002, **27**, 45-55.

68. E. M. Garcia, H. A. Tarôco, T. Matencio, R. Z. Domingues and J. A. F. dos Santos, *Int. J. Hydrogen Energ.*, 2012, **37**, 6400-6406.

69. H. W. Brinks, H. Fjellvåg, A. Kjekshus and B. C. Hauback, *J. Solid State Chem.*, 2000, **150**, 233-249.

70. K. Zhu, T. Wu, M. Li, R. Lu, X. Zhu and W. Yang, *J. Mater. Chem. A*, 2017, **5**, 19836-19845.

71. V. Antonucci, A. Di Blasi, V. Baglio, R. Ornelas, F. Matteucci, J. Ledesma-Garcia, L. G. Arriaga and A. S. Aricò, *Electrochim. Acta*, 2008, **53**, 7350-7356.

72. J. Ahmed, N. Alhokbany, M. Ubaidullah, S. Mutehri, M. A. M. Khan and S. M. Alshehri, *Ceram. Int.*, 2020, **46**, 20038-20044.

73. W. T. Grubb, *J. Electrochem. Soc.*, 1959, **106**, 275.
74. S. Slade, S. Campbell, T. Ralph and F. Walsh, *J. Electrochem. Soc.*, 2002, **149**, A1556.
75. M. Conte, A. Iacobazzi, M. Ronchetti and R. Vellone, *J. Power Sources*, 2001, **100**, 171-187.
76. F. N. Khatib, T. Wilberforce, O. Ijaodola, E. Ogungbemi, Z. El-Hassan, A. Durrant, J. Thompson and A. G. Olabi, *Renew. Sust. Energ. Rev.*, 2019, **111**, 1-14.
77. X. Sun, K. Xu, C. Fleischer, X. Liu, M. Grandcolas, R. Strandbakke, T. S. Bjørheim, T. Norby and A. Chatzitakis, *Catalysts*, 2018, **8**, 657.
78. L. Bi, S. Boulfrad and E. Traversa, *Chem. Soc. Rev.*, 2014, **43**, 8255-8270.
79. M. Ni, M. K. H. Leung and D. Y. C. Leung, *Int. J. Hydrogen Energ.*, 2008, **33**, 2337-2354.
80. H. Wendt, *Electrochemical hydrogen technologies: Electrochemical production and combustion of hydrogen*, Elsevier Science Limited, 1990.
81. J. W. Sheffield, K. B. Martin and R. Folkson, in *Alternative Fuels and Advanced Vehicle Technologies for Improved Environmental Performance*, ed. R. Folkson, Woodhead Publishing, 2014, DOI: https://doi.org/10.1533/9780857097422.1.117, pp. 117-137.
82. M. David, C. Ocampo-Martínez and R. Sánchez-Peña, *Journal of Energy Storage*, 2019, **23**, 392-403.
83. M. Bodner, A. Hofer and V. Hacker, *WIREs Energy and Environment*, 2015, **4**, 365-381.
84. Y. Guo, G. Li, J. Zhou and Y. Liu, *IOP Conference Series: Earth and Environmental Science*, 2019, **371**, 042022.
85. Ø. Ulleberg, *Int. J. Hydrogen Energ.*, 2003, **28**, 21-33.
86. I. C. Man, H.-Y. Su, F. Calle-Vallejo, H. A. Hansen, J. I. Martínez, N. G. Inoglu, J. Kitchin, T. F. Jaramillo, J. K. Nørskov and J. Rossmeisl, *ChemCatChem*, 2011, **3**, 1159-1165.
87. J. Nieminen, I. Dincer and G. Naterer, *Int. J. Hydrogen Energ.*, 2010, **35**, 10842-10850.
88. H. Dau, C. Limberg, T. Reier, M. Risch, S. Roggan and P. Strasser, *ChemCatChem*, 2010, **2**, 724-761.
89. H. Sun, Z. Yan, F. Liu, W. Xu, F. Cheng and J. Chen, *Advanced Materials*, 2020, **32**, 1806326.
90. Y. Zuo, Y. Liu, J. Li, R. Du, X. Han, T. Zhang, J. Arbiol, N. J. Divins, J. Llorca, N. Guijarro, K. Sivula and A. Cabot, *Chem. Mater.*, 2019, **31**, 7732-7743.
91. S. Zhou, N. Liu, Z. Wang and J. Zhao, *ACS Appl. Mater. Inter.*, 2017, **9**, 22578-22587.
92. N.-T. Suen, S.-F. Hung, Q. Quan, N. Zhang, Y.-J. Xu and H. M. Chen, *Chem. Soc. Rev.*, 2017, **46**, 337-365.
93. G. Bronoel and J. Reby, *Electrochim. Acta*, 1980, **25**, 973-976.
94. M. Plevová, J. Hnát and K. Bouzek, *J. Power Sources*, 2021, **507**, 230072.
95. K. S. Exner, *ACS Catal.*, 2020, **10**, 12607-12617.
96. S. Ivanov, in *Science and Technology of Atomic, Molecular, Condensed Matter & Biological Systems*, eds. T. P. Das, B. Sanyal and O. Eriksson, Elsevier, 2012, vol. 2, pp. 163-238.
97. L. C. Klein and G. J. Garvey, *J. Non-Cryst. Solids*, 1980, **38-39**, 45-50.
98. K. Nishio and T. Tsuchiya, in *Handbook of Sol-Gel Science and Technology: Processing, Characterization and Applications*, Springer International Publishing, 2018, pp. 133-154.
99. US3330697A, 1963.
100. M. Zayat and D. Levy, *Chem. Mater.*, 2000, **12**, 2763-2769.
101. J.-j. Zhang, J.-w. Ning, X.-j. Liu, Y.-b. Pan and L.-p. Huang, *Mater. Res. Bull.*, 2003, **38**, 1249-1256.
102. S. Wang, K. Huang, B. Zheng, J. Zhang and S. Feng, *Mater. Lett.*, 2013, **101**, 86-89.
103. J. Matthew, *Surf. Interface Anal.*, 2004, **36**, 1647-1647.

104. J. Epp, in *Materials Characterization Using Nondestructive Evaluation (NDE) Methods*, eds. G. Hübschen, I. Altpeter, R. Tschuncky and H.-G. Herrmann, Woodhead Publishing, 2016, DOI: 10.1016/B978-0-08-100040-3.00004-3, ch. 4, pp. 81-124.

105. N. W. Ashcroft and N. D. Mermin, *Journal*, 1976.

106. V. Pecharsky and P. Zavalij, *Fundamentals of powder diffraction and structural characterization of materials*, Springer Science & Business Media, 2008.

107. G. Caglioti, A. Paoletti and F. P. Ricci, *Nuclear Instruments*, 1958, **3**, 223-228.

108. B. H. Toby and R. B. Von Dreele, *J. Appl. Crystallogr.*, 2013, **46**, 544-549.

109. T. Degen, M. Sadki, E. Bron, U. König and G. Nénert, *Powder Diffr.*, 2014, **29**, S13-S18.

110. W. I. F. David, *J Res Natl Inst Stand Technol*, 2004, **109**, 107-123.

111. E. Prince, *Mathematical Techniques in Chrystallography and Materials Science*, Springer, New York, 3rd edn., 2004.

112. R. Young, *The rietveld method*, 1993.

113. B. H. Toby, *Powder Diffr.*, 2006, **21**, 67-70.

114. H. M. Rietveld, *J. Appl. Crystallogr.*, 1969, **2**, 65-71.

115. G. W. Stinton and J. S. O. Evans, *J. Appl. Crystallogr.*, 2007, **40**, 87-95.

116. R. E. Dinnebier, A. Leineweber and J. S. Evans, *Rietveld Refinement: Practical Powder Diffraction Pattern Analysis Using TOPAS*, Walter de Gruyter GmbH & Co KG, Berlin, 2018.

117. R. W. Cheary and A. Coelho, *J. Appl. Crystallogr.*, 1992, **25**, 109-121.

118. P. W. Atkins, *Oxf. Univ. Press, Melbourne Tokyo, Sixth Edition. pp87*, 1978.

119. R. D. Armstrong and M. Henderson, *Journal of Electroanalytical Chemistry and Interfacial Electrochemistry*, 1972, **39**, 81-90.

120. B. Malik, K. Vijaya Sankar, R. Konar, Y. Tsur and G. D. Nessim, *ChemElectroChem*, 2021, **8**, 517-523.

121. S. Kumar, K. Ojha and A. K. Ganguli, *Advanced Materials Interfaces*, 2017, **4**, 1600981.

122. A. J. Bard and L. R. Faulkner, *Electrochemical methods*, 2001, **2**, 580-632.

123. J. T. Stock and M. V. Orna, *Electrochemistry, past and present*, ACS Publications, 1989.

124. J. Suntivich, H. A. Gasteiger, N. Yabuuchi, H. Nakanishi, J. B. Goodenough and Y. Shao-Horn, *Nat. Chem.*, 2011, **3**, 546-550.

125. C. Jin, X. Cao, L. Zhang, C. Zhang and R. Yang, *J. Power Sources*, 2013, **241**, 225-230.

126. X. Rong, J. Parolin and A. M. Kolpak, *ACS Catal.*, 2016, **6**, 1153-1158.

127. S. Ward, M. A. Isaacs, G. Gupta, M. Mamlouk and S. S. Pramana, *Sustainable Energy & Fuels*, 2021, **5**, 154-165.

128. J. Masud, S. Umapathi, N. Ashokaan and M. Nath, *J. Mater. Chem. A*, 2016, **4**, 9750-9754.

129. P. T. Babar, A. C. Lokhande, M. G. Gang, B. S. Pawar, S. M. Pawar and J. H. Kim, *J. Ind. Eng. Chem.*, 2018, **60**, 493-497.

130. C. Chen, J. Cheng, S. Yu, L. Che and Z. Meng, *J. Cryst. Growth*, 2006, **291**, 135-139.

131. Y. Mao, S. Banerjee and S. S. Wong, *J. Am. Chem. Soc.*, 2003, **125**, 15718-15719.

132. Y. Mao, S. Banerjee and S. S. Wong, *Chem. Commun.*, 2003, 408-409.

133. D. D. Athayde, D. F. Souza, A. M. A. Silva, D. Vasconcelos, E. H. M. Nunes, J. C. Diniz da Costa and W. L. Vasconcelos, *Ceram. Int.*, 2016, **42**, 6555-6571.

134. P. Cousin and R. A. Ross, *Mat. Sci. Eng. A-Struct.*, 1990, **130**, 119-125.

135. J. A. Kilner, R. A. De Souza and I. C. Fullarton, *Solid State Ionics*, 1996, **86-88**, 703-709.

136. R. A. De Souza and J. A. Kilner, *Solid State Ionics*, 1999, **126**, 153-161.

137. M. W. Kanan and D. G. Nocera, *Science*, 2008, **321**, 1072-1075.

138. Y. Zhao, J. R. Swierk, J. D. Megiatto, B. Sherman, W. J. Youngblood, D. Qin, D. M. Lentz, A. L. Moore, T. A. Moore, D. Gust and T. E. Mallouk, *P. Natl. Acad. Sci. USA.*, 2012, **109**, 15612-15616.

139. J. I. Jung, M. Risch, S. Park, M. G. Kim, G. Nam, H. Y. Jeong, Y. Shao-Horn and J. Cho, *Energ. Environ. Sci.*, 2016, **9**, 176.

140. C.-F. Chen, G. King, R. M. Dickerson, P. A. Papin, S. Gupta, W. R. Kellogg and G. Wu, *Nano Energy*, 2015, **13**, 423-432.

141. E. Fabbri, M. Nachtegaal, T. Binninger, X. Cheng, B.-J. Kim, J. Durst, F. Bozza, T. Graule, R. Schäublin, L. Wiles, M. Pertoso, N. Danilovic, K. E. Ayers and T. J. Schmidt, *Nat. Mater.*, 2017, **16**, 925-931.

142. J. Luo, J.-H. Im, M. T. Mayer, M. Schreier, M. K. Nazeeruddin, N.-G. Park, S. D. Tilley, H. J. Fan and M. Grätzel, *Science*, 2014, **345**, 1593-1596.

143. E. A. Hernández-Pagán, N. M. Vargas-Barbosa, T. Wang, Y. Zhao, E. S. Smotkin and T. E. Mallouk, *Energ. Environ. Sci.*, 2012, **5**, 7582-7589.

144. K. Zeng and D. Zhang, *Prog. Energ. Combust.*, 2010, **36**, 307-326.

145. S. Jung, C. C. L. McCrory, I. M. Ferrer, J. C. Peters and T. F. Jaramillo, *J. Mater. Chem. A*, 2016, **4**, 3068-3076.

146. R. L. Doyle and M. E. G. Lyons, in *Photoelectrochemical Solar Fuel Production: From Basic Principles to Advanced Devices*, Springer International Publishing, Cham, 2016, pp. 41-104.

147. G. Gupta, K. Scott and M. Mamlouk, *J. Power Sources*, 2018, **375**, 387-396.

148. L. Qiu, T. Ichikawa, A. Hirano, N. Imanishi and Y. Takeda, *Solid State Ionics*, 2003, **158**, 55-65.

149. V. P. Kumar, Y. S. Reddy, P. Kistaiah and C. V. Reddy, *Int. J. Mod. Phys. B*, 2012, **26**, 1250174.

150. J. W. Stevenson, T. R. Armstrong, R. D. Carneim, L. R. Pederson and W. J. Weber, *J. Electrochem. Soc.*, 1996, **143**, 2722-2729.

151. P. Li, S. Ouyang, G. Xi, T. Kako and J. Ye, *J. Phys. Chem. C*, 2012, **116**, 7621-7628.

152. Z. Chen, T. A. Tyson, K. H. Ahn, Z. Zhong and J. Hu, *J. Magn. Magn. Mater.*, 2010, **322**, 3049-3052.

153. K. T. Lee and A. Manthiram, *J. Electrochem. Soc.*, 2005, **152**, A197-A204.

154. R. D. Shannon, *Acta Crystallogr. A*, 1976, **32**, 751-767.

155. K. Vidal, L. M. Rodríguez-Martínez, L. Ortega-San-Martín, E. Díez-Linaza, M. L. Nó, T. Rojo, A. Laresgoiti and M. I. Arriortua, *Solid State Ionics*, 2007, **178**, 1310-1316.

156. X. Cui, S. Li and X. Zhu, *Mater. Lett.*, 2014, **130**, 267-270.

157. I. D. Brown, *The Chemical Bond in Inorganic Chemistry: The Bond Valence Model*, Oxford University Press, Oxford, 2016.

158. J. L. Tallon, *Physica C*, 1990, **168**, 85-90.

159. S. She, J. Yu, W. Tang, Y. Zhu, Y. Chen, J. Sunarso, W. Zhou and Z. Shao, *ACS Appl. Mater. Inter.*, 2018, **10**, 11715-11721.

160. Z. Shen, Y. Zhuang, W. Li, X. Huang, F. E. Oropeza, E. J. M. Hensen, J. P. Hofmann, M. Cui, A. Tadich, D. Qi, J. Cheng, J. Li and K. H. L. Zhang, *J. Mater. Chem. A*, 2020, **8**, 4407-4415.

161. A. Grimaud, A. Demortière, M. Saubanère, W. Dachraoui, M. Duchamp, M.-L. Doublet and J.-M. Tarascon, *Nat. Energy*, 2016, **2**, 16189.

162. S. Lütkehoff, M. Neumann and A. Ślebarski, *Phys. Rev. B*, 1995, **52**, 13808-13811.

163. Y. Zhang, K. Han, X. Yin, Z. Fang, Z. Xu and W. Zhu, *J. Cryst. Growth*, 2009, **311**, 3883-3888.

164. L. Yan, R. Yu, G. Liu and X. Xing, *Scr. Mater.*, 2008, **58**, 707-710.

165. A. Bianconi, A. Kotani, K. Okada, R. Giorgi, A. Gargano, A. Marcelli and T. Miyahara, *Phys. Rev. B*, 1988, **38**, 3433-3437.
166. F. H. Aragón, I. Gonzalez, J. A. H. Coaquira, P. Hidalgo, H. F. Brito, J. D. Ardisson, W. A. A. Macedo and P. C. Morais, *J. Phys. Chem. C*, 2015, **119**, 8711-8717.
167. H. Ogasawara, A. Kotani, R. Potze, G. A. Sawatzky and B. T. Thole, *Phys. Rev. B*, 1991, **44**, 5465-5469.
168. M. I. Sosulnikov and Y. A. Teterin, *J. Electron Spectrosc. Relat. Phenom.*, 1992, **59**, 111-126.
169. M. S. Naughton, F. R. Brushett and P. J. A. Kenis, *J. Power Sources*, 2011, **196**, 1762-1768.
170. P. Nachimuthu, Y. J. Kim, S. V. N. T. Kuchibhatla, Z. Q. Yu, W. Jiang, M. H. Engelhard, V. Shutthanandan, J. Szanyi and S. Thevuthasan, *J. Phys. Chem. C*, 2009, **113**, 14324-14328.
171. A. P. Grosvenor, B. A. Kobe, M. C. Biesinger and N. S. McIntyre, *Surf. Interface Anal.*, 2004, **36**, 1564-1574.
172. J. Kim, X. Yin, K.-C. Tsao, S. Fang and H. Yang, *J. Am. Chem. Soc.*, 2014, **136**, 14646-14649.
173. M. Islam, M.-G. Jeong, I.-H. Oh, K.-W. Nam and H.-G. Jung, *J. Ind. Eng. Chem.*, 2020, **85**, 94-101.
174. J. Bak, H. Bin Bae and S.-Y. Chung, *Nat. Commun.*, 2019, **10**, 2713.
175. T. Shinagawa, A. T. Garcia-Esparza and K. Takanabe, *Sci. Rep.*, 2015, **5**, 13801.
176. D. He, G. He, H. Jiang, Z. Chen and M. Huang, *Chem. Commun.*, 2017, **53**, 5132-5135.
177. J. Zou, J. Park, B. Kwak, H. Yoon and J. Chung, *Solid State Ionics*, 2012, **206**, 112-119.
178. V. A. Cherepanov, T. V. Aksenova, L. Y. Gavrilova and K. N. Mikhaleva, *Solid State Ionics*, 2011, **188**, 53-57.
179. F. Jin, H. Xu, W. Long, Y. Shen and T. He, *J. Power Sources*, 2013, **243**, 10-18.
180. A. I. Klyndyuk and Y. A. Chizhova, *Funct. Mater.*, 2009, **16**, 17-22.
181. Y. N. Kim, J. H. Kim and A. Manthiram, *J. Power Sources*, 2010, **195**, 6411-6419.
182. A. I. Klyndyuk, *Inorganic Materials*, 2009, **45**, 942-945.
183. A. I. Klyndyuk and E. A. Chizhova, *Inorganic Materials*, 2013, **49**, 319-324.
184. Q. Sun, Z. Dai, Z. Zhang, Z. Chen, H. Lin, Y. Gao and D. Chen, *J. Power Sources*, 2019, **427**, 194-200.
185. J. Chen, M. Shen, X. Wang, J. Wang, Y. Su and Z. Zhao, *Catal. Commun.*, 2013, **37**, 105-108.
186. A. Ashok, A. Kumar, R. R. Bhosale, F. Almomani, S. S. Malik, S. Suslov and F. Tarlochan, *J. Electroanal. Chem.*, 2018, **809**, 22-30.
187. I. Yamada, A. Takamatsu, K. Asai, T. Shirakawa, H. Ohzuku, A. Seno, T. Uchimura, H. Fujii, S. Kawaguchi, K. Wada, H. Ikeno and S. Yagi, *The Journal of Physical Chemistry C*, 2018, **122**, 27885-27892.
188. T. G. Yun, Y. Heo, H. Bin Bae and S.-Y. Chung, *Nat. Commun.*, 2021, **12**, 824.
189. S. Bao, C. Ma, G. Chen, X. Xu, E. Enriquez, C. Chen, Y. Zhang, J. L. Bettis, M.-H. Whangbo, C. Dong and Q. Zhang, *Sci. Rep.*, 2014, **4**, 4726.
190. S. S. Pramana, A. Cavallaro, C. Li, A. D. Handoko, K. W. Chan, R. J. Walker, A. Regoutz, J. S. Herrin, B. S. Yeo, D. J. Payne, J. A. Kilner, M. P. Ryan and S. J. Skinner, *J. Mater. Chem. A*, 2018, DOI: 10.1039/C7TA06817D.
191. A. Grimaud, K. J. May, C. E. Carlton, Y.-L. Lee, M. Risch, W. T. Hong, J. Zhou and Y. Shao-Horn, *Nat. Commun.*, 2013, **4**, 2439.
192. H. Wang, J. Wang, Y. Pi, Q. Shao, Y. Tan and X. Huang, *Angew. Chem. Int. Edit.*, 2019, **58**, 2316-2320.

193.   Y. Zhu, L. Zhang, B. Zhao, H. Chen, X. Liu, R. Zhao, X. Wang, J. Liu, Y. Chen and M. Liu, *Adv. Funct. Mater.*, 2019, **29**, 1901783.

194.   F. Gunkel, L. Jin, D. N. Mueller, C. Hausner, D. S. Bick, C.-L. Jia, T. Schneller, I. Valov, R. Waser and R. Dittmann, *ACS Catal.*, 2017, **7**, 7029-7037.

195.   H. S. Kushwaha, A. Halder, P. Thomas and R. Vaish, *Electrochim. Acta*, 2017, **252**, 532-540.

196.   H. Sun, G. Chen, Y. Zhu, B. Liu, W. Zhou and Z. Shao, *Chemistry – A European Journal*, 2017, **23**, 5722-5728.

197.   M. Kosmulski, P. Próchniak and C. Saneluta, *Adsorption*, 2009, **15**, 172-180.

198.   T. Haisch, F. Kubannek, L. Nikitina, I. Nikitin, S. Pott, T. Clees and U. Krewer, *Phys. Chem. Chem. Phys.*, 2020, **22**, 16648-16654.

199.   Y. Toshev, V. Mandova, N. Boshkov, D. Stoychev, P. Petrov, N. Tsvetkova, G. Raichevski, C. Tsvetanov, A. Gabev, R. Velev and K. Kostadinov, in *4M 2006 - Second International Conference on Multi-Material Micro Manufacture*, eds. W. Menz, S. Dimov and B. Fillon, Elsevier, Oxford, 2006, DOI: https://doi.org/10.1016/B978-008045263-0/50073-8, pp. 323-326.

200.   B.-A. Mei, O. Munteshari, J. Lau, B. Dunn and L. Pilon, *The Journal of Physical Chemistry C*, 2018, **122**, 194-206.

201.   E. Locorotondc, L. Pugi, L. Berzi, M. Pierini, S. Scavuzzc, A. Ferraris, A. G. Airale and M. Carello, Florence, Italy, 2019.

202.   N. Narendar, G. C. Mather, P. A. N. Dias and D. P. Fagg, *RSC. Adv.*, 2013, **3**, 859-869.

203.   Y. Zhu, W. Zhou, Z. G. Chen, Y. Chen, C. Su, M. O. Tadé and Z. Shao, *Angew. Chem. Int. Edit.*, 2015, **54**, 3897.

204.   J. Zhang, K. Huang, L. Yuan and S. Feng, *CrystEngComm*, 2018, **20**, 470-476.

205.   P. Hao, Z. Lin, P. Song, Z. Yang and Q. Wang, *J. Mater. Sci.: Mater. Electron.*, 2020, **31**, 6679-6689.

206.   Y. Li, J. Liu, X. Huang and G. Li, *Cryst. Growth Des.*, 2007, **7**, 1350-1355.

207.   C. Y. Song, J. Xu, A. Yimamu and L. Wang, *Integrated Ferroelectrics*, 2014, **153**, 33-41.

208.   K. Fukai, K. Hidaka, M. Aoki and K. Abe, *Ceram. Int.*, 1990, **16**, 285-290.

209.   N. K. Singh, P. Sharma, I. Kumar and A. S. Chaddha, *Int. J. Electrochem. Sci.*, 2019, **14**, 11379-11379.

210.   T. Nagai, N. Fujiwara, M. Asahi, S.-i. Yamazaki, Z. Siroma and T. Ioroi, *Journal of Asian Ceramic Societies*, 2014, **2**, 329-332.

211.   S. Park, S. Choi, J. Kim, J. Shin and G. Kim, *ECS Electrochemistry Letters*, 2012, **1**, F29-F32.

212.   J.-H. Kim, F. Prado and A. Manthiram, *J. Electrochem. Soc.*, 2008, **155**, B1023-B1028.

213.   K. Dehnicke and A. Greiner, *Angew. Chem. Int. Edit.*, 2003, **42**, 1340-1354.

214.   M. Sun, X. Chen and L. Hong, *RSC. Adv.*, 2014, **4**, 5618-5625.

215.   J. Li, J. Li, D. Yan, J. Pu, B. Chi and L. Jian, *Electrochim. Acta*, 2018, **270**, 294-301.

216.   L. Jiang, T. Wei, R. Zeng, W.-X. Zhang and Y.-H. Huang, *J. Power Sources*, 2013, **232**, 279-285.

217.   S.-L. Zhang, K. Chen, A.-P. Zhang, C.-X. Li and C.-J. Li, *Ceram. Int.*, 2017, **43**, 11648-11655.

218.   C. Hu, L. Zhang and J. Gong, *Energ. Environ. Sci.*, 2019, **12**, 2620-2645.

219.   A. Vailionis, H. Boschker, W. Siemons, E. P. Houwman, D. H. A. Blank, G. Rijnders and G. Koster, *Phys. Rev. B*, 2011, **83**, 064101.

220.   K. T. Butler, *Journal of Materials Chemistry C*, 2018, **6**, 12045-12051.

221.   M. W. Lufaso and P. M. Woodward, *Acta Crystallographica Section B*, 2001, **57**, 725-738.

222.   B.-J. Kim, E. Fabbri, I. E. Castelli, M. Borlaf, T. Graule, M. Nachtegaal and T. J. Schmidt, *Catalysts*, 2019, **9**, 263.

223.   H. Sun, G. Chen, J. Sunarso, J. Dai, W. Zhou and Z. Shao, *ACS Appl. Mater. Inter.*, 2018, **10**, 16939-16942.

224.   G. Chen, Z. Hu, Y. Zhu, Z.-G. Chen, Y. Zhong, H.-J. Lin, C.-T. Chen, L. H. Tjeng, W. Zhou and Z. Shao, *J. Mater. Chem. A*, 2018, **6**, 9854-9859.

225.   D. Yang, R. Yang, K. Wang, C. Wu, X. Zhu, J. Feng, X. Ren, G. Fang, S. Priya and S. Liu, *Nat. Commun.*, 2018, **9**, 3239.

226.   I. Grinberg, D. V. West, M. Torres, G. Gou, D. M. Stein, L. Wu, G. Chen, E. M. Gallo, A. R. Akbashev, P. K. Davies, J. E. Spanier and A. M. Rappe, *Nature*, 2013, **503**, 509-512.

227.   F. Ye, Y. Zhang, C. Addiego, M. Xu, H. Huyan, X. Ren and X. Pan, *npj Computational Materials*, 2021, **7**, 130.

228.   S. A. L. Weber, I. M. Hermes, S.-H. Turren-Cruz, C. Gort, V. W. Bergmann, L. Gilson, A. Hagfeldt, M. Graetzel, W. Tress and R. Berger, *Energ. Environ. Sci.*, 2018, **11**, 2404-2413.

229.   H. Li, F. Li, Z. Shen, S.-T. Han, J. Chen, C. Dong, C. Chen, Y. Zhou and M. Wang, *Nano Today*, 2021, **37**, 101062.

230.   Y. Uratani, T. Shishidou, F. Ishii and T. Oguchi, *Physica B: Condensed Matter*, 2006, **383**, 9-12.

231.   P.-P. Shi, Y.-Y. Tang, P.-F. Li, W.-Q. Liao, Z.-X. Wang, Q. Ye and R.-G. Xiong, *Chem. Soc. Rev.*, 2016, **45**, 3811-3827.